UNIVERSITÉ CLERMONT FERRAND II – BLAISE PASCAL

T H È S E

pour obtenir le grade de

DOCTEUR DE L'UBP

Discipline : Physique des Particules

préparée au CERN/AT/MCS

dans la cadre de l'**École Doctorale des Sciences Fondamentales**

présentée et soutenue publiquement le

15 Décembre 2006

par

Boris BELLESIA

Correlation between Magnetic Field Quality and mechanical components of the Large Hadron Collider Main Dipoles

_____

Directeurs de thèse :

Prof. Claudio SANTONI

Dott. Ezio TODESCO

_____

JURY

Prof. Pierre HENRARD, Président

Prof. Francisco CALVIÑO

Dott. Walter SCANDALE

Acknowledgements

I have to express my sincere thanks to Dott. Ezio Todesco. He has been my supervisor and closest colleague. His intelligent leadership together with his deep knowledge of magnet technology and accelerator beam physics made my effort much easier. I hope the future projects will allow me to keep enjoying both his professional skills and his friendship.
I would like to thank my supervisor Prof. Claudio Santoni for his initiative, which made possible doing my Diploma and Doctoral Theses at CERN.
I have to thank Prof. Pierre Henrard leader of the "Laboratoire de Physique Corpusculaire" at the University Blaise Pascal for the doctoral position necessary to carry out this work.
I would also like to express my gratitude to Dr. Walter Scandale, for his continuous and valuable support during the development of this thesis. It has been a pleasure and a privilege to work together within during these years.
Particular thanks must be addressed to Lucio Rossi and his group – AT-MCS – at CERN. In particular I would like to acknowledge Paolo Fessia, Frederique Savary, Marta Baiko, Andrea Musso, Paulo Martins, Gjis de Rjik belonging to the section in charged in of production of the main dipole. Also thank to Francesco Bertinelli (and its Component Center) which follow-up the mechanical components production, without his collaboration a big part of this work could not been completed.
Many thank to Gianni Molinari whose ideas and discussions were the starting points for the development of the method used to localize electrical faults in the superconducting dipole coils.
Thank to Alstom-Jeumont, Ansaldo Superconduttori, and Babcock Noell enterprises and their staff who gave me the possibility to perform special magnetic measurement during the main dipole production, essential for this work.
This doctoral thesis is the most important step of my student career. I want to remember and sincerely thank all the professors in Torino who led my first steps into the world of Science and in particular to my High School physics teacher Don May.
A big hug to the guys that supported and suffered me during these years, my family in Geneva: Giuseppe, Federico Ra., Stefano Pa., Alex , Federico Ro., Alberto, Luis, Mirko, Georgina, Jose, Juan, Álex, Iván, Tatiana, Stefano Re., Christos, Andrea, Chiara, Elena, Fabrizio, Gianluca, , Andrés, Rocío, Motse and Dave. Thanks guys.
…e adesso mi tocca ringraziere la mia famiglia tutta…uff…che difficile, come faccio a ringraziare? Dovrei incominciare ringraziando per il sostegno che e' stato dato ad ogni mio progetto… o per la fiducia che mi hanno sempre riposto…o per i sacrifici che hanno fatto, noti e no…o per l'amore che mi hanno fatto conoscere e che mai e' venuto meno? Non so cosa venga per prima ma sicuramente no basterebbe mai.
Ed ora un grazie agli amici di Torino che hanno cercato di non lasciarmi scappare definitivamente: Eliano, Daniele, Franci, Raffa ed Elisa.
Gracias Esther.

Contents

Chapter 1

Introduction

CERN is the European Organization for Nuclear Research, one of the world most influential particle physics laboratories. It was founded in 1954 by 12 European countries. Now, in 2006, there are 20 Member States. CERN's mandate is the construction and operation of large accelerators: the Synchro-Cyclotron (SC, 1957) and the Proton Synchrotron (PS, 1959) were followed by the Intersecting Storage Rings (ISR, 1971), the Proton Synchrotron Booster (PSB, 1972) and the Super Proton Synchrotron (SPS, 1976). The Large Electron-Positron storage ring (LEP) was completed in 1989, installed in a tunnel of 27 km circumference and it was operated between 1989 and 2001. The Large Hadron Collider, whose commissioning is foreseen for the end of 2007, will be installed in the LEP tunnel emptied after the LEP definitive shut down. The LHC will be the first storage ring in which quarks and gluons collide in the TeV energy range and represent the next step in high energy physics research.

To force the beams into circular orbits, dipole magnets providing a constant magnetic field are necessary. They have two poles producing field lines in the aperture of the magnet (where the beam passes) perpendicular to the plane of the particle beam orbit. They are in general electro-magnets, with magnetic fields generated by the flow of electric current in the winding of their coils. The coils are encased in a ferromagnetic yoke which provides a return path to close the field lines and to increase the field in the aperture. Depending on the field strength several designs are possible:

- low field (up to 2 T) iron-dominated magnets;
- super-ferric magnets;
- superconducting magnets;

In the iron-dominated magnets the peak magnetic field is limited by the iron saturation at about 2 T. The field shape depends principally on the shape of the iron yoke, which determines the good field region where the beam can travel safely. In most of the cases, such magnets are resistive, although there are examples of iron-dominated superconducting magnets, where the yoke can remain either at ambient or at cryogenic temperature. For fields above 2 T, the magnets should be superconducting and the coil should produce the additional magnetic flux. In this case, the coil becomes larger and the placement of the conductors determines the shape and the quality of the field. Laminated steel spacers called collars are in general placed around the coils and inside the yoke in order to confine the conductors and keep them

in place. In many cases, the yoke itself is used to support the coils. These magnets, called high-field magnets, may be rectangular or circular. In the high-field rectangular magnets [2], the conductors are placed above and below the aperture and the coil features a rectangular shape. In the round magnet design, the coil is placed in a cylindrical shell around the magnet bore. This coil configuration is called the $\cos\theta$ configuration, since the current distribution in the cylindrical shell approximately varies as the cosine of the angle from the mid plane. Dipoles with the $\cos\theta$ configuration and Nb-Ti superconductors have been built for the following accelerators:

- Tevatron at Fermilab, Chicago, USA: 4.4T;
- HERA at DESY, Hamburg, Germany: 4.7T;
- RHIC at Brookhaven, New York, USA: 3.5T;
- SSC (project cancelled in October 1993) at SSCL, Texas, USA: 6.6T;

In the Large Hadron Collider in which counter rotating beams collide, the magnet design option of "two-in-one" $\cos\theta$ design is adopted, where the two sets of coils for the two beams are combined in a single iron yoke.

To avoid as much as possible beam orbit perturbations, the magnetic field provided by the dipoles is required to have a high level of homogeneity. In terms of magnet technology the field must respect a high quality determined by controlling the magnetic field harmonics along the magnet production. The field harmonics are the coefficient of series expansion of the magnetic field inside the aperture, and are the spurious modes added to the main component. Any harmonic (or multipole) component must be kept small, within values determined by beam stability studies. In superconducting magnets, the field quality is strongly dominated by the position of the conductors which depends on many factors, like design geometry, induced currents effect, iron saturation and geometry errors during fabrication of the mechanical components.

If the design geometry is respected, all the multipole values should be sufficiently small to avoid detrimental effects for beam stability. The systematic components of field harmonics are due to the coil design or systematic errors being identical in all dipoles of a series production. Random parts of the multipoles, ideally zero, vary from dipole to dipole and they are induced by tolerances of mechanical components and by assembly procedures. During the R&D phase of the LHC main dipole many studies have been done to predict the effects on the field quality induced by the tolerances imposed to the mechanical components and by the assembly procedures. The usual way to calculate the effect of geometry error on the field quality is to change one by one the geometrical parameters of the magnet model and to evaluate the consequent effect on field shape. In this way, one can build sensitivity matrices, which give the relation between geometrical parameters and field components. This method permits to identify the area of the magnet with a relevant influence on field quality, and hence to specify the tolerances for the mechanical components.

In 2001, the series production of 1248 dipoles has started. Since then, all magnets have been manufactured; the field has been measured in warm conditions for 100% and at 1.9 K for 20%. Data relative to coil components, dimensions and proprierties have been stored. The aim of this thesis is to carry out an analysis of the influence of

the components on the field quality, a check of the homogeneity of the production and of the assembly procedures identifying the correlations with the magnetic field measurement.

In chapter 2 we present the main parameters of the Large Hadron Collider and of its superconducting main dipole. The mechanical components are described in detail and their mechanical and magnetic functions are explained. Chapter 3 is focused on the magnetic field and on the magnet design of the coils together with some issues about multipolar expansion theory. Main information of the magnetic measurements and the control limits used for the LHC main dipoles are given.

The original part of the work is presented in chapter 4, 5 and 6 where we analyze the influence on the magnetic field of the productions of the following components:

- superconducting cables
- coil copper wedges
- coil retaining collars.

For each component, a dimensional analysis is performed to analyze if the productions respected the tolerances. Each production is then split according to the supplier and the assembly procedures and compared with the magnetic measurements performed on the first magnetic assembly in the LHC main dipoles assembly chain – the collared coil" – to find correlations. Computing sensitivity tables of the effects of the geometry on the field quality with "ad hoc" magneto-static models, the influence of the components on the magnetic field is calculated and compared with the measurements. Finally Monte Carlo codes are developed in order to foresee the effect of the successive component production on the magnetic field quality. Since the three component productions were studied during their production period there is not homogeneity among the studies presented in the number of the available data of components and collared coil measurements.

In chapter 7 a more general study on the random components of the field errors is presented. In previous works, estimates of the geometric random errors are usually based on estimating field perturbations induced by a random displacement of the coil blocks with a spread of ~50 μm. We developed a Monte Carlo code aiming at giving a more precise calculation of this value. The approach is based on the assumption that the conductor blocks of the coil layout are rigid and shape-retaining entities which can be moved randomly along their three degrees of freedom in the magnet cross section plane. Numerical simulations are worked out in order to fit the measurement of the random component for the LHC main dipole production; in addition we analyzed the main dipole productions of Tevatron, HERA and RHIC.

Finally in chapter 8, we present a method to localize the short circuits by means of the magnetic field measurement at room temperature. The localization goes through steps, starting evaluating the field anomaly generated by the electrical defect up to the identification of the two cables short-circuited along the 15 m dipole aperture. Before the development of this method when a short circuit was detected with the coil resistive measurement the cold mass assembler could only identify the affected pole. Without a finer localization the indetermination of the position was the total length of the coil, which made unlikely the repair. The method lowers the indetermination to the length of the magnetic measurement mole (0.75 m), and it can

also distinguish between inner or outer layer, making possible the precise localization and reparation of the damage. For these reason, since the very first time that the method was applied, the three cold mass assemblers adopted it as an essential tool to rescue the faulty collared coil with considerable money and time savings.

Chapter 2

The Large Hadron Collider and its main dipole

In December 1994 the CERN Council approved the Large Hadron Collider (LHC) project [2.1]: a circular particle accelerator replacing the Large Electron Positron Collider (LEP) in the underground tunnel of 27 km in circumference where the accelerated particles will be protons instead of electrons and positrons. The LHC commissioning it is forecast for the end of 2007.

The ambitious project will provide two counter direction proton beams of 7 TeV. They will collide in four experiments (ALICE [2.2], ATLAS [2.3], CMS [2.4] and LHCb [2.5]) with a maximum particle interaction energy of 7+7 TeV which is order of magnitude above the actual maximum colliding energy (0.98+0.98 TeV of the Tevatron at Fermi National Laboratory, Chicago, IL, USA [2.6]). The LHC experiments will explore unknown fields of high energy particle physics, answering to some open questions such as the existence of the Higgs boson and super-symmetric particles, and validating the Standard Model.

LHC will be supplied with protons by the injector chain illustrated in Figure 2.1. The protons are generated by a Duoplasmatron source from which they are extracted with a kinetic energy of 100 keV and injected in the Linac. The Linac consists of a beam transport line of about 80 m along which the particles are accelerated to 50 MeV and grouped in buckets by mean of radio frequency cavities. The protons are then injected in the Proton Synchrotron Booster (PSB), a 157 m circumference complex capable of accelerating high intensity beams up to 1.4 GeV and composed of a stack of four separate rings with a common magnetic and radio frequency system. From the PSB the particles are transferred to the Proton Synchrotron (PS), a 628 m circumference ring, where they are accelerated to 26 GeV. Up to this point the accelerators complex is installed at ground level. A beam transport line connects the PS to the Super Proton Synchrotron (SPS), which has a circumference of 6.9 km and lays at about 50 m underground. In the SPS the beam energy increases from 26 to 450 GeV. The particles beams will be injected from the SPS to the LHC via two transfer lines in order to establish two circulating beams in opposite directions. These two transfer lines provide the connection between the SPS and the LHC which lays between 80 and 150 m underground. When all the particle bunches fill the two LHC rings, the energy is raised up the nominal and finally the two beams are collided.

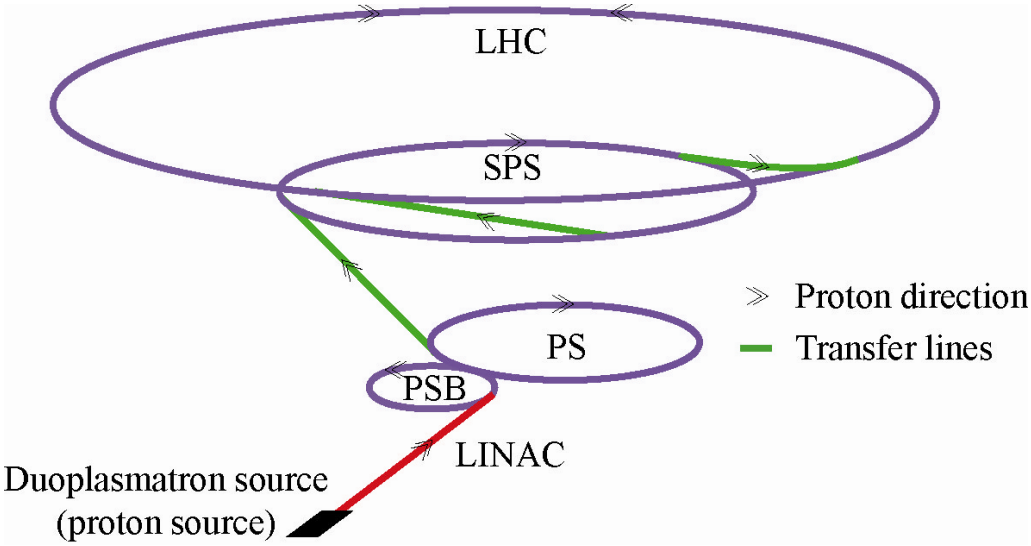

Figure 2.1: The LHC ring and the CERN accelerating chain.

In order to reach the LHC energies (7 TeV per beam) in the same tunnel where the LEP (0.1 TeV per beam) was hosted; the magnetic field *B* of the dipoles must be increased to 8.33 T, according to:

$$E \propto qBR \qquad \text{Eq. 2.1}$$

where *E* is the energy of the beam, *q* is the particle charge and *R* the radius of the accelerator circumference. The main LHC magnets are:

- The dipole magnets which bend the particles along the accelerator circumference; there are a total of 1232 units providing a magnetic field of 8.33 T perpendicular to the accelerator plane;
- The quadrupole magnets, which focus the particles bunches; there are a total of 386 units providing a magnetic field that is null in the center of the beam pipe and linearly increases with the distance from the center; the LHC quadrupoles have a field gradient of 223 T/m.

In addition to the previous two main magnet types about 4000 correctors magnets are installed.

2.1 The LHC main dipole

In order to steer the 7 TeV beam correctly in the beam pipe an 8.33 T dipole field has to be provided by 15 m long dipole magnets positioned all along the accelerator ring. To reach such fields, the magnets have to rely on superconducting technology which allows transporting high current density without heat generation (zero resistance) and consequently, generating high magnetic field. The design and the production were developed following the experience of four machines using superconducting magnet: Tevatron (commissioned in 1983), HERA (DESY, Germany, commissioned in 1990 [2.7]), RHIC (Brookhaven, USA, commissioned in 1999 [2.8]) and SSC (project

cancelled in October 1993, SSCL Texas, USA [2.9]), see Figure 2.2. Their magnets all make use of classical Nb-Ti superconductor [2.10] cooled with liquid helium at 4.2 K and their operating fields are,: 4.5, 4.7, 3.5 and 6.6 T.

To obtain higher magnetic field, the cooling helium temperature has been lowered to 1.9 K in order to increase the critical field and current of the superconductor. Below 2.17 K liquid helium becames superfluid [2.13], a macroscopic quantistic propriety (like superconductivity), having a much lower viscosity and a much greater heat transmission capacity with respect to the liquid helium. From the other hand, the enthalpy of the metallic components is lowered of about one order of magnitude. This means that their temperature increases much faster for a given energy deposition and then, for LHC magnets, a more careful study of the retain structures with respect to the past projects has to be done.

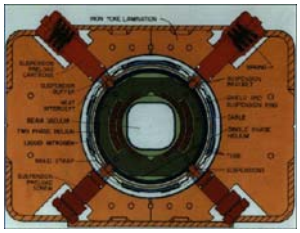

Tevatron
B=4.5 T
Bore: 76 mm

HERA
B=4.7 T
Bore: 75 mm

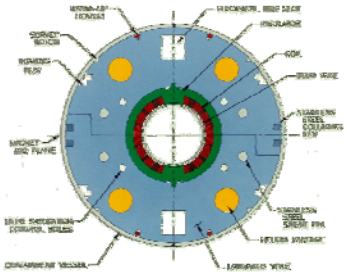

RHIC
B=3.5 T
Bore: 80 mm

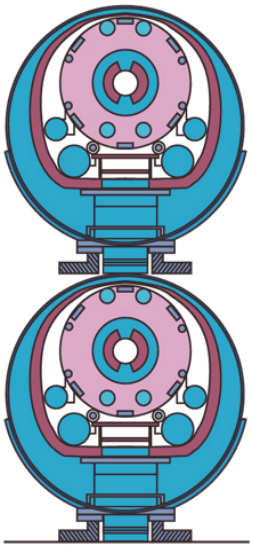

SSC
B=6.6 T
Bore: 50-50 mm

Figure 2.2: Cross section of four superconducting dipoles.

The LHC main dipoles feature, for the first time in the dipole for accelerators, a two-in-one design. That is, the two proton beams circulating in opposite direction will pass through a common structure but in two physically separated channels (or apertures). This made possible to lower the costs of about 30% and to save precious space in the tunnel [2.1]. The two apertures must provide vertical magnetic fields with opposite signs to bend two proton beams circulating in counter directions; in Figure 2.3 the magnetic field lines are sketched: the 2-in-1 design creates a cross-talk between the two coils.

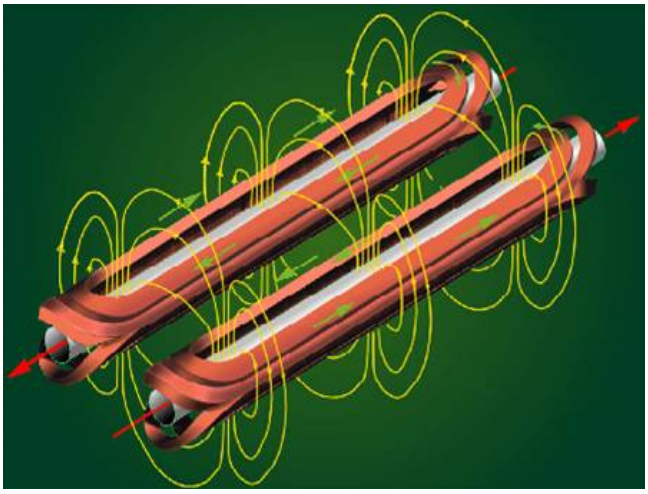

Figure 2.3: The magnetic filed lines in a LHC main dipole.

The coils are surrounded by a containment structure that consists of coil clamping elements, the collars, the iron yoke and the shrinking cylinder (Figure 2.4). These elements contribute to producing the necessary pre-compression in the coils to prevent stresses arising in the coils under the action of the electro-magnetic forces when the magnets are powered. During operation, the assembly inside the shrinking cylinder, the so-called cold mass, is kept at 1.9 K. The cold mass is installed inside a cryostat forming the cryo-dipole which consists of a support system, cryogenic pumping, radiative insulation and thermal shield, all contained within a vacuum vessel. The cryostat provides a stable mechanical support for the cold mass whilst limiting heat inleak to match the strict heat-load budget of the LHC, determined to keep cables temperature in the range needed for Nb-Ti to be in the superconducting state. The cryostat and the dipole thermal shields are shown Figure 2.4. The dipole cryostat runs at three temperature levels, 1.9 K for the cold mass, and at 5-20 K and 50-70 K for the two intermediate heat intercept levels. The vacuum vessel contains insulation vacuum at a pressure below 10^{-6} mbar and is made of construction steel to reduce costs and shield stray magnetic flux. Two alignment targets are mounted on it and works as outer reference to the inner magnetic axis to properly align the LHC components.

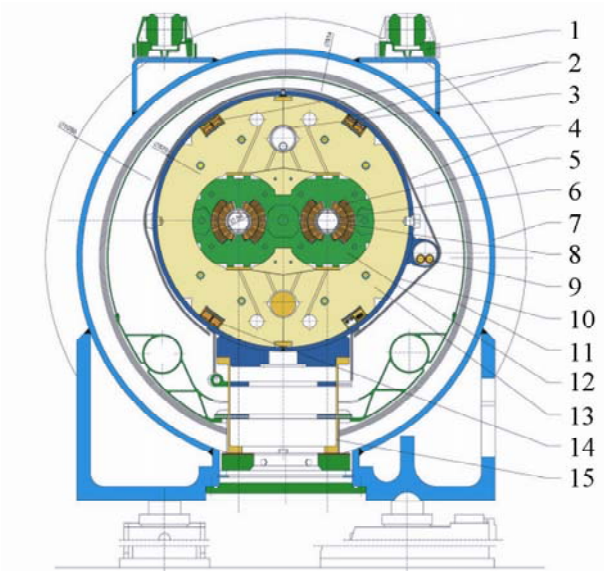

Figure 2.4: Twin aperture LHC dipole magnet cross-section: 1- alignment target; 2- main quadrupole bus-bars; 3- heat exchanger pipe, 4- super insulation; 5- superconducting coils; 6- beam pipe; 7- vacuum vessel; 8- beam screen; 9- auxiliary bus-bars; 10- shrinking cylinder / He I-vessel; 11- thermal shield (55 to 75K); 12- non magnetic collars; 13- iron yoke (cold mass, 1.9K); 14 -dipole bus bars; 15- support post.

Table 2.1: LHC main dipole parameters

Parameter	Value	Units
Injection field (0.45 TeV beam energy)	0.54	T
Current at injection field	763	A
Nominal field (7 TeV beam energy)	8.33	T
Current at nominal field	11850	A
Inductance at nominal field	98.7	mH
Stored energy at nominal field	6.93	MJ
Operating temeperature	1.9	K
Aperture radius	56	mm
Bending radius at 1.9 K	2803.98	m
Magnetic length at 1.9 K	14312	mm
Coil inner diameter	56	mm
Coil outer diameter	120.5	mm
Coil length	14467	mm
Thickness of insulation to ground	0.75	mm
Distance between aperture axes at 1.9 K	194	mm
Collar height	192	mm
Collar width	396	mm
Yoke outer diameter	550	mm
Shrinking cylinder	570	mm
Length of active part	14603	mm
Overall cold mass length	15180	mm
Cold mass weight	27.5	t
Outer diameter of cryostat	914	mm
Inner diameter of cryostat	890	mm
Overall cryo-dipole weight	31.5	t
Forces/coil quadrant at nominal filed		
$\sum Fx$	1.8	MN/m
$\sum Fy$	0.81	MN/m
Axial force at each end at nominal field	0.50	MN

2.2 Cold mass and main components

The LHC cold mass is manufactured by assembling a large number of components. Here, the main ones are presented briefly. As shown in Figure 2.5, the cold mass is made of:

- superconducting coils,
- collars,
- ferromagnetic iron yoke and inserts,
- shrinking cylinder.

In the last part of the assembly procedure, the cold mass is inserted into the cryostat, together with other components (spool pieces, corrector magnets, etc... see [4]).

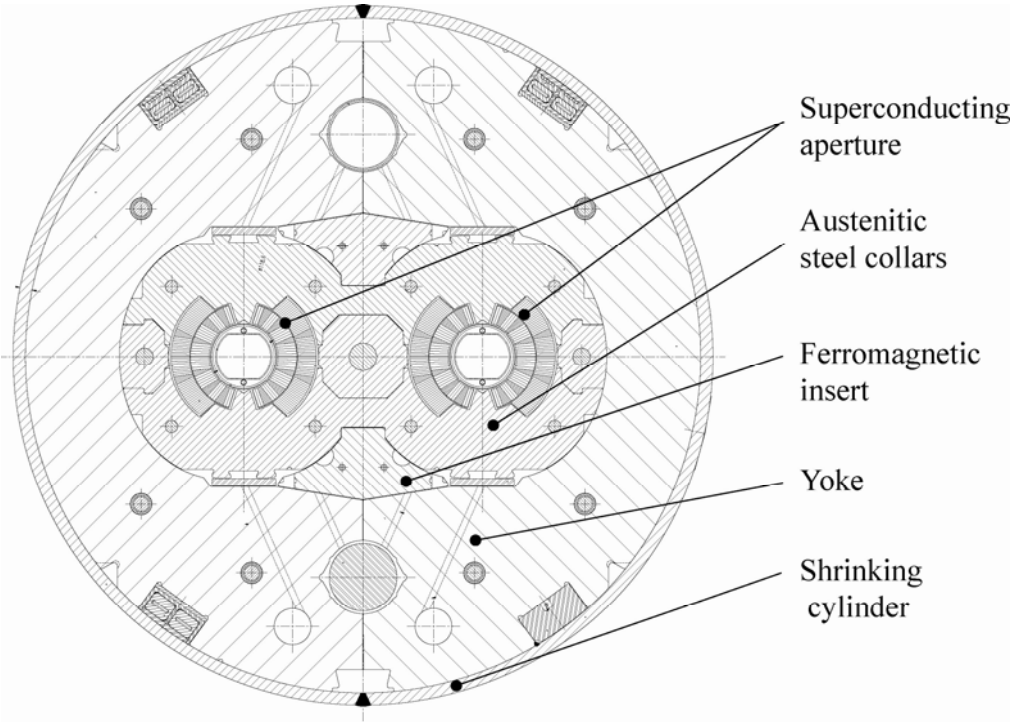

Figure 2.5: Dipole cold mass cross section.

2.2.1 Superconducting coils

A twin-aperture dipole consists of two single dipoles, each around a beam channel. Each dipole has an upper and a lower pole which are identical. Each pole consists of a coil wound in two layers, called inner layer and outer layer, wound with two different cables. The six sets of adjacent coil turns within the limits of the various copper wedges are defined as cable *blocks*. Each aperture provides a vertical field perpendicular to its longitudinal axis; the two apertures, connected in series and fed by the same operating current, originate two vertical uniform magnetic fields with opposite sign (see Figure 2.3).

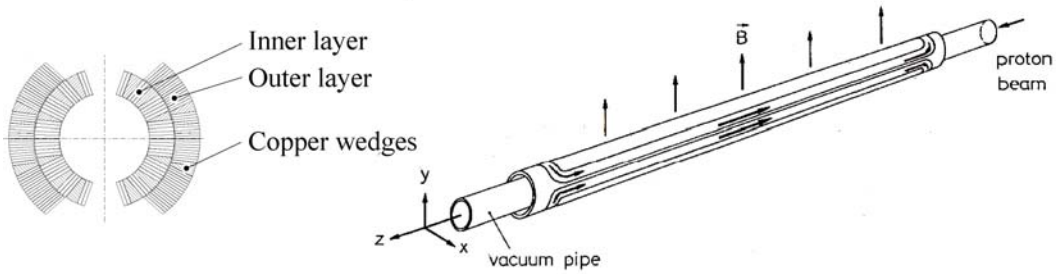

Figure 2.3: Aperture cross-section of the LHC dipole. Right: Vertical field generated by the coils.

Superconductivity

Superconductivity was discovered in 1911 by the Dutch physicist H. Kamerlingh Onnes, only three years after he had succeeded in liquefying helium. During his investigations on the conductivity of metals at low temperature, he found that the electrical resistance of mercury dropped to a non-measurable small value just at the boiling temperature of liquid helium. This was indeed a great discovery: when an electric current goes through a normal conductor there is an energy loss due to resistance; if it vanishes, also the losses do. Onnes called this phenomenon *superconductivity* and his name has been retained since. The temperature at which the transition took place was called the *critical temperature* T_C.

Superconductivity is a quantistic effect related to the electronic reorganization which a particular material undergoes when it reaches its critical temperature. A complete description of the state-of-the-art knowledge about superconductivity (see for instance [2.14] for references), goes beyond the aim of this work. It is enough to say that the cables used for the LHC magnets are made of Nb-Ti. This material maintains the superconducting state if its values of temperature T, magnetic field B and current density j are below the so-called *critical surface*, see Figure 2.6.For Nb-Ti the critical values of temperature and magnetic field at zero current density are: B_c = 14.5 T and T_c = 9.2 K

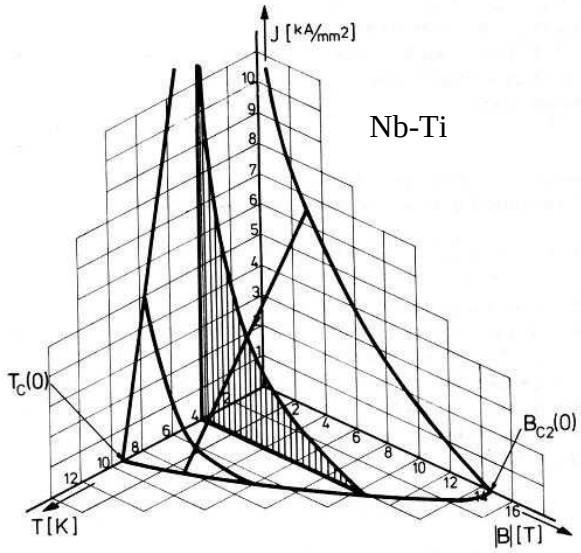

Figure 2.6: Critical surface for a superconductor: depending on the values of temperature T, magnetic field B and current density J at its interior, the conductor change to the normal state if the three value localize a position outside the critical surface.

The transition of a superconductor to its normal state is called *quench* and it can happen for a variation of one of the three parameters. For the LHC dipoles and the cables used in its design a quench can not be provoked by the magnetic field or by the current density going over their design values. Actually, in operational condition the working point of the dipoles in the (B,T,*j*) space is below the critical surface (B=8.33 T, T=1.9K, j=1.9 kA/mm^2) . Instead, the main cause of quenches in the LHC magnets is the thermal energy release due to a conductor movement and a consequent temperature increase over the critical temperature. In fact, the release of energy due to a displacement of some micrometers can be enough to loose the superconductivity state.

2.2.2 The superconducting cables

The transverse cross-section of the coils of the LHC dipole magnet has two layers of different cables distributed in 6 blocks. The cables used in the dipole coils are of the Rutherford type, see Figure 2.7, and they are composed by strands arranged in trapezoidal shape. Their insulation is designed to provide simultaneously the required electrical insulation level, allow the heat transfer (achieved by allowing superfluid helium to permeate the insulation and wet the conductors) and maintain the coil turns in their position. The Rutherford cables used in the LHC dipole coil has 28 strands in the inner layer, each of 1.065 mm diameter, and 36 strands in the outer layer, each of 0.825 mm diameter. Each strand is made by a large number of NbTi filaments (about 8000) embedded in copper which provide a bypass to the electric current flowing in the superconducting filaments when they undergo a quench. Figure 2.7 shows an example of strand used for the LHC magnets.

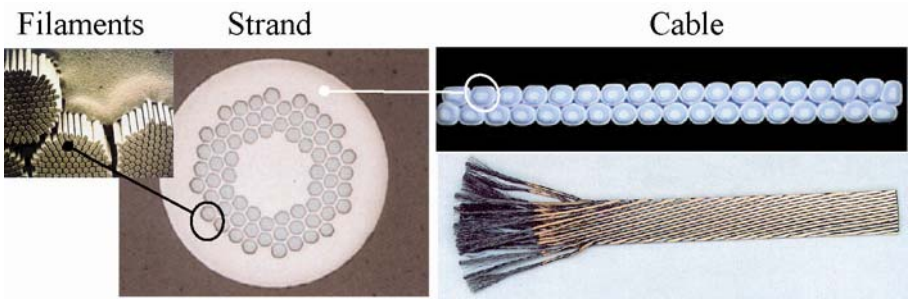

Figure 2.7: Left: LHC superconducting strand made of around 8000 NbTi filaments embedded in a copper matrix forming the strand – center. Right: Rutherford cable: cross section (top); (bottom) conductor windings (the left side is thicker)

2.2.3 Mechanical structure

The structure of the dipole is designed to withstand the high forces generated in the magnet and limit as much as possible the coil deformation during operation. Therefore, the materials used for the most highly stressed components have a high load-bearing capacity, high elastic moduli, good fatigue endurance and a good behavior at cryogenic temperatures down to 1.9 K.

Collars

The high currents and fields in a typical shell coil as shown in Figure 2.3 produce very large Lorentz forces on the conductors [2.10]. The Lorentz forces have two main components: an azimuthal component, which tends to squeeze the coil towards the mid-plane, and a radial component, which tends to bend the coil outwards, with a maximum displacement at the coil mid-plane.

These components may produce wire motions inside the coil. If the motions are purely elastic, no heat is dissipated and the coil remains superconducting. However, if the motions are frictional, the associated heat dissipation may be sufficient to produce a quench. The motions must therefore be prevented as much as possible by providing a rigid support to the coil: the collars (see Figure 2.8). The collars confine radially the coil inside a rigid cavity hence counteracting the radial component of the Lorentz forces. Moreover, since the azimuthal component compresses the coil towards the mid-plane, at high field the coil turns close to the poles tend to move away from the collar poles. To prevent this phenomenon, the collars are assembled in order to produce an azimuthal pre-compression, called *pre-stress*, on the coils. The rule followed during assembly is to apply an azimuthal pre-stress such that the coil does not lose compression at the pole at full magnet current. Therefore, the coil pre-stress applied at room temperature by the collar must be sufficient to compensate for:

- stress redistribution due to the azimuthal component of the Lorentz forces at high current;
- differential thermal shrinkage between collars and coil during cool-down;
- insulation creep following the collaring procedure.

In the LHC dipole it has been chosen an azimuthal pre-stress at ambient temperature after collaring of 75 ±15 MPa, which falls down to about 30 ± 7 MPa after the cool-down. The collars are made of a 3 mm thick high-strength stainless steel sheet. They are closed around the two coils by means of three locking rods (Figure 2.8). Collars sheets are superposed one to the other to create packs assembled using pins. Each layer is composed of two different parts, the so-called long-collar and the short-collar. The long-collar contains the holes where to put the locking rods. The short one has indeed a pure filling function and proposal to replace them with cheaper materials were done in the R&D phase [2.11]. Different layers of collars are assembled putting alternatively the long collars on the upper part and on the lower part of the magnet.

Ferromagnetic Iron yoke and insert

Referring to Figure 2.5, the iron yoke is made of 6 mm thick low-carbon-steel laminations split into two at the vertical symmetry plane of the twin-aperture magnet. Between the two halves, a gap is present to compensate for the difference in thermal contraction of the iron yoke and the coil/collar assembly during cooling from room temperature to 1.9 K [2.15]. The iron yoke is needed as a magnetic flux return circuit, i.e. to shield the external part of the magnet from the inner field, and, in the LHC case, it also partially acts as a force retaining component (10-20% with respect to collars). The pressure with which this component is mounted on the collared coil is transmitted

to collars by ferromagnetic inserts (Figure 2.5), whose shape is carefully designed to avoid a left-right asymmetry of the field in each of the two apertures [2.12].

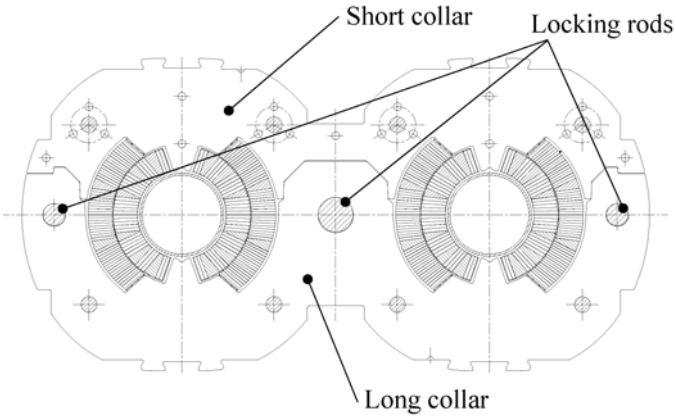

Figure 2.8: Collared coil assembly straight part cross-section: type 1 and type 2 collars mounted on coils and the structure locking rods are shown.

Shrinking cylinder

When the iron yoke laminations are mounted on the collared coil, a stainless steel cylinder is welded around the assembly. In effect, this part is welded with interference around the iron yoke in such a way that the required pre-stress is obtained. The shells are made up of austenitic stainless steel, grade 316LN [2.16]. They have a length of 15350 mm, a 275 mm inside radius and a thickness of 10mm. Furthermore, they are bent in opposite directions, so that one is concave and the other convex in order to achieve, after longitudinal welding around the yoke, the specified horizontal curvature of the dipole cold mass. The shrinking cylinder gives to the cold mass assembly the inertia necessary to keep the self-weight induced deflections within the specified limits. It is also the main part of the helium containment vessel, which has to be leak with respect to gaseous helium at a test pressure of 26 bar, and at 1.9 K with respect to superfluid helium at an operating absolute pressure of 1.3 bar.

2.3 Magnet assembly

Since the LHC machine is designed to have 1232 dipoles, series production has been the only option to be taken into account for the manufacture of this item. Components are manufactured by different firms that have to follow CERN specifications in the production steps. Once components are manufactured, they are assembled in the following sub-assemblies by the so called Cold Mass Assemblers:

- Coils;
- Collared coils;
- Cold mass.

The cold mass is shipped to CERN where it is inserted into the cryostat.

2.3.1 Coil curing

The two layers are wound and cured on different dedicated mandrels. The objectives of curing are three-fold:

- to form the coil into the correct shape and correct dimensions;
- to make the coil as uniform as possible along its length;
- to polymerize the epoxy of the cable insulation (Figure 2.9) in order to make the coil rigid and thus easier to manipulate.

Correctness of coil dimensions is important for the magnetic field quality. Uniformity of the coil is also required to achieve uniform pre-compression after collaring. [25] During pressing and curing operation, the cable temperature must never exceed the threshold of 200°C. Before increasing the temperature to the curing level, a phase of pressure and thermal cycles takes place in order to settle the coils. The pressure in the coil is increased from 10 to 80/100 MPa and then sizing is performed at temperatures between 100 and 135 °C. After curing, poles are assembled and the coils can undergo the collaring procedure.

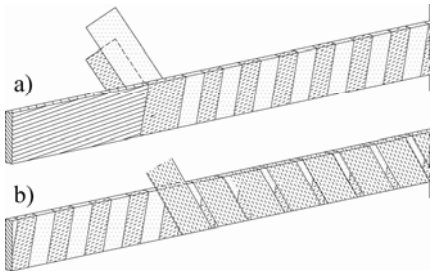

Figure 2.9: Conductor insulation: two polyimide layers wrapped around the cable, with 50% overlapping (a), and another adhesive polyimide tape wrapped onto the cable and spaced by 2mm (b).

2.3.2 Collared coil assembly

To obtain the collared coil sub-assembly, the four poles are assembled in couples around the cold bore tubes in order to obtain two dipole apertures. Pre-assembled packs of collars or pairs of collars are placed around the two insulated single coils. During these operations, collaring shims can be inserted in the inner and outer coil layer in order to fine tune both magnetic field quality (see next chapter) and coil pre-stress. The coil/collar assembly is then introduced into a collaring press. Starting with a pre-stress phase when the collars are only partially closed and increasing up to a pressure where temporary locking rods of reduced diameter can be inserted into the stack, pressure cycles are performed until the introduction of the final nominal rods (see Figure 2.8)

2.3.3 Cold mass assembly

The cold mass assembly begins with a collared coils and a set of half yokes, yoke insert packs and austenitic stainless steel half-cylinders, as shown in Figure 2.5. After the assembly is obtained, it is transferred to a welding press. The half cylinders have to be longitudinally welded around the yoke so that the final average circumferential pre-stress is at least 150 MPa. To obtain such a level of pre-stress, the two shells are welded under pressure. The desired pre-stress level gives the assembly the correct stiffness to withstand its own weight and to be manipulated without affecting the coils. Before welding, the active part (collared coil, half yokes and magnetic inserts) is pushed against a curved jig, so that the nominal horizontal curvature and sagitta are

obtained. Then all the ancillary parts and components (not mentioned in this work) are fixed on the shrinking cylinder, which has to be leak and pressure tested, and then inserted into the cryostat.

2.4 Main dipole production

A contract, for the production of 1248 dipole magnets, was placed in autumn 1999 with 3 European companies: consortium Alstom-Jeumont in France, ASG Superconductors in Italy and Babcock Noell Nuclear in Germany [2.17]. In October 2006 the last cold mass was delivered to CERN (Figure 2.10). More than half of the 1232 arc dipoles, after having passed all acceptance tests, are installed in the LHC tunnel.

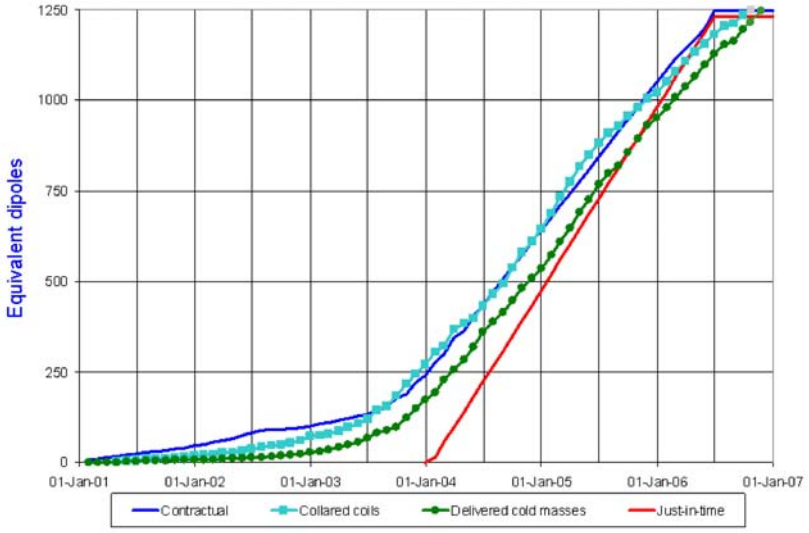

Figure 2.10: Collared coil accepted and cold masses delivered.

During the production, the dipole coil was modified to reach the targets imposed by the beam dynamics to the quality of the magnetic field (see next chapter). The first modification was made at the beginning of the production by changing the wedges of the inner layer blocks and keeping the same coil azimuthal length. The first modification was not enough to steer the magnetic multipoles inside the limits and a ground insulation foil of a thickness of 0.12 mm was added between the two poles of the apertures. In Table and figure the geometric parameters of the 3 cross sections are reported.

Table 2.2: Geometric parameters of the three LHC dipole cross sections.

		Cross section 1		Cross section 2		Cross section 3	
block	r [mm]	φ [deg]	α [mm]	φ [deg]	α [mm]	φ [deg]	α [mm]
1	43.900	0.157	0.000	0.157	0.000	0.239	0.000
2	43.900	21.900	27.000	21.900	27.000	21.982	27.000
3	28.000	0.246	0.000	0.246	0.000	0.374	0.000
4	28.000	22.020	24.080	22.020	25.430	22.148	25.430
5	28.000	47.710	48.000	47.980	45.800	48.108	45.800
6	28.000	66.710	68.500	66.710	68.500	66.838	68.500

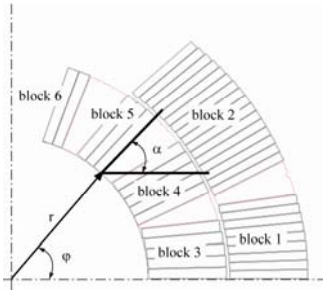

Figure 2.11: Geometric parameters of the LHC dipole cross section.

In Table 2.3 the collared coils produced by the three Cold Mass Assemblers split according to the cross sections are shown.

Table 2.3: Collared coil production split according to cold mass assembler and cross section design.

Cold Mass Assembler	Cross section 1	Cross section 2	Cross section 3	Total	Date of last collared coil produced
Firm1	16	47	353	416	Oct. 2006
Firm2	6	55	355	416	Oct. 2006
Firm3	10	45	361	416	Aug. 2005

References

[2.1] *LHC Design Report Volume I.* CERN-2004-003-V-1, 2004.

[2.2] *ALICE, A Large Ion Collider Experiment;* http://alice.web.cern.ch/alice.

[2.3] *ATLAS, A Toroidal Lhc ApparatuS;* http://atlas.web.cern.ch/atlas/welcome.html

[2.4] *CMS, The Compact Muon Solenoid*, URL: http://cmsinfo.cern.ch/welcome.html.

[2.5] *LHCb, The Large Hadron Collider Beauty experiment*, http://lhcb.web.cern.ch/lhcb

[2.6] *Tevatron*: http://www-bdnew.fnal.gov/tevatron

[2.7] *Hadron Electron Ring Acc*.: http://ppewww.ph.gla.ac.uk/preprints/97/08/gla_hera/node1.html

[2.8] *Relativistic Heavy Ion Collider*: http://server.c-ad.bnl.gov/esfd/status.htm

[2.9] *Superconducting Super Collider*: http://www.hep.net/ssc

[2.10] K.-H.Mess, P.Schmuser, S.Wolff, "*Superconducting accelerator magnets*", World Scientific Publishing, 1996.

[2.11] P. Fessia et al., "*Selection of the Cross-Section Design for the LHC Main Dipole*", IEEE Trans. Appl. Supercond. **Vol 10** (**2000**) , 65-8 also **CERN-LHC-Project-Report-347**

[2.12] E. Todesco et al., "*Optimization of the Even Normal Multipole Components in the Main Dipole of the Large Hadron Collider*", **CERN-LHC-Project-Report-578**

[2.13] S. W. Van Sciver, "*Helium cryogenics*", Plenum Press, 1986.

[2.14] A.C. Rose-Innes, E.H. Rhoderick, "*Introduction to superconductivity*", Pergamon Press, 1988

[2.15] *"LHC technical specification for the supply of 1158 cold masses of the superconducting dipole magnets for the LHC collider", **Annex G6,*** LHC Project Document **LHC–MB A–C1–0006**.

[2.16] *"LHC technical specification for the supply of 1158 cold masses of the superconducting dipole magnets for the LHC collider", **Annex G8***, LHC Project Document **LHC–MB A–C1–0006**.

[2.17] M. Baiko et al, "*Status report on the superconducting dipole magnet production for the LHC*", presented in Applied Superconductivity Conference 2006, Seattle, WA, USA.

Chapter 3

The magnetic field

The starting point of this chapter is the general expression for the magnetic field in an empty space and the definition of the magnetic field harmonics. Then from the general expression for the magnetic field in the aperture of a magnet we obtain the current distribution needed to generate a perfect multipole field of the order *n*. It is shown that a perfect dipole field can be approximated by means of a shell configuration of multistrand Rutherford-type cables. The influences of the geometry and the iron joke on the field harmonics are computed and the main sources of magnetic field errors are discussed. Furthermore the technique of harmonics measurement with roating coil is presented and the limits imposed by the beam dynamics on the LHC main dipole both at room temperature and at 1.9 K are given.

3.1 Magnetic field and field harmonics

In region free of any current and magnetized material, a stationary magnetic field, $\vec{B}=(B_x,B_y,B_t)$ fulfils the Maxwell equations:

$$\vec{\nabla}\cdot\vec{B}=0$$
$$\vec{\nabla}\times\vec{B}=0 \qquad \text{Eq. 3.1}$$

These two equations imply the existence of a scalar magnetic potential $V(x,y,z)$, and a vector potential $\vec{A}=(A_x,A_y,A_t)$ that satisfy:

$$\vec{B}=-\vec{\nabla}V$$
$$\vec{B}=\vec{\nabla}\times\vec{A} \qquad \text{Eq. 3.2}$$

Let us assume that the magnetic field has the component $B_t = 0$; the problem becomes two-dimensional with $\vec{A}=A_t$ and $\partial V/\partial z = 0$. We call x and y two orthogonal Cartesian axis and t the axis perpendicular to the plane (x,y). As consequences of these assumptions, the two non-zero components of the magnetic field can be written as:

$$B_x = -\frac{\partial V}{\partial x} = \frac{\partial A_z}{\partial y}$$
$$B_y = -\frac{\partial V}{\partial y} = -\frac{\partial A_z}{\partial x} \qquad \text{Eq. 3.3}$$

Using a complex notation for the magnetic field function $B(x,y) = B_y(x,y) + iB_x(x,y)$, it can be easily proven that it is analytic since it satisfies the Cauchy-Riemann conditions:

$$\frac{\partial B_x}{\partial x} = -\frac{\partial B_y}{\partial y}$$
$$\frac{\partial B_x}{\partial y} = \frac{\partial B_y}{\partial x} \qquad \text{Eq. 3.4}$$

A fundamental propriety of the analytic functions is that their power series is convergent:

$$B(x,y) = \sum_{n=1}^{\infty} C_n z^{n-1} \qquad \text{Eq. 3.5}$$

where $z=x+iy$. The domain of convergence is a circle whose radius is given by the location of the first singularity (for instance the analytic function $f(z) = (1-z)^{-1} = \sum_{n=1}^{\infty} z^n$ is convergent for $|z|<1$). The complex coefficients of the series C_n can be written as:

$$C_n = B_n + iA_n \qquad \text{Eq. 3.6}$$

and B_n and A_n are the *field harmonics* or *multipoles*. In the following section an example of magnetic field harmonics calculation for a simple case is given.

The 2-dimensional approximation is very accurate to calculate the field in the straight part of a magnet featuring a small diameter/length ratio. This is usually the case for the large accelerator magnets that are several meters long with a coil bore of the order of few centimeters. For instance, the LHC dipoles and quadrupoles are 15 and 3.25 m long respectively with a coil diameter of 0.12 m. So in these cases one can consider the field in the (x,y) plane and neglect its t component.

The field computation in the magnets end is rather complex since a t component is present: analytical expressions of the field are difficult to be worked out (see [3.1]) and 3-dimensional finite element calculations are required to have precise estimations. However, the longer is the magnet the lower is the impact of the magnetic field of the magnet heads.

3.1.1 Field harmonics of a current line

The magnetic field in $z=x+iy$ of a single current line in the position $z_c=x_c+iy_c$, can be written, using the Biot-Savart law in a complex notation:

$$B(z)=\frac{\mu_0 I}{2\pi(z-z_c)} \quad ; \quad B=B_y+iB_x \qquad \text{Eq. 3.7}$$

where the field is in Tesla, μ_0 is the magnetic permeability in the vacuum ($4\pi 10^{-7}$ kg·m/s^2/A^2), I is the current in Ampere and with sign, z is the complex coordinate ($re^{i\theta}$), and the z_c ($r_c e^{i\theta c}$) is the coordinate of the current line in meters.

Since the Eq. 3.7 is an analytic function on $|z|< z_c$ it can be expanded in $z=0$, from Eq. 3.6 and Eq. 3.7:

$$B(z)=\sum_{n=1}^{\infty}\left(-\frac{\mu_0 I}{2\pi}\frac{1}{z_c^n}\right)z^{n-1}=\sum_{n=1}^{\infty}C_n z^{n-1}=\sum_{n=1}^{\infty}(B_n+iA_n)z^{n-1} \qquad \text{Eq. 3.8}$$

and therefore:

$$\begin{aligned} C_n &= \frac{\mu_0 I}{2\pi}\frac{1}{r_c^n}e^{in\theta_c} \\ B_1 &= \frac{\mu_0 I}{2\pi}\frac{1}{r_c}\cos\theta_c \end{aligned} \qquad \text{Eq. 3.9}$$

Since magnets usually aim at producing only main component (pure n-polar field) the quality of the magnetic field is expressed in terms of dimensionless *normalized complex coefficients* c_n, or of the real - b_n - and imaginary - a_n - parts respectively called **normal** and **skew** magnetic field **harmonics** [3.2]:

$$B(z)=B_{ref}10^{-4}\sum_{n=1}^{\infty}c_n\left(\frac{z}{R_{ref}}\right)^{n-1}=B_{ref}10^{-4}\sum_{n=1}^{\infty}(b_n+ia_n)\left(\frac{z}{R_{ref}}\right)^{n-1} \qquad \text{Eq. 3.10}$$

where the R_{ref} is the reference radius and normally is taken equal to 2/3 of the considered aperture [wilson] and B_{ref} is the value of the main component (dipole in our example - B_1) of Eq. 3.9. Normally the values of the multipoles are four-five orders of magnitude smaller than the B_{ref} and for this reason they are rescaled by a factor of 10^4, i.e. $b_1=10^4$ by definition for a dipole.

Using Eq. 3.10 one obtains a simple formulation of the normalized coefficients in the origin of the reference system of a current line placed in $z_c=r_c e^{i\theta c}$:

$$b_n=\frac{R_{ref}^{n-1}}{r_c^{n-1}}\frac{\cos(n\theta_c)}{\cos(\theta_c)}\cdot 10^4 \quad ; \quad a_n=-\frac{R_{ref}^{n-1}}{r_c^{n-1}}\frac{\sin(n\theta_c)}{\cos(\theta_c)}\cdot 10^4 \qquad \text{Eq. 3.11}$$

The coefficients C_n are linear, whereas the normalized one (c_n) are not: let us define the complex coefficients C_n' and c_n' of a current line; if we add a second current line, and we define its C_n'' and the normalized coefficients c_n'' the coefficients of the two lines together are $C_n = C_n' + C_n''$ but $c_n \neq c_n' + c_n''$.

3.1.2 Generation of pure multipole field

From Eq. 3.11 it is evident that a single current line generates multipole of any order n. In order to generate pure m-component field a special arrangement of the current lines must be considered. Using the orthogonality of the trigonometric functions, a pure multipole field, containing just the single order $n=m$, is obtained if an azimuthal current sheet (having an infinitesimal width) distribution on a circle $z=r_c e^{i\theta c}$ satisfies:

$$I(\theta_c) = I_o \cos(m\theta_c) \qquad \text{Eq. 3.12}$$

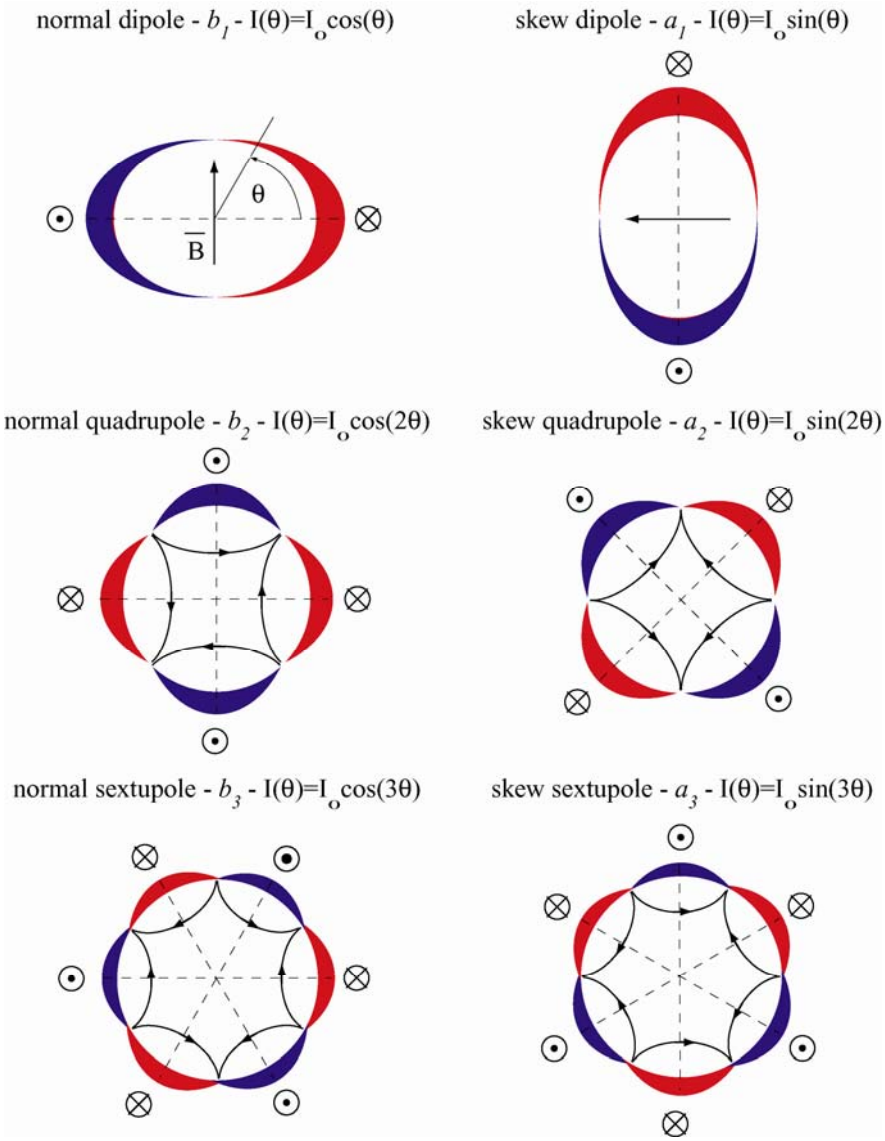

Figure 3.1: Generation of pure multipole fields by current sheet with a distribution of cos($m\theta$) and sin($m\theta$).

In fact, one has:

$$B(z)=\sum_{n=1}^{\infty}\left[4\cdot\int_{0}^{\pi/2}\frac{\mu_0|I_0|\cos(m\theta)}{2\pi}\frac{1}{r_c^n}\left(\cos(n\theta)-i\sin(n\theta)\right)d\theta\right]\cdot z^{m-1}=\frac{\mu_0 I_o}{2r_c^m}z^{m-1} \qquad \text{Eq. 3.13}$$

for m=1,2,3 one can obtain a dipole, a quadrupole and a sextupole field, respectively. By substituting the sine to the cosine a skew pure field can be generated, see Figure 3.1.

Current distributions with a cos($m\theta$) dependence are difficult to fabricate with a superconducting cable of constant cross section. In the next section we discuss how a dipole field can be approximated with a simple case of four wires dipole and a more realistic shell configuration.

3.2 Dipole field

Four current line dipole

The simplest way to construct a dipole magnet, having an aperture hosting in principle a particle beam, is to overlap two identical spires carrying the same current (the 2D approximation is valid far from the end of the spires) . Looking at a cross section (see Figure 3.2 – left): a current line $+I$ is placed an angle ϕ, the other three are: $+I$ at an angle $-\phi$, $-I$ at $\pi-\phi$ and $-I$ at $\pi+\phi$ ($+I$ means that the current enters the plane of the cross section). Appling equation Eq. 3.10 one can derive the expression for the multipoles, Eq. 3.14. It can be proven that respecting these symmetries only the normal multipoles of order n = (2k+1) are present (k=0,1,2,3…).

$$\begin{aligned}C_n=\frac{\mu_0}{2\pi}\frac{I}{r_c^n}\big[&\left(\cos(n\varphi)+\cos(n(-\varphi))-\cos(n(\pi-\varphi))-\cos(n(\pi+\varphi))\right)+\\&+i\left(-\sin(n\varphi)-\sin(n(-\varphi))+\sin(n(\pi-\varphi))+\sin(n(\pi+\varphi))\right)\big]=\\&=\frac{\mu_0}{2\pi}\frac{I}{r_c^n}\big[\left(\cos(n\varphi)+\cos(n\varphi)+\cos(n\varphi)+\cos(n\varphi)\right)+\\&+i\left(-\sin(n\varphi)+\sin(n\varphi)+\sin(n\varphi)-\sin(n\varphi)\right)\big]=\\&=\frac{\mu_0}{2\pi}\frac{I}{r_c^n}4\cos(n\varphi)\qquad\qquad n=2k+1;\quad k=0,1,2,...\end{aligned} \qquad \text{Eq. 3.14}$$

Dipole shell configuration

The current shell approximation takes into account the same symmetry features to generate a dipole magnetic field, Figure 3.2 - center. The current is carried by two shells of a radial thickness r_e-r_i and an azimuthal extension from 0 to ϕ carrying the same current density j with different sign. The computation of the field multipoles can be derived using Eq. 3.10:

$$C_n=4\frac{\mu_0 j}{2\pi}\int_0^{\varphi}\int_{r_1}^{r_2}\frac{1}{r_c^n}\left(\cos(n\theta)-\sin(n\theta)\right)2\pi r_c\,\mathrm{d}r\mathrm{d}\theta \qquad \text{Eq. 3.15}$$

One can proves that if current shells with dipole symmetry are made with limiting angle of $\phi = 60^o$, the sextupole (b_3) vanishes. A single layer current shell arrangement with constant density can provide a field quality not enough optimized since it leaves a strong b_5. In magnet construction, to increase the magnetic field strength, another layer can be added, Figure 3.2 – right, [3.1].

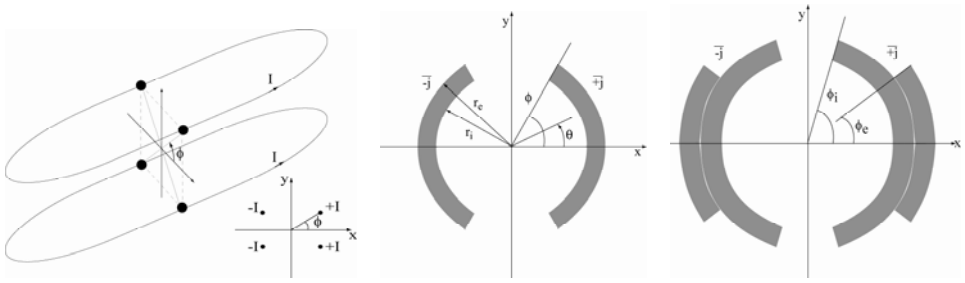

Figure 3.2: Four current lines with dipole symmetry - left. Simplest current shell arrangements for a dipole coil, $\phi=60^o$ to vanish b_3 - center; two layers dipole configuration - right.

Dipole magnets

A further control on field quality is achieved by introducing in the coils some wedges between the superconducting cables. This gives the opportunity to minimize the contribution of a number of allowed multipoles that it is proportional to the number of wedges inserted. Normally Rutherford cables with trapezoidal shape are used to approximate the circular shape of a shell, and they are constituted by a certain number of strands carrying the current. To save computing time to have a realistic estimation of the multipoles it is sufficient to sum algebraically the contributions of each current lines of each cable of the cross section, that is:

$$C_n = \sum_{s=1}^{N} \frac{\mu_0 I_s}{2\pi} \frac{1}{r_s^n} \left(cos(n\theta_s) - \mathrm{i}\, sin(n\theta_s)\right) \qquad \text{Eq. 3.16}$$

where N is the number of strands per cable multiplied for the number of cable in the cross section; (r_s, θ_s) are the radial and azimuthal position of the strands.

As examples, in Figure 3.3 the dipole cross sections of Tevatron [3.3], HERA [3.4] and RHIC [3.5] are shown and the value for b_3, b_5 and b_7 defined by their geometry are given.

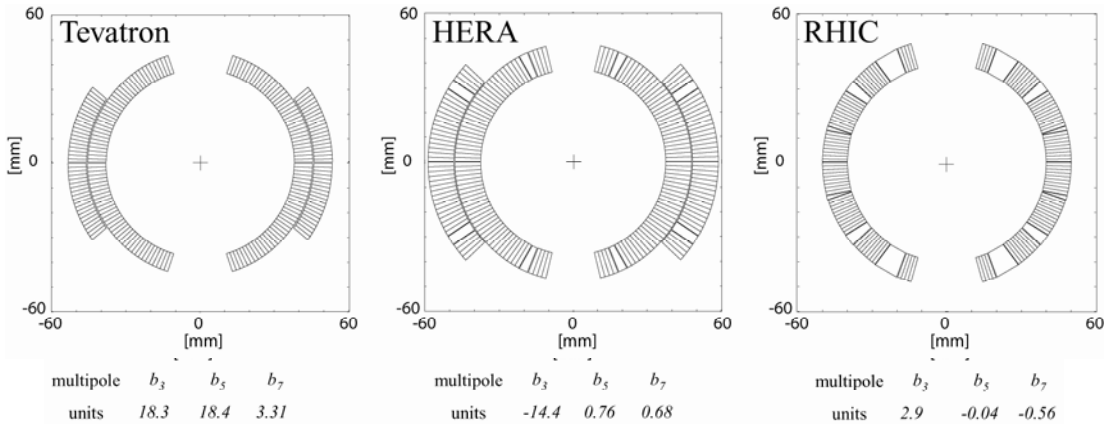

Figure 3.3: Tevatron, HERA and RHIC dipole cross section with the field quality by design

3.2.1 Field harmonics of a dipole magnet

Due to mechanical tolerances, one will never match perfectly the coil design. Therefore, in real dipole magnets the multipoles differ from the nominal ones. If the coil symmetries are broken, also non allowed harmonics are generated.

For a dipole coil geometry one can split the multipoles in 4 classes with respect to the symmetries of the geometry that can affects them as shown in Figure 3.4, [3.6]:

- **Odd normal:** b_3, b_5, b_7…b_{2n+1}: are generated by Up-Down and Left-Right symmetry.
- **Even normal:** b_2, b_4, … b_{2n}, are generated by a Left-Right anti-symmetry and a Up-Down symmetry.
- **Odd skew:** a_3, a_5, a_{2n+1} are generated by Up-Down and Left-Right anti symmetry.
- **Even skew:** a_2, a_4, … a_{2n} are generated by a Left-Right symmetry and a Up-Down anti symmetry.

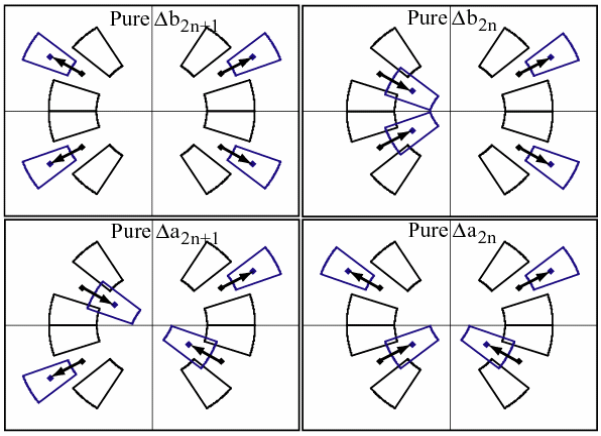

Figure 3.4: Pure geometrical and independent generation of the four classes of field harmonics.

3.2.2 Field harmonics induced by iron yoke

The high field superconducting magnets for accelerator are equipped with an iron yoke to confine the magnetic field. Its influence on the magnetic field given by the coil can be computed with the method of the image currents, assuming that the iron is not saturated (this is valid when, B < 2 T [3.1]) and the magnetic permeability μ is uniform.

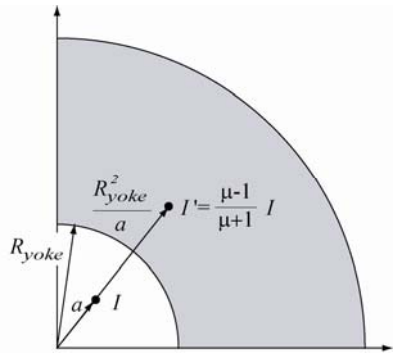

Figure 3.5: Method of the image current to evaluate the effect of the iron yoke - gray part - on the magnetic field at room temperature.

Let us consider a current line I in a position $z_l=ae^{i\varphi}$ from the origin of the reference system and a iron yoke having a inner radius R_{yoke} see Figure 3.5 . One can prove that the effect of the iron on the magnetic field is equivalent to that of an image current I'

$$I' = \frac{\mu - 1}{\mu + 1} I \qquad \text{Eq. 3.17}$$

located at

$$z_l^{'} = \frac{R_{yoke}^2}{z_l^*} = \frac{R_{yoke}^2}{a} e^{i\varphi} \qquad \text{Eq. 3.18}$$

Therefore, the additional component of the magnetic field due to the iron yoke is:

$$B_{yoke}(z) = \frac{\mu_0 I}{2\pi} \frac{\mu - 1}{\mu + 1} \frac{1}{z - \frac{R_{yoke}^2}{z_l^*}} \qquad \text{Eq. 3.19}$$

and the amplitudes of the effect on the field multipoles are (derived following Eq. 3.8 and Eq. 3.9):

$$C_{n,\,yoke} = -\frac{\mu_0 I}{2\pi z_l^n} \left[\frac{\mu - 1}{\mu + 1} \frac{|z_l|^{2n}}{R_{yoke}^{2n}} \right] \qquad \text{Eq. 3.20}$$

Since the magnetic permeability of the iron is quite large (for LHC yoke ~ μ=1000 kg·m/s^2/A^2) one can assume that

$$\frac{\mu - 1}{\mu + 1} \approx 1 \qquad \text{Eq. 3.21}$$

Therefore, for a current line, the iron yoke increases the main field of a factor $[1+(a/R_{\text{yoke}})^2]$. The image current method provides a good estimation of the yoke contribution to the field shape for a magnet with a single aperture fully surrounded by the iron at low field. When the iron starts saturating (B ~ 2 T), the assumption of a constant μ is not more valid; actually it strongly depends on the local field, which is not uniform in the yoke. No precise analytical solution exists and several finite element codes have been developed during the past 30 years (OPERA, Tosca, ROXIE…) to perform magnetic computations in this regime.

In the LHC case, the multipoles induced by the iron yoke in the cold mass assembly can be obtained from the measured multipoles of the collared coil (i.e. without the yoke) by mean of:

$$b_{n,cm} = kb_{n,cc} - b_{n,cm-cc} \qquad \text{Eq. 3.22}$$

where *cm* stands for cold mass and *cc* for collared coil. In this way we single out anomalies in the cold mass assembly only, the collared coil anomalies having already being pointed out by the corresponding measurement. The effect of the iron yoke is to increase the main field by a factor k=1.18 (for LHC) in the straight part and by k=1.12 in the coil heads. Therefore the multipole values in the cold mass are reduced by 1/k and then the rescaled control bounds for collared coil magnetic measurements are calculated according to the following expression [3.21]:

3.3 Sources of field errors

Field errors have different origins: geometry errors, iron saturation, coil deformations under electro magnetic forces, persistent and eddy currents.

a) Geometry errors

The field errors originating from misplacements of conductors can be computed analytically at the design stage from the manufacturing tolerances. Sensitivity matrices are computed for displacement of single conductors or conductor blocks. Some examples are given for LHC dipole magnet in terms units of Δb_n and Δa_n, defined, as usual for magnetic calculation of LHC main magnets, at the reference radius R_{ref} = 17 mm:

- a 0.1 mm reduction of the coil azimuthal size of the inner layer with constant current and coil thickness, produces a Δb_3 = 2.18, Δb_5 = -0.40 and Δb_7 = 0.15 units [3.7]
- a 0.1 mm difference of azimuthal coil dimension between upper and lower pole of the same aperture produces Δa_2 = 5.28 and Δa_4 = 0.80 units [3.8]
- a shift of 0.1 mm of the outer circular surface of the austenitic steel collars gives Δa_3 = -2.42 and Δa_5 = -0.22 units [3.9].

From these examples one can understand how difficult is to obtain in superconducting magnets a field quality comparable to that of classical lower field magnets, where the field distribution is determined by the iron-pole profiles which can be easily produced with a hundredth-millimeter precision. In superconducting magnets the coil geometry is the result of assembling stacks of conductors, typically 15 to 30, which are produced with stringent, but not infinitely small, tolerances (in cables the best that can be achieved nowadays is of the order of $\pm$ 0.0025 mm on the thickness [3.10]) and insulated by wrapping them with tapes which can be industrially produced with a few micrometers tolerance on their thickness. Moreover the assembly of the coil under high loads and the voids of the cables make very difficult the geometry control.

b) Iron saturation

The field errors originating from the magnetic permeability vary with excitation and depend strongly on the coil-yoke distance. For warm iron magnets (e.g. Tevatron

dipoles) these errors can be neglected in practice. For cold iron magnets (as LHC dipoles) they have to be carefully evaluated.

c) Coil deformation under due to electro magnetic forces

These errors vary with excitation and can be estimated after the mechanical analysis of the structure and the determination of the deformed coil configurations, using analytical or other computer programs [3.10].

d) Persistent currents in the superconductors

The persistent current errors are a feature of superconducting magnets. They are due to currents induced in the superconducting filaments by field variations and, contrary to normal conductors where resistance rapidly reduces and after a while eliminates eddy currents, circulate indefinitely as long as the superconductor is kept below its critical temperature. Persistent current errors affect all field multipole components allowed by the symmetry configuration of the magnet, including the fundamental one. Their importance decreases with excitation, but they are particularly strong at low field level and especially at injection. They depend on the previous powering of the magnet and vary with time and, therefore, require a careful study of the magnet excitation cycle. Persistent currents are proportional to the effective diameter of the superconducting filaments, so accelerator magnets use filaments as thin as possible, compatibly with cost and quality of production.

Typically the magnetic errors due to the persistent currents are partially corrected with the geometry; magnet cross sections are designed in order not to nullify the allowed multipoles which compensate these errors. The nominal LHC dipole cross-section, for instance, has been chosen to generate a non-zero value of the low order odd multipoles which partially compensates the effect of the persistent currents [3.11]. The effect of the persistent currents is of about -8.0 units for the b_3, about 1.0 unit for the b_5 and about -0.4 units for the b_7 at the injection and it disappears at nominal field.

e) Eddy currents

Eddy currents occur during field sweep in multi-strand conductors both inside the strands, mainly due to coupling between filaments, and between the strands [3.12]. They distort the magnetic field, and their effects depend on the geometrical and electrical characteristics of strands and cables (matrix and inter-strand resistance, cable aspect ratio, distribution of superconducting filaments, etc.) and, of course, on the field ramp rate.

3.4 Magnetic field measurement

Once a coil has been designed and manufactured, its field quality can be analyzed by magnetic measurements. The magnetic field in the straight part of a dipole as shown in Figure 3.6 can be considered two-dimensional and to evaluate the field quality inside the beam channel, the multipolar expansion can be written as:

$$B(x,y) = B_{ref}\,10^{-4}\sum_{n=1}^{\infty} c_n \left(\frac{z}{R_{ref}}\right)^{n-1} = B_{ref}\,10^{-4}\sum_{n=1}^{\infty}\left(b_n + ia_n\right)\left(\frac{x+iy}{R_{ref}}\right)^{n-1} \qquad \text{Eq. 3.23}$$

For superconducting accelerator magnets, usually it is needed a field uniformity corresponding to multipoles b_n, a_n of the order of 10^{-4} (with the exception of b_1 which is set to one by definition). The field quality for the LHC dipole magnets must be controlled up to 10-100 ppm, i.e. 1-0.1 units [3.13]. The magnetic measurements performed on LHC superconducting magnets are performed twice in the magnet assembly chain: at room temperature (around 300 K) and at cryogenic temperature (4.4 and 1.9K).

3.4.1 Magnetic measurement at room temperature

The magnetic measurements at room temperature (around 300 K) are performed by exciting a magnet coil in its normal conducting state with a low current (of the order of 10 A). In such way, measurements are carried out during industrial series production, even if the magnet is still far from the final assembly. The LHC dipoles undergo two measurements at room temperature during their assembly chain:

- one on the collared coils
- one on the cold mass

These measurements are a powerful tool to detect assembly errors or faulty components at an early stage of production. Moreover, they give a relevant indication of the field quality in operational conditions. The magnetic content differs from collared coil to cold mass due to the presence of the yoke whose estimation has been given in previous section. Here some issues related with the measurements of the collared coil are discussed, but the same can be repeated for the cold mass, since the two measurements are similar and the equipment is exactly the same.

A precise measurement of the low magnetic field (~0.01 T) induced by a low electric current (~10 A) in the collared coils is made using the technique of rotating search coils and harmonic analysis [3.14],[3.15]. The rotating coils are mounted in a so-called *magnetic mole* which is inserted in the aperture. For the LHC dipoles, coils within the probe are 750 mm long. In order to cover the whole length of the collared coil (~15 m), a full set of measurements is performed on 20 positions along the coil axis. The main components of the field-measuring probe are: three rotating *search coils* (see Figure 3.6), an incremental encoder, an electronic gravity sensor and a pneumatic brake. The encoder, mounted on the coil rotation axis, determines their angular position with an accuracy of the main field direction better than 0.1 mrad. The reference axis of the coils is adjusted by rotating the whole mole according to the electronic gravity sensor. The mole is held in position during the measurement by a pneumatic brake.

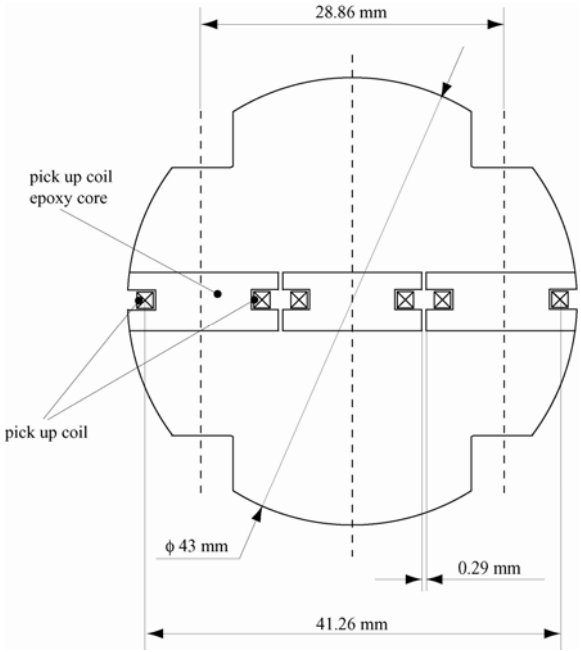

Figure 3.6: Rotating search coil cross section

Search coils are made of three identical coils, mounted side by side, the central one being centered on the rotating axis. They are made of 20-wire flat cable wound onto a fiberglass reinforced epoxy core. When inside a magnetic field, coils rotate to produce a voltage proportional to the flux and to the speed of rotation. Series of ten measurements are carried out at each longitudinal position, five at positive current and five at negative current in order to cancel iron magnetization and earth field effect [3.14]. The signal from the outward coil (absolute signal) is used to determine the main component. On the other hand, the field harmonics are calculated from a combination of signals coming from different coils. The system includes also two *motors* (one for rotating the coil and one for leveling the mole with respect to gravity) and an *acquisition system*. Once a magnetic measurement has been carried out the harmonic coefficients (i.e. multipoles) are reconstructed by means of a Discrete Fourier Transform [3.14].

The parameters taken over each of the 20 positions along the two collared coil apertures are here listed:

- C_1, main field component in [T];
- *Angle*, main field component direction with respect to the gravity in [mrad];
- b_n and a_n, normal and skew multipoles up to the order 15^{th}
- D_x and D_y, coordinates of the magnetic axis with respect to the mechanical one of the measured aperture in [mm]. They are determined by assuming that the not-allowed harmonics a_{10} and b_{10} are only due to first order feed down of b_{11} harmonics (see [3.16] for further reading).

When a particle beam crosses a dipolar field nearly at the speed of light, its motion is mainly affected by the average magnetic field in the magnet straight part, if there are no strong multipolar variations, and the short magnet heads have limited influence on the field quality. For the LHC dipole, measurement position 1 and 20 are

in the magnet heads. Measurement positions 2 to 19 are along the so-called *straight part*. Accelerator physicists are therefore interested in values integrated along the magnet straight part to qualify the overall LHC machine performance. Magnetic measurements at room temperature provide such values, which can be used to characterize the aperture as a whole:

- *Magnetic Length*:

$$M_L = \frac{\int_{-\infty}^{+\infty} C_1 dl}{\langle C_1 \rangle} \qquad \text{Eq. 3.24}$$

  where $\langle C_1 \rangle$ is the average of the main field component along the so-called straight part. It is computed along the whole aperture axis.

- *Transfer Function* (*TF*):

$$TF = \frac{\langle C_1 \rangle}{I} \qquad \text{Eq. 3.25}$$

  it is the average transfer function in the straight part (in T/A); I is the DC current used for measurements (10-8.5 A at room temperature).

- *Integrated multipoles*: for a generic multipole b_n (a similar equation holds for the skew multipoles a_n), its integrated value is defined by the following equation:

$$\langle b_n \rangle = \frac{\int_{-\infty}^{+\infty} b_n C_1 dl}{\int_{-\infty}^{+\infty} C_1 dl} \qquad \text{Eq. 3.26}$$

Coil waviness: multipolar variations along the magnetic axis can be summarized in a scalar value in microns which is called the coil waviness. This is the amplitude (one sigma) of random movements of the blocks that give the closest values to the measured multipole spread according to simulations [3.17]. Empirical control limits are set at 30 micron and 60 microns. The coil waviness computed from the difference of cold mass and collared coil is also used to recognize if the cold mass really contains the corresponding collared coil. This check is very effective since the coil waviness allows to checking the pattern of field variations along the axis that are a fingerprint of the magnet.

3.4.2 Magnetic measurement at 1.9 K

During magnetic measurements at cryogenic temperature, the field quality in operational conditions of temperature (for LHC dipoles, 1.9 K) and electric current (for LHC dipoles, from 760 A to 11.8 kA) is measured. These kind of magnetic measurements imply, therefore, that the magnet must be assembled in its cryostat. Special benches have been developed at CERN to perform the tests. The probe used for measurements is usually anti-cryostatized to avoid calibration problems.

The measurements are performed following a so-called “loadline curve” preceded by a “precycle” (see Figure 3.7, left): the magnetic field is ramped from zero up to

8.4T then ramping down to a minimum field of 0.25 T, corresponding to a current of 350 A – pre-cycle - then the field is ramped up to 8.33 T (11850 A) and then again to 350 A by 35 steps. The steps last 140 s in order to avoid all transient effects and to perform the measurement. At each step of the load line the integrated transfer function, the local and the integrated field are obtained. In general at each plateau the quantities measured at room temperature are taken [3.18].

Following a measurement of a multipole along the loadline it is possible to distinguish the different source of the effect on the multipole; for instance, in Figure 3.7 the b_3 is reported. We define:

- b_3^{inj} the measurement performed at the LHC current injection level, 760 A
- b_3^{geo} the multipole geometric component defined as the average of the two measurement of b_3 of the ramp-up and ramp-down of the load line branches at 5000 A. At this current level the persistent current effect is almos negligible and the iron is not yet saturated, then the major source of field error is the geometry of the coil.
- b_3^{high} the multipole component measured at the top current – 11850 A.
- $b_3^{per} = b_3^{inj} - b_3^{geo}$ the multipole component due to persistent current.
- $b_n^{iron\_lf} = b_3^{high} - b_3^{geo}$ the multipoles component due to the iron saturation of the surrounding yoke and the deformation caused by the Lorentz forces.

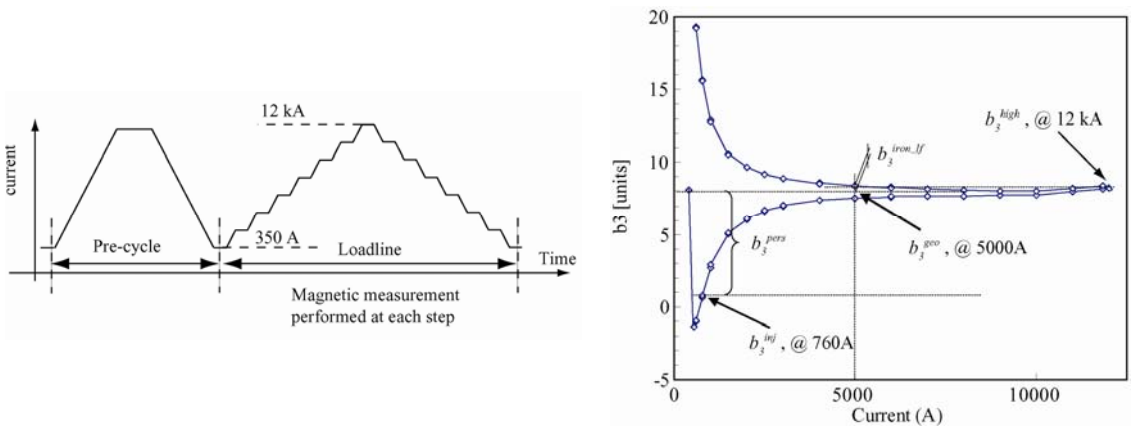

Figure 3.7: Pre-cycle and loadline curve – left; Measurement of b_3 along the loadline, the salient point are evidenced.

3.4.3 Control limits for field quality of LHC main dipoles

The control limits on field quality are given by beam dynamics, the criteria being to evaluate the maximum instabilities that the beam can withstand [3.19]. The Specifications for the LHC main dipoles field harmonics are summarized in Table 3.1.

Table 3.1: Specification for the dipole field quality at injection and high filed

	Injection (450 Gev – 760 A)		High field (7 TeV – 8.33 T)	
	Systematic	Random	Systematic	Random
b_1	-	8.0	-	8.0
b_2	±1.4	0.7	±1.4	0.8
b_3	±10.5	1.4	±3.0	1.8
b_4	±0.2	0.5	±0.2	0.5
b_5	±1.1	0.5	±0.8	0.4
b_6	-0.06< b_6<0	0.3	-0.07< b_6<0	0.08
b_7	-0.3< b_7<0.1	0.2	-	0.2
a_1	±6.5	8.0	±6.5	8.0
a_2	0	1.9	0	1.6
a_3	0	0.7	0	0.7
a_4	0	0.5	0	0.5
a_5	0	0.4	0	0.4
a_6	0	0.1	0	0.15
a_7	0	0.2	0	0.07

The limits are considered for the entire production and they are imposed on the systematic and random part of the field harmonics. For *systematic* we indicate the average of a field harmonics evaluated over a certain set of magnets and the r.m.s. is the random part. For instance in Figure 3.8 the measurement of the harmonic a_2 over the whole LHC dipole production is plotted; each point represents a measured aperture; the average of the distribution is the systematic component (0.35 units) and the standard deviation is the random component.

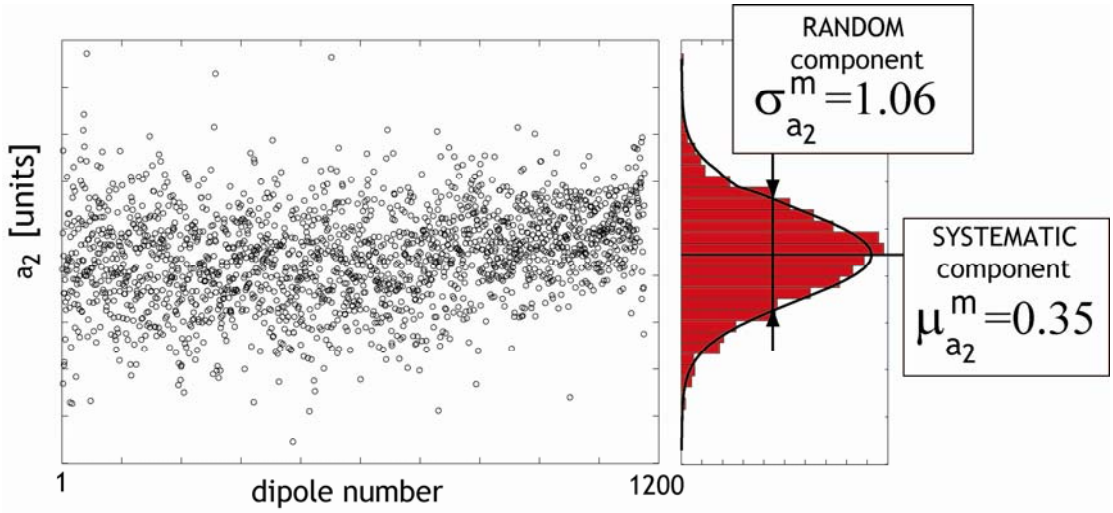

Figure 3.8: Definition of systematic and random components of a filed harmonic.

In order to steer the production using room temperature measurements, one needs to transfer the target ranges from the two operational conditions to warm measurements. The offset between injection field (or high field) and room temperature measurement of the cold mass can be written as the average over all magnets measured both at 1.9 K and at room temperature:

$$b_n^{off,inj} = \overline{b_n^{inj} - b_n^{cm}} = \overline{b_n^{inj} - b_n^{@\,5000\,A}} + \overline{b_n^{@\,5000\,A} - b_n^{cm}} = \overline{b_n^{pers}} + \overline{b_n^{off,geo}}$$
$$b_n^{off,high} = \overline{b_n^{high} - b_n^{cm}} = \overline{b_n^{high} - b_n^{@\,5000\,A}} + \overline{b_n^{@\,5000\,A} - b_n^{cm}} = \overline{b_n^{iron\_lf}} + \overline{b_n^{off,geo}} \qquad \text{Eq. 3.27}$$

where the terms $b_n^{off,geo}$ represent the change of the geometric component between the room temperature and the 1.9 K configuration. The targets on the cold mass harmonics (b_n^{cm}) at room temperature (Eq. 3, 4) are the intersection of the limits given by the beam dynamics at injection (b_n^{inj}) and at high field (b_n^{high}) [3.20] projected at room temperature through the previously defined offsets, and taking into account also the effect of the beam screen (b_n^{BS}):

$$b_{n,low\,lim}^{cm} = max\left(b_{n,low\,lim}^{inj} - b_n^{off,inj}; b_{n,low\,lim}^{high} - b_n^{off,high}\right) - b_n^{BS}$$
$$b_{n,upper\,lim}^{cm} = min\left(b_{n,upper\,lim}^{inj} - b_n^{off,inj}; b_{n,upper\,lim}^{high} - b_n^{off,high}\right) - b_n^{BS} \qquad \text{Eq. 3.28}$$

In order to have a fast feedback, magnetic measurements are also performed at the stage of collared coil. The limits are computed considering the difference between the cold mass and the collared coil measurements as explained in section 1.2.2 and given in Table 3.2. For the even normal harmonics the limits are given for each aperture and also for the average of the two apertures.

Table 3.2: Control limits for the field quality of the LHC cold masses and collared coils.

	cold mass			collared coil		
	Lower lim.	Upper lim.	Random	Lower lim.	Upper lim.	Random
b_2 -ap 1	1.09	3.22	0.8	-2.28	0.24	0.9
b_2-ap 2	-3.29	-1.15	0.8	-0.34	2.17	0.9
b_2-av.	-0.47	0.30	0.8	-0.49	0.42	0.9
b_3	3.65	0.79	1.4	-4.48	1.12	1.7
b_4 -ap 1	-0.37	0.25	0.5	-0.56	0.17	0.6
b_4-ap 2	-0.26	0.36	0.5	-0.26	0.21	0.6
b_4-av.	-0.20	0.19	0.5	-0.5	0.5	0.6
b_5	-0.94	0.22	0.4	-1.14	-0.3	0.5
b_7	0.26	0.66	0.2	-0.79	-0.31	0.2
a_2	-0.79	0.92	1.2	-0.66	1.35	1.9
a_3	-1.4	1.4	0.7	-1.65	1.86	0.8
a_4	-0.14	0.14	0.5	-0.11	0.19	0.6
a_5	-0.41	0.39	0.4	-0.47	0.48	0.5

References

[3.1] A. V. Tollerstrup, "*The amateur magnet's builder handbook*", Fermilab, UPC 086.

[3.2] M. N. Wilson, "*Superconducting magnets*", Calderon Press, Oxford, 1986

[3.3] P. Bauer et al, "*Tevatron magnetic Models Geometric and Hysteretic Multipoles in the Tevatron Dipole*" Fermilab Internal Note **TD-02-040** (**2004**).

[3.4] *B.H. Wiik, "Design and Status of the HERA Superconducting Magnets",* Progress in high Temperature Superconductivity, **Vol 8**, Ed. C.G. Burnham, R.D. Kane, World Scientific, World Congress on Superconductivity, (**1988**).

[3.5] P. Wanderer et al, "*The RHIC magnet system*", Nuclear Instruments and Methods in Physics Research, **A 499** (**2003**) pp. 280-315.

[3.6] Rob Wolf, "*Field error naming conventions for LHC magnets*", CERN LHC-MMS/98-198 Rev. 2.0, CERN, **1998**, **Annex F1**.

[3.7] P. Ferracin, "*Mechanical and magnetic analysis of the Large Hadron Collider main dipole*", CERN-**Thesis-2002-009**.

[3.8] S. Pauletta, "*Field quality analysis to monitor the industrial series production of the dipole magnets for the Large Hadron Collider"* **CERN-Thesis-2003-002**

[3.9] B. Bellesia "*Influence of Austenitic Steel Collar Dimensions on Magnetic Field Harmonics in the LHC Main Dipole*", CERN **LHC-Project-Note-377**, **2005**

[3.10] R. Perin, *"Field, forces and mechanics of superconducting mgnets"*, CERN Accelerator School, **CERN 96-03**

[3.11] R Bartolini, "*Magnetic errors of the LHC dipoles and possible cures*" **CERN-OPEN-2000-147.**

[3.12] A. Devred and T. Ogitsu, *"Influence of eddy currents in superconducting particle accelerator magnets using Rutherford-type cables"*, CERN Accelerator School, **CERN 96-03**.

[3.13] E.Todesco, "*Status report on field quality in the main LHC dipoles"*, Proceedings of European Particle Accelerator Conference, **2002, JAcoW**.

[3.14] J.Billan et al., "*Magnetic measurements of the LHC quadrupole and dipole magnets at room temperature*", CERN **LHC-Project-Note-283**, **2002**.

[3.15] K.N. Henrichsen, "*Overview of magnet measurement methods*", **CERN Report 98-05**.

[3.16] S.Gleis et al, "*Analysis of warm magnetic measurements in a LHC main dipole prototype*", CERN **LHC-Project-Report-352**, **1999**.

[3.17] P. Ferracin, "*Modeling of random geometric errors in superconducting magnets with applications to the CERN Large Hadron Collider*" CERN **LHC-Project-Report-460**, **2001**.

[3.18] S. Filippo et al., "*Magnetic measurements for 15 m long dipoles – standard program of cold test "* LHC **MTA-IN-2001-169**.

[3.19] F. Fartoukh, O. brunning, "*Field quality specification for the LHC main dipole magnets*", CERN **LHC-Project Report 501**, **2001**.

[3.20] R. Wolf, S. Le Naour, *"The Expected Persistent Current Field Errors in the LHC Main Dipole and Quadrupole"*, **LHC, Project-Note-230**, **2000**.

[3.21] E. Todesco, " Status report on field quality in the main LHC dipoles" CERN, **LHC-Project-Report-579,** 2002.

Chapter 4

Superconducting cables

This is the first of three chapters where the influence on the magnetic field of the main components of the LHC collared coil - superconducting cables, coil copper wedges and coil retaining collars - is evaluated. Here the attention is focused on superconducting cables. First, the magnetic effects of the geometry of the cables are estimated and then the influence of the measured magnetization of the superconductors on the magnetic field quality measured at 1.9 K is evaluated.

In the first section the production, the geometry, the tolerances on dimensions, the tolerances on magnetization and the measurements of the two types of superconducting cables used in the LHC main dipole coils are presented.

The analysis performed on the influence of the cable dimensions on the dipole magnetic field quality is evaluated, in order

- To estimate the influence of the cable tolerances on field quality
- To verify the impact of the measured variations of dimensions in the cable production on the random components of the field harmonics
- To study the effect on field quality when the two coil layers, wound with cables of different manufacturer, are coupled in a same aperture
- To analyze the correlation between cable geometry and field quality.

Finally the effects on the magnetic field, measured at 1.9 K due to the persistent currents of the superconductor are studied. The aims of the work are the followings:

- To compare the measured difference of the magnetization among cable producers to the offset between measurements at injection field at 1.9 K and at room temperature
- To evaluate for each cable manufacturer the offset between injection field at 1.9 K and room temperature measurements; when no measurements on magnets are available, they are estimated using existing models and data on cable magnetization.
- To compute the offsets to be applied for the machine, using the final composition of cable manufacturers.

Cable Dimensions vs. magnetic field

4.1 Production

4.1.1 Cable types

The coil design of the LHC main dipole is based on a two layers cosϑ structure with current grading between the inner and the outer layer by using two different Rutherford superconducting cables. The inner layer cable (usually referred as ‘‘Cable01’’) is made of 28 NbTi strands of 1.065mm diameter; the outer layer cable (‘‘Cable02’’) is made of 36 NbTi strands of 0.825mm diameter. They both have a trapezoidal shape and the quantities that define the cable geometry are the mid-thickness (defined at 50 MPa), the keystone angle and the width, see Figure 4.1. The nominal dimensions and tolerances on these quantities for the two types used in the LHC main dipoles are given in Table 4.1 [4.1].

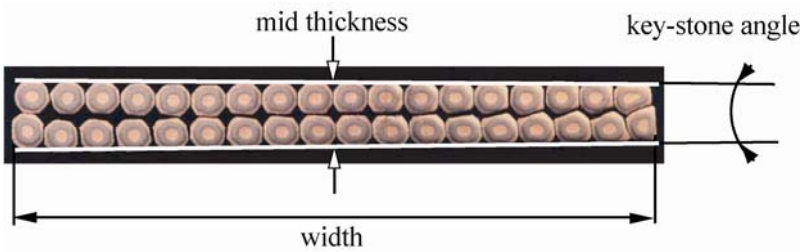

Figure 4.1: Main dimensions of a Rutherford cable.

Table 4.1: Nominal dimensions and tolerances of the two types of cables used in the LHC coils

	Cable 01	Cable 02
Width	$15.10^{+0.08}_{-0.00}$ mm	$15.10^{+0.08}_{-0.00}$ mm
Mid-thickness at 50 MPa	1.900±0.006 mm	1.480±0.006 mm
Keystone angle	1.25±0.05 deg	0.9±0.05 deg
N° of superconducting strands	28	36
Minimum unit length	448 m	740 m

4.1.2 Production and dimensional control

The cables are delivered at CERN in four unit lengths per pallet (a unit length is the length necessary to wind a single layer of one pole), and before being accepted they have to satisfy several control tests: magnetization, inter-strand cross contact resistance, copper to superconductor ratio, critical current (both on the strand and on the cable) and dimensional analysis. The whole amount of cable production required for the LHC construction is about 7000 km.

The production of Cable01 is shared among two firms whilst that one of Cable02 among five; we identify cable manufacturers by letters (B and E for Cable01 and B, C, D, G and K for Cable02). In Table 4.2 we show how the cable production is shared among the firms.

Each manufacturer performs systematic quality control on both strands and cables. Indeed, CERN has installed a dedicated test laboratory for measurements to cross-check the results from the industry. In particular CERN performs dimensional and physical tests on one cable unit length over four from each pallet delivered.

Table 4.2: Cable production shared among firms expressed in LHC octants.

	Cable manufacturers					
	B	C	D	E	G	K
Dipole Inner Layer (Cable01)	5	-	-	3	-	-
Dipole Outer Layer (Cable02)	3	2	1	-	1	1

4.1.3 Cable assembly procedures

In the LHC dipoles Specification [4.6] it is written: "The cables will be delivered in 4 unit lengths per pallet… the Contractor shall establish the manufacturing plan such that the 4 units length will be used in the same cold mass. Should one (or more) layer(s) be rejected during manufacture, CERN will choose one (ore more) unit length(s) of equivalent characteristics". In other words, in one cold mass the cables used to wind the 4 inner layers should come from the same supplier and the same for the outer layer cables. Indeed, in certain situations the cables can be mixed in order to easy the production but the replacement has to be guided by similarity in the dimensional and physical proprieties. During the collared coil production only in few cases the cold mass assembler had to mix the cables. In the analysis when we refer to a dipole cable configuration two letters are given (e.g. EK) which indicate the inner and outer cable producers respectively of the four poles.

4.2 Available data

4.2.1 Cable dimensions

The cable production was terminated in January 2006. More than 7000 km of superconducting cables were produced and delivered to CERN. As mentioned the cable to be accepted had to pass severe tests both in industry and at CERN. Regarding the dimensional control, it is found that the suppliers and CERN measurements are slightly different [4.7], for instance CERN cable width measurements have more spread than the ones taken in the supplier premises. In our analysis only CERN measurements on the mid-thickness, key stone angle and width will be taken into account. The statistic sample is reported in Table 4.3.

Table 4.3: Number of cable billet measured for dimensional control and magnetization measurements.

Cable manufacturer	Dimensional measurements
01B	1200
01E	1240
02B	730
02C	1000
02D	320
02G	360
02K	370

4.2.2 Collared coil measurements at room temperature

In Table 4.4 the number of the collared coils and dipoles measured at room temperature is given and split according to the cable configuration of the magnets. No mixed cable configuration in a single aperture along the production was found; this means that the cables of the upper and lower layers of the dipole apertures come always from the same supplier. Hence in the first column of Figure 4.4 the cable configuration used in the analyzed dipole is given only with the inner and outer cable supplier. By the way, in next section also the analysis performed at the beginning of the production to evaluate the effect of mixing cables of different suppliers in the same aperture is given.

The whole magnet production was measured at room temperature in order to have a fast feed back and a complete model of the machine. Here the used sample is about a thousand magnets (80% of the production) which all have the last modification of the cross section (see Chapter 2) thus having a large homogeneous sample to be analyzed. No magnets with the EK configuration have the last aperture cross section.

.

Table 4.4: Number of collared coils measured at room temperature.

Cable manufacturer	Measured Coll. coil. at room temp.
01B/02B	258
01B/02C	64
01B/02D	80
01B/02G	109
01B/02K	68
01E/02B	131
01E/02C	132
01E/02D	74
01E/02G	61
01E/02K	-
Total	977

4.3 Trends in cable geometrical data and in magnetic measurements at room temperature

4.3.1 Dimensional analysis

In Table 4.5 and in Figure 4.2 - Figure 4.4 we give the statistics of the measurements thickness, keystone angle and width. Two different standard deviations of the thickness and keystone angle measurements are evalauated. The "σ typical" is the spread of the measurements of one single cable billet (one cable is measured every two meters) while the "σ all" is the spread of the averages of the measurements of different cables of the same manufacturer. Only mean values and "σ all" are available for the width. The cable production is within tolerances and it is very homogeneous among the suppliers.

Table 4.5: Statistics of cable dimension measurements

Cable manufacturer	Mid thickness [mm]			Keystone angle [deg]			Width [mm]	
	μ	σ typical	σ all	μ	σ typical	σ all	μ	σ all
01B	1.8995	0.0017	0.0017	1.252	0.006	0.026	15.138	0.012
01E	1.9005	0.0016	0.0024	1.249	0.006	0.021	15.154	0.008
02B	1.4802	0.0015	0.0015	0.882	0.005	0.021	15.135	0.009
02C	1.4816	0.0020	0.0021	0.883	0.006	0.025	15.146	0.010
02D	1.4813	0.0016	0.0014	0.887	0.007	0.017	15.127	0.008
02G	1.4819	0.0016	0.0016	0.889	0.009	0.020	15.141	0.007
02K	1.4816	0.0014	0.0013	0.890	0.008	0.019	15.140	0.008

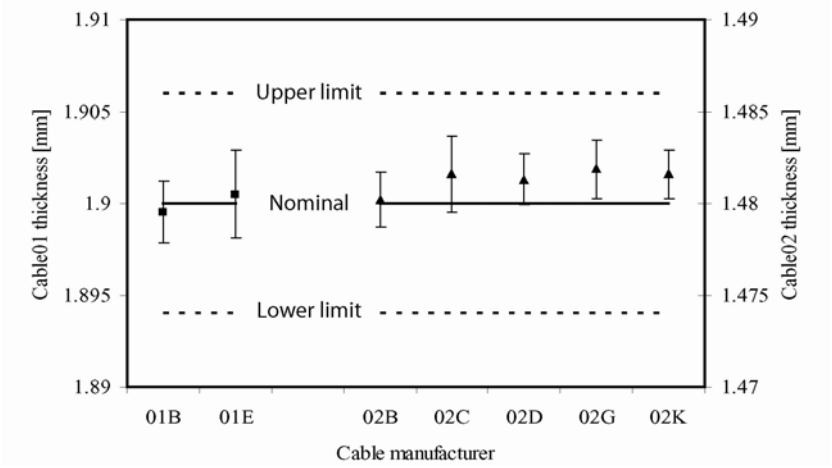

Figure 4.2: Cable mid thickness measurements versus tolerances. An error bar of one sigma is associated to the measurements.

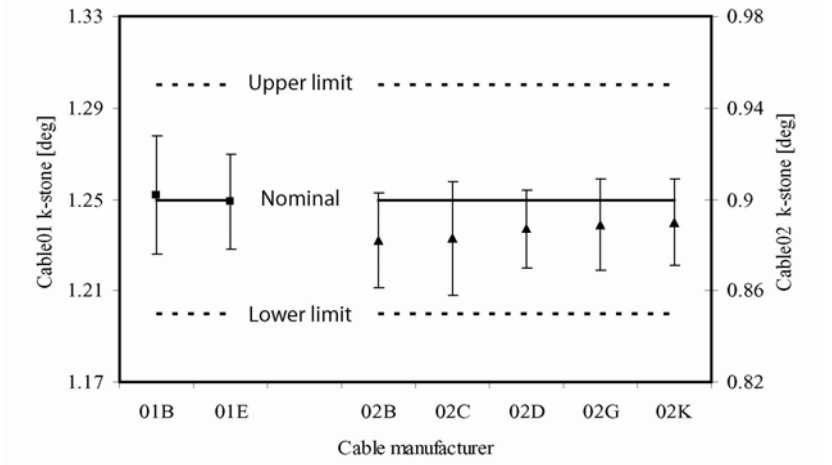

Figure 4.3: Cable key-stone angle measurements versus tolerances. An error bar of one sigma is associated to the measurements.

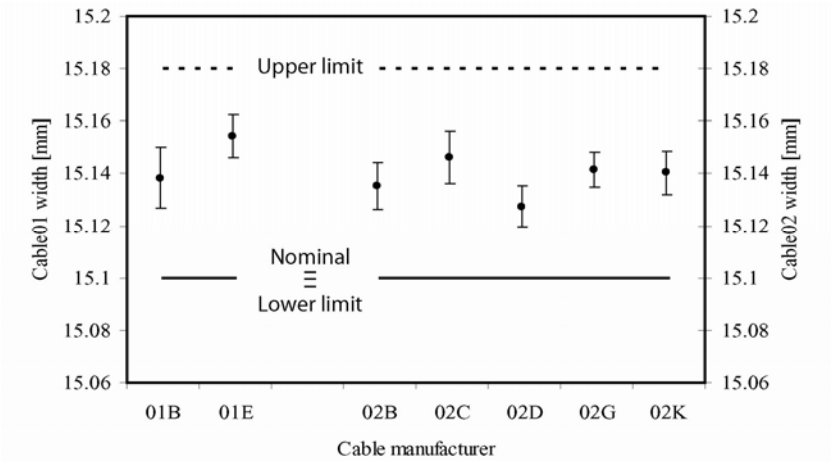

Figure 4.4: Cable width measurements versus tolerances. An error bar of one sigma is associated to the measurements.

4.3.2 Room temperature harmonics vs. cable manufacturer

A variation of the cable dimensions affects the odd normal and the even skew field harmonics. In Table 4.6 we give the average (μ) and the r.m.s (σ) of these classes of harmonics measured at room temperature relative to the cable configuration.

There is not correlation between the cable configuration and the field harmonics. A large variation of the averages when the same inner layer cable is taken into account shows that the geometry of Cable01 has not relevant influence on field quality. On the other hand, cable configurations which present the same Cable02 (for instance: compare BG and EG), present similar means and averages even if the difference are in the order of 30%. Concluding, the cable manufacturers have not a visible impact on the field quality at room temperature.

Table 4.6: Average (μ) and the r.m.s (σ) of these classes of harmonics with respect to the cable configuration of the collared coil.

	01B/02B		01B/02C		01B/02D		01B/02G		01B/02K	
	μ	σ	μ	σ	μ	σ	μ	σ	μ	σ
b_3	-1.87	1.74	-1.70	1.15	-2.29	0.84	-1.56	0.61	-3.06	1.22
b_5	0.184	0.519	-0.75	0.581	-0.76	0.271	-0.48	0.196	-0.62	0.435
b_7	1.179	0.161	0.991	0.109	1.046	0.125	1.198	0.048	0.86	0.242
a_2	0.32	1.07	0.29	1.06	0.59	1.03	0.76	0.89	0.33	1.03
a_4	0.056	0.318	0.231	0.311	0.052	0.279	-0.04	0.288	0.353	0.320
	01E/02B		01E/02C		01E/02D		01E/02G		01E/02K	
	μ	σ	μ	σ	μ	σ	μ	σ	μ	σ
b_3	-1.0_3	1.364	-2.18	0.974	-2.99	0.693	-1.33	1.147	-	-
b_5	0.144	0.557	-0.690	0.481	-0.740	0.130	-0.380	0.180	-	-
b_7	1.088	0.107	0.933	0.124	1.117	0.043	1.125	0.054	-	-
a_2	0.12	1.01	0.15	0.98	0.93	0.60	0.66	0.80	-	-
a_4	0.036	0.326	0.171	0.272	-0.09	0.241	-0.18	0.248	-	-

4.4 Expected field harmonics vs. measured at room temperature

4.4.1 Sensitivity matrix

Here, we evaluate how the tolerances of the cable thickness, keystone angle and width influence the field harmonics.

Effect on prestress

If the average mid-thickness of the cables is different from the nominal value, also the azimuthal length of the coil will be not nominal. In our study, we give to the cable the maximum allowed tolerance, i.e. +0.006 mm; multiplying it for the number of the cables contained in the considered layer (15 in the inner layer and 25 in the outer one) and assuming nominal copper wedges and shims, we can calculate the excess size of the azimuthal coil length of the inner and outer layers (both upper and lower pole): 0.18 mm and 0.30 mm respectively. This affects the prestress given to the coil: an additional thickness of 0.1 mm in the coil size gives an additional pre-stress of 12.5MPa [4.12]. Using the results of [4.13] relative to the influence of pre-stress on field harmonics, we evaluate the effect on the multipoles (Table 4.7).

Table 4.7: Effect of a collar deformation due to an azimuthal prestress of the coil (in [MPa]) at room temperature on odd multipoles (10−4 units, Rref = 17mm) for the collared coil.

[MPa]	Δb_3	Δb_5	Δb_7
0	0	0	0
10	-0.46	0.11	-0.02
20	-0.91	0.23	-0.04
30	-1.37	0.34	-0.05
40	-1.83	0.45	-0.07
50	-2.29	0.57	-0.09
60	-2.74	0.68	-0.11
70	-3.20	0.80	-0.12
80	-3.66	0.91	-0.14
90	-4.11	1.02	-0.16

Tilt of the mid-plane

The other effect due to the non nominalities of the cable thickness is a shift of the midplane, the shift being proportional to the difference of the non nominalities between the upper pole cable and the lower pole cable; this will affect the even skew harmonics because an up-down anti-symmetry is created. Using of the sensitivity tables given in [4.14] we evaluate the effects on these multipoles in the hypothesis that the elastic modulus of the cables is negligible with respect to the one of the copper wedges and the collar cavity.

Key-stone angle

A difference of the keystone angle between the upper layer cable and the lower one results in a tilt of the contact surface between the two poles. A change of the keystone angle does not influence the average prestress (since the mid-thickness

remains nominal) and therefore there is no impact on odd normal multipoles; it will affect only the even skew harmonics, see Table 4.8. The study was carried out with a magneto-static model assuming an infinitely rigid cavity and copper wedges.

Cable width

The non nominalities of the cable width give an effect on all the harmonics considered, actually a larger width produces an effect which is a combination of a up-down and left-right symmetry (odd normal multipoles excited) and a up-down anti-symmetry (even skew multipoles excited). Also in this case, we use the sensitivity matrix give in [4.14] in the hypothesis of infinite rigidity of the copper wedges and collars.

In Table 4.8 we summarize the influence of the cable geometrical tolerances on field harmonics. The effects of the tolerances are evaluated according to the worst case. For instance, the highest impact on odd normal multipoles is given by a cables mid-thickness of both layers (upper and lower) close to the upper limit of the tolerances (so that the pre-stress increases). On the other hand, the worst case for the even skew harmonics is obtained by a maximum shift of the mid plane, i.e. when the upper layer is larger than the nominal and the lower is smaller.

Table 4.8: Sensitivity of cable geometrical tolerances on magnetic field harmonics.

Geometric Parameter		Mid Thickness		Keystone angle	Width	
Induced effect		Pre-stress change of the coil	Shift of the mid plane	Tilt of the contact surface between layers	Narrower coil	Wider coil
Worst case	Upper pole	+0.006 mm each cable	+0.006 mm each cable	0.05 deg each cable	-0.02 mm each cable	0.02 mm each cable
	Lower pole	+0.006 mm each cable	-0.006 mm each cable	-0.05 deg each cable	0 mm each cable	0 mm each cable
Inner layer	b_3	-0.5	0	0	0.11	-0.11
	b_5	0.13	0	0	-0.004	0.004
	b_7	-0.020	0	0	0.004	-0.004
	a_2	0	4.8	-2.0	0.72	-0.73
	a_4	0	0.72	-0.23	0.10	-0.10
Outer layer	b_3	-0.8	0	0	-0.12	-0.19
	b_5	0.21	0	0	0.03	0.00
	b_7	-0.034	0	0	-0.005	-0.004
	a_2	0	4.7	-1.8	1.1	-1.6
	a_4	0	0.34	-0.23	0.31	-0.19

The impact of cable dimensions on odd normal multipoles is rather small when compared to the allowed range for the systematics given by the beam dynamics (see Table 4.9). In particular is negligible for b_3 and b_7 (at most 0.6 units and 0.025 units respectively). The only concern is for b_5 that could be shifted of up to 0.35 units in the case of cables systematically at the edge of the mid-thickness tolerance: this is half of the allowed range for the systematic (see Table 4.8). Cable widths within tolerances have a much lower impact on odd multipoles than mid-thickness.

The influence of cable dimensions on even skew multipoles can be relevant. If all upper cables are systematically larger than lower cables, but within tolerances, one

can obtain both a_2 and a_4 that are out of the allowed ranges for systematics (Table 4.9). In this unfortunate case, one could obtain up to 9.5 units of a_2 and 1 unit of a_4, i. e. values much larger than the allowed range (2 and 0.26 units respectively). In order to evaluate the impact of these tolerances on random components, we perform a Monte Carlo analysis which will be described in the next section.

Table 4.9: Targets for field harmonics in terms of allowed range for the systematic and maximal allowed spread [4.15].

Field harmonics	Range for systematic	Random (one sigma)
b_3	4.5	1.7
b_5	0.8	0.5
b_7	0.5	0.2
a_2	2	1.9
a_4	0.3	0.6

4.4.2 Expected harmonics: evaluation and comparison with the measured ones

The used algorithm is the following: we use the "σ all", see Table 4.5, and the mean (μ) in order to build a Gaussian distribution for each manufacturer. Then, we randomly extract one value of the distribution. This will be the average parameter over the unit length. Now using the "σ typical" and the extracted average we simulate the variation of the parameter along the cable length by building another Gaussian distribution. From this last Gaussian we extract 15 or 25 numbers (i.e., the number of cables in the inner and outer layer, respectively) to build the upper pole. We repeat the same for the lower pole and we obtain the geometry of the entire aperture and using the sensitivity tables we can evaluate the effects on field harmonics. We do the same study for all the possible configurations of firms coupling in one aperture (avoiding the permutations), this means three cases for the inner layer (BB, BE, EE, where the first letter correspond to the cables manufacturer of the layer of the upper pole) and 10 cases for the outer layers (BB, BC, BG, BK, CC, CG, CK, GG, GK, KK). For each scenario we compute the effect on field harmonics iterating 10^6 times the described algorithm. A similar study is carried out using the measurement of the cable width. Since for the cable width no values for "σ typical" are available, we use for the two Gaussian distributions the values of "σ all".

The analysis is split in first evaluating the effects on multipoles caused by coupling in the same aperture two cables of a same manufacturer and then two cables from different producers. Each aperture randomly generated by the Monte Carlo simulation identifies one dipole. This assumption hides the conservative hypothesis that the coherence length (the maximum length along which the cable dimensions can be considered as constant) of the dipole is the total length. If the coherence length is shorter than the dipole length the results of the simulation will be rescaled of a factor of $\sqrt{N}$ where N is the number of coherence lengths in a dipole.

Impact on random components: cable of same manufacturer

We analyze the case of layers of upper and lower poles wound with cables from same manufacturer, which is the LHC baseline. We find that the influence of the cable

thickness variation on random a_2 is up to 1.40 units (one sigma) compared to 1.9 units specified for the collared coil (Table 4.10). Assuming that the influences of the inner and outer layer are independent, i.e. summing they in quadrature, one obtains 1.7 units that is closed to the specified value. Therefore the simulation shows that the mid-thickness accounts for most of the specified a_2 (Table 4.9). On the other hand, a negligible effect of cable dimension is found on the random components of odd normal field harmonics. These results are not surprising since the sensitivity matrix shows that the impact of the cable geometry on odd normal multipole is rather small.

Table 4.10: Random multipoles (one sigma) expected from the measured spread in *mid-thickness* with respect to the cable manufacturers of the two poles.

	Upper pole cable	Lower pole Cable	b_3	b_5	b_7	a_2	a_4
Inner Layer	B	B	0.10	0.03	0.004	0.99	0.15
	E	E	0.15	0.04	0.006	1.40	0.21
Outer Layer	B	B	0.15	0.04	0.006	0.86	0.06
	C	C	0.20	0.05	0.009	1.20	0.09
	D	D	0.14	0.04	0.006	0.80	0.06
	G	G	0.16	0.04	0.007	0.91	0.07
	K	K	0.13	0.03	0.005	0.74	0.05

Table 4.11: Random multipoles (one sigma) expected from the measured spread in *keystone angle* with respect to the cable manufacturers of the two poles.

	Upper pole Cable	Lower pole cable	a_2	a_4
Inner Layer	B	B	0.75	0.09
	E	E	0.60	0.07
Outer Layer	B	B	0.53	0.07
	C	C	0.63	0.08
	D	D	0.43	0.05
	G	G	0.50	0.07
	K	K	0.48	0.06

Table 4.12: Random multipoles (one sigma) expected from the measured spread in *width* with respect to the cable manufacturers of the two poles.

	Upper pole cable	Lower pole cable	b_3	b_5	b_7	a_2	a_4
Inner Layer	B	B	0.05	0.00	0.002	0.32	0.04
	E	E	0.03	0.00	0.001	0.22	0.03
Outer Layer	B	B	0.06	0.00	0.001	0.53	0.06
	C	C	0.07	0.00	0.001	0.59	0.07
	D	D	0.06	0.00	0.001	0.47	0.06
	G	G	0.05	0.00	0.001	0.41	0.05
	K	K	0.06	0.00	0.001	0.47	0.06

Considering the three random components induced by the three measured dimensions (tables above) we reconstruct the global effect on a_2 and a_4 and in Table 4.13 and we compare them with the measured ones from Table 4.6. We find that the simulated random part of a_4 well describe the measurements (within a 30 % in the worst case) whilst the expected values of a_2 are about 40-50% larger than the measured. We can say that the driving mechanism of a_2 and a_4 can the cable

dimensions; the effect induced on a_2 is partially reduced during the assembly procedure.

Table 4.13: Measured and expected random part of even skew harmonics

cable configuration	measured		expected	
	a_2	a_4	a_2	a_4
BB	1.07	0.32	1.72	0.24
BC	1.06	0.31	1.96	0.24
BD	1.03	0.28	1.64	0.21
BG	0.89	0.29	1.70	0.22
BK	1.03	0.32	1.63	0.24
EB	1.01	0.33	1.92	0.25
EC	0.98	0.27	2.13	0.26
ED	0.60	0.24	1.85	0.24
EG	0.80	0.25	1.90	0.25
EK	-	-	1.84	0.24

Impact on field quality: cables of different manufactures

At the beginning of the dipole production there was the need to quantify the effect on field quality of a replacement of one cable with one not belonging to the same manufacturer. Even though the baseline was to replace damaged cables with the same manufacturer, this scenario had to be analyzed to check if this alternative option was viable to ease production and logistics in special cases.

Using the same method discussed in the previous section, we simulate the effect on field quality of coupling cables of different manufacturers in the same aperture. Results are given in Table 4.14 - Table 4.16 where we list both the standard deviation and the average for the effects due to the thickness, keystone angle and width. The geometrical parameter which has the largest impact on field quality is the mid-thickness; on the other hand, the influences of the non-nominalities of the width are negligible.

No effect on odd normal field harmonics and a large effect on the even skews are found: if some combinations of manufacturers for the upper and lower pole (BE for inner layer and BC for the outer) would be systematically met during production, this would give rise to systematic even skew multipoles out of specifications. Indeed, the effect on a single or on a few magnets would not affect the systematic over the entire machine and would not spoil the random component.

Moreover the width effects on the field quality are completely negligible with respect to Table 4.9. We can conclude that it is not mandatory, from a geometrical point of view, to replace a cable damaged during assembly with another one of the same manufacturer.

Table 4.14: Impact on the systematic and random harmonics components of coupling cables due to the non nominalities of the *mid thickness*.

	Upper cable	Lower cable		b_3	b_5	b_7	a_2	a_4
Inner Layer	B	E	σ	0.13	0.03	0.005	1.18	0.18
			μ	-0.03	0.01	-0.001	0.39	0.06
Outer Layer	B	C	σ	0.19	0.05	0.007	1.01	0.07
			μ	-0.09	0.02	-0.003	0.55	0.04
	B	G	σ	0.16	0.04	0.006	0.88	0.07
			μ	-0.09	0.03	-0.003	0.66	0.05
	B	K	σ	0.16	0.04	0.006	0.85	0.06
			μ	-0.06	0.02	-0.003	0.55	0.04
	B	D	σ	0.16	0.04	0.006	0.86	0.06
			μ	-0.05	0.01	-0.002	0.43	0.03
	C	D	σ	0.18	0.05	0.008	1.01	0.07
			μ	-0.07	0.02	-0.003	0.12	0.01
	C	G	σ	0.19	0.05	0.007	1.07	0.08
			μ	-0.06	0.01	-0.002	0.12	0.01
	C	K	σ	0.19	0.05	0.008	1.06	0.08
			μ	0.00	0.00	0.000	0.00	0.00
	D	G	σ	0.16	0.04	0.007	0.88	0.07
			μ	-0.13	0.03	-0.005	0.24	0.02
	D	K	σ	0.15	0.04	0.006	0.80	0.06
			μ	-0.07	0.02	-0.003	0.12	0.01
	G	K	σ	0.16	0.03	0.007	0.87	0.07
			μ	-0.16	0.04	-0.006	0.12	0.01

Table 4.15: Impact on the systematic and random harmonics components of coupling cables due to the non nominalities of the *keystone angle*.

	Upper cable	Lower cable		a_2	a_4
Inner Layer	B	E	σ	0.68	0.08
			μ	-0.06	-0.01
Outer Layer	B	C	σ	0.58	0.07
			μ	-0.02	0.00
	B	G	σ	0.52	0.06
			μ	-0.12	-0.02
	B	K	σ	0.50	0.06
			μ	-0.14	-0.02
	B	D	σ	0.48	0.06
			μ	-0.09	-0.02
	C	D	σ	0.52	0.06
			μ	-0.07	-0.01
	C	G	σ	0.56	0.07
			μ	0.12	0.02
	C	K	σ	0.55	0.07
			μ	0.11	0.00
	D	G	σ	0.47	0.06
			μ	-0.04	-0.01
	D	K	σ	0.45	0.06
			μ	-0.05	-0.01
	G	K	σ	0.48	0.06
			μ	-0.02	0.00

Table 4.16: Impact on the systematic and random harmonics components of coupling cables due to the non nominalities of the *keystone angle*.

	Upper cable	Lower cable		b_3	b_5	b_7	a_2	a_4
Inner Layer	B	E	σ	0.13	0.03	0.005	1.18	0.18
			μ	-0.03	0.01	-0.001	0.39	0.06
Outer Layer	B	C	σ	0.19	0.05	0.007	1.01	0.07
			μ	-0.09	0.02	-0.003	0.55	0.04
	B	G	σ	0.16	0.04	0.006	0.88	0.07
			μ	-0.09	0.03	-0.003	0.66	0.05
	B	K	σ	0.16	0.04	0.006	0.85	0.06
			μ	-0.06	0.02	-0.003	0.55	0.04
	B	D	σ	0.16	0.04	0.006	0.86	0.06
			μ	-0.05	0.01	-0.002	0.43	0.03
	C	D	σ	0.18	0.05	0.008	1.01	0.07
			μ	-0.07	0.02	-0.003	0.12	0.01
	C	G	σ	0.19	0.05	0.007	1.07	0.08
			μ	-0.06	0.01	-0.002	0.12	0.01
	C	K	σ	0.19	0.05	0.008	1.06	0.08
			μ	0.00	0.00	0.000	0.00	0.00
	D	G	σ	0.16	0.04	0.007	0.88	0.07
			μ	-0.13	0.03	-0.005	0.24	0.02
	D	K	σ	0.15	0.04	0.006	0.80	0.06
			μ	-0.07	0.02	-0.003	0.12	0.01
	G	K	σ	0.16	0.03	0.007	0.87	0.07
			μ	-0.16	0.04	-0.006	0.12	0.01

Cable magnetization vs. magnetic field

4.5 Magnetization measurement and quality control

When the dipoles are excited at low current – 760 A (corresponding to a magnetic field of 0.54 T) - the magnetic field quality is affected by the persistent currents created in the superconducting filaments [4.2]. The persistent currents are strictly related to the concept of "magnetization of a superconductor": when a superconductor is immersed in magnetic field, it generates persistent currents (which do not decay due to the lack of resistivity of the material) to create a magnetic field opposite to the external one; the self-made field is the magnetization of the superconductor. In order to predict the field errors during injection field, magnetization measurements are performed on the superconducting strands at 1.9 K, i.e. the LHC operational temperature. The limits imposed at the beginning of the cable production on the strand magnetization are given in Table 4.17 [4.3]. Then the limits for the averages were relaxed during the production whilst the ones for the variation remained unchanged. Moreover the strict limits on strand magnetization measurement is given by the tolerance imposed to the variation along the averages (±4.5%): the cable magnetization is the average of the magnetizations of the 28 or 36 strands composing the cable and then by sorting the strands composing a cable the spread of the cable magnetization is reduced of a factor $1/\sqrt{28}$ (or $1/\sqrt{36}$) with respect to the one of the strands [4.5].

Table 4.17: Limits and tolerances imposed on LHC cable magnetization curve width at 0.5T and 1.9K at the *beginning of the production*.

	Average of the production	Tolerance with respect to the average
Cable01 – Inner Layer	<30mT	±4.5%
Cable02 – Outer Layer	<23mT	±4.5%

4.6 Available Data

4.6.1 Magnetization measurement and quality control

The number of magnetization measurements is considerably high (Table 4.3) because all unit lengths were measured. The strand magnetization is measured using two pick up coils connected in series plunged in an external time dependent magnetic field at 1.9 K. A sample is put in one of the two pick up coils. The external magnetic field is ramped up to 1T. The two pick up coils collect a time dependent flux that generates a voltage, according to the electromagnetic induction law. The pick up coil that contains the sample sees a magnetic flux that is the sum of the flux of the external field and the flux due to the magnetic field generated by the superconductor, whereas the empty pick up coil sees only the flux due to the external magnetic field. The sum of the flux seen by the two pick up coils, being inversely connected, is directly

proportional to the magnetization of the superconductor. The external field is ramped from 0 T to 1 T and then down to 0 T, thus obtaining a magnetization curve as shown in Figure 4.5. The width of the curve at 0.5 T is measured. In order to avoid time dependent effects various measurements at different ramp rates of the field are performed and the extrapolated value at a ramp rate equal to zero is taken [4.8].

Table 4.18: Number of cable billet measured for dimensional control and magnetization measurements.

Cable manufacturer	Magnetization measurements
01B	3400
01E	2600
02B	2700
02C	2000
02D	800
02G	1000
02K	900

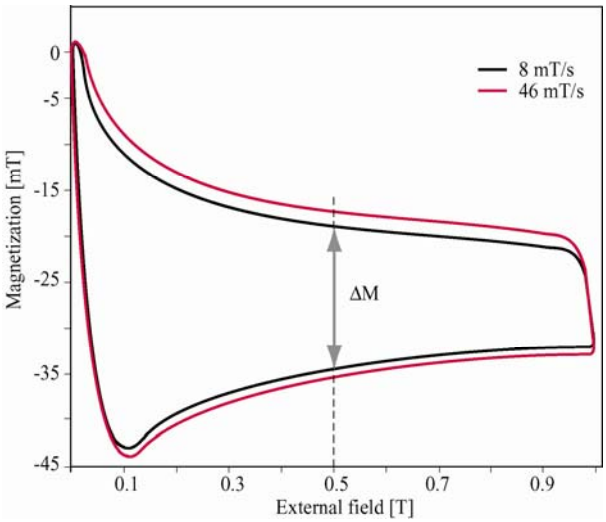

Figure 4.5: Strand magnetization curves measured at two different external magnetic field ramp rates, and amplitude ΔM of the hysteresis at 0.5 T.

4.6.2 Magnetic field measurements at 1.9 K

In Table 4.19 the number of dipoles measured at 1.9 K is given and split according to the cable configuration of the magnets. As it was decided in [4.9], only about 20% of the dipoles has been measured at 1.9 K; most of them present BB and BK cable configurations.

Several types of measurements are performed at 1.9 K [4.10], in this analysis the interest is focused on those which are correlated to the magnetization of the superconducting cables, namely the measurements performed at low excitation current, when the field quality is mainly affected by persistent current. The magnetic field quality measurements at 1.9 K are performed following a so-called "loadline curve" (see Chapter 3). In Figure 4.6 we give as example the b_1 and b_3 measurements along the loadline.

Table 4.19: Number of dipoles measured at 1.9 K

Cable manufacturer	Dipoles meas. at 1.9 K
01B/02B	60
01B/02C	9
01B/02D	3
01B/02G	11
01B/02K	58
01E/02B	13
01E/02C	12
01E/02D	17
01E/02G	3
01E/02K	10
Total	196

We denote the measurements performed at injection field of 0.54 T (excitation current of 760 A, ramping up of the current) by b_n^{inj}. The geometric component is denoted by b_n^{geo}, and it is defined as the average of the two values of the ramp-up and ramp-down branches at 5000A. The *persistent current component of the field errors* is then computed as $b_n^{pers} = b_n^{inj} - b_n^{geo}$; this value is strictly linked to the magnetization of the cables. Moreover since the cable magnetization is evaluated as a width of the magnetization hysteresis loop at 0.5 T, we also evaluate also the *width of the field error loops* at 760A as shown in Figure 4.6 left. For the main component of the field, we define b_1, for the straight part of the magnets, as:

$$b_1 = \frac{TF_{meas} - TF_{nom}}{TF_{nom}} 10^4 \quad ; \text{TF is the "transfer function"}: \frac{\text{Magnetic field [T]}}{\text{Energizing current [kA]}} ,$$

the value of TF_{nom} is 0.707 T/kA at injection field, see Figure 4.6 for the hysteresis curve on b_1.

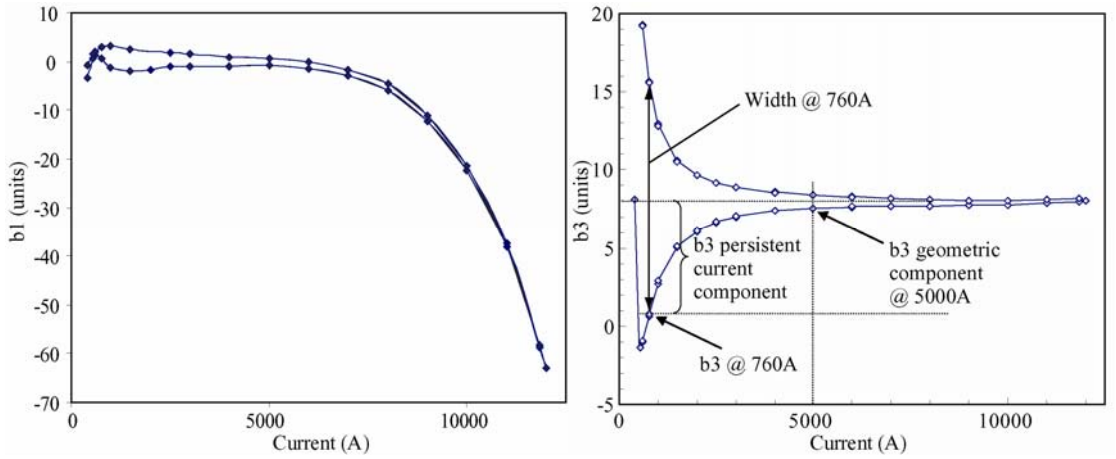

Figure 4.6: b_1 and b_3 measured along the loadline, width of the hysteresis at injection field (760 A), and geometric component at 5000 A (average of ramping up and down).

4.7 Trends in cable magnetization data and magnetic measurement at 1.9 K.

4.7.1 Cable magnetization

The results of the analysis of the magnetization measurements are given in Table 4.20 and in Figure 4.7 and Figure 4.8:

- For the Cable01: the average magnetization of 01E is 13% higher than 01B. This difference is due the different type of productions adopted by the two manufacturers: single stack by supplier B and double stack by E (see section 2). Standard deviations are below 3% (1 sigma), and the spreads are inside the allowed band of tolerance of ±4.5%.
- For the Cable02: 02B, 02G and 02K have a very similar average magnetization (within 2%), 02C has 3.6% more, and 02D has 4% less. Standard deviations are below 2.5% (1 sigma)

Table 4.20: Average and rms of the magnetization measurements of the six cable productions.

Manufacturer	μ [mT]	σ [mT]
01B	27.1	0.55
01E	30.7	0.55
02B	22.0	0.36
02C	22.5	0.34
02D	21.0	0.22
02G	21.7	0.33
02K	22.0	0.27

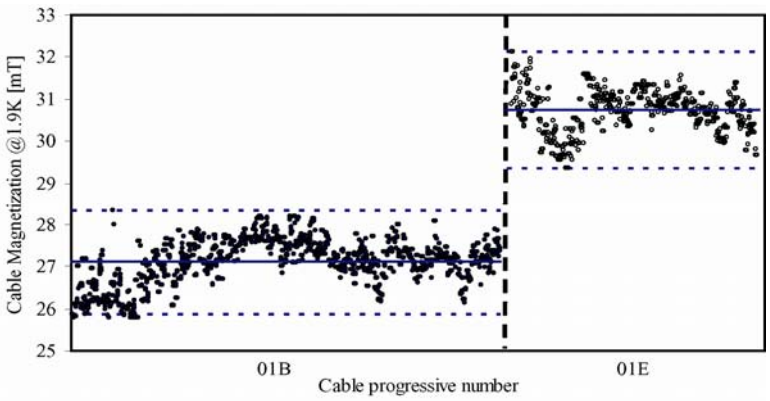

Figure 4.7: Cable01 magnetization measurement at performed CERN and control limits.

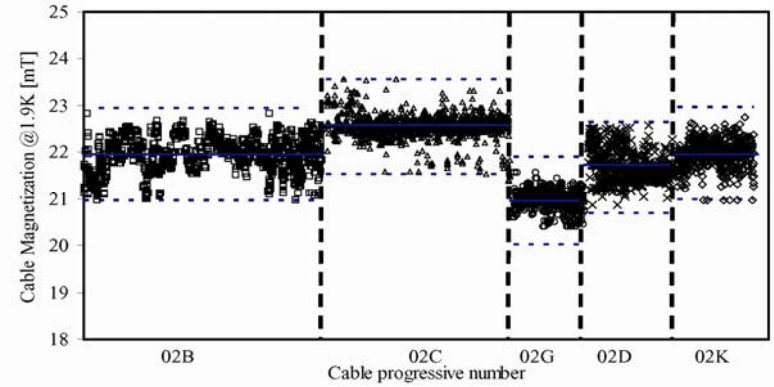

Figure 4.8: Cable02 magnetization measurement at performed CERN and control limits.

4.7.2 1.9 K harmonics vs. cable manufacturers

Persistent current field harmonics components

In Figure 4.9 the persistent current components b_3, b_5, b_7 and b_9 measured in about 200 dipoles are plotted. Data are sorted according to the cable manufacturer. In Table 4.21, data relative to the four plots and results of the analysis on b_1 are presented: for each cable configuration we evaluate the average and the r.m.s..

Negligible differences have been found between magnets with inner cable 01E and the others with 01B; the largest ones are for high order multipoles between the configuration 01B/02K and 01E/02K giving a difference of about 10% for b_5, b_7 and b_9.

Table 4.21: Average and standard deviation of the persistent current multipole components in the LHC main dipoles measured at 1.9 K and sorted by their cable configuration.

	01B/02B		01B/02C		01B/02D		01B/02G		01B/02K	
	μ	σ	μ	σ	μ	σ	μ	σ	μ	σ
b_1	-1.26	1.44	-2.80	0.98	-0.21	0.52	0.84	0.94	-0.23	1.35
b_3	-7.18	0.34	-7.58	0.27	-6.90	0.16	-7.11	0.20	-6.91	0.28
b_5	1.12	0.11	1.09	0.08	0.98	0.05	1.04	0.06	1.03	0.06
b_7	-0.31	0.03	-0.34	0.04	-0.31	0.03	-0.28	0.02	-0.30	0.03
b_9	0.20	0.02	0.19	0.01	0.19	0.02	0.18	0.01	0.19	0.01
	01E/02B		01E/02C		01E/02D		01E/02G		01E/02K	
	μ	σ	μ	σ	μ	σ	μ	σ	μ	σ
b_1	-0.90	1.41	-1.66	0.79	0.80	0.85	0.44	0.41	-0.30	1.21
b_3	-6.86	0.35	-7.01	0.36	-6.90	0.32	-7.06	0.06	-6.69	0.31
b_5	1.04	0.11	1.02	0.09	1.05	0.06	0.97	0.09	1.19	0.07
b_7	-0.33	0.04	-0.31	0.04	-0.33	0.04	-0.33	0.01	-0.40	0.04
b_9	0.19	0.02	0.20	0.02	0.19	0.01	0.19	0.00	0.21	0.02

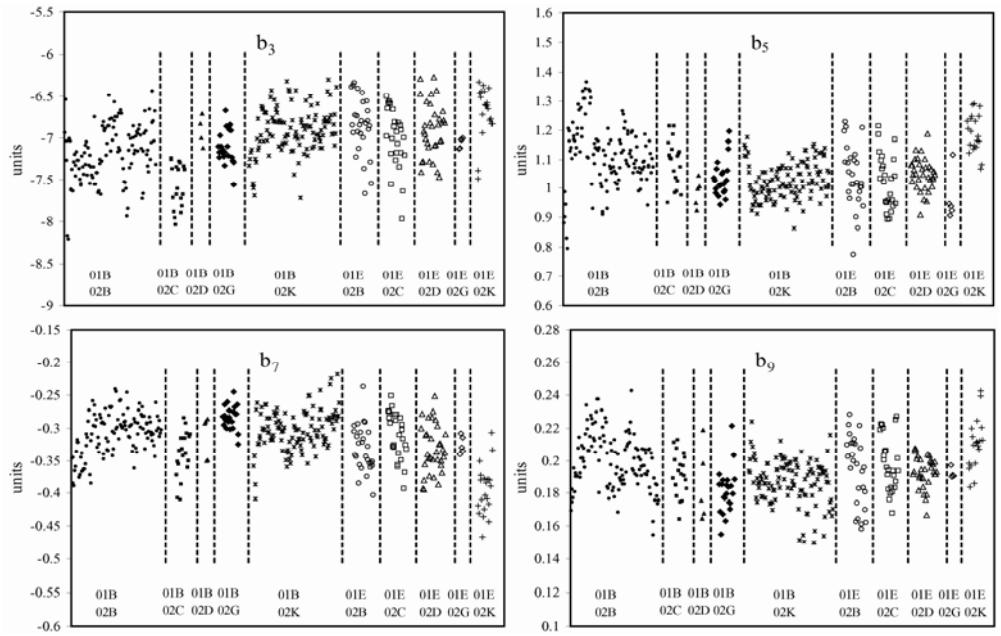

Figure 4.9: Persistent current components of the LHC dipoles sorted by cable manufacturer.

Hysteresis loop width at 760 A

In Figure 4.10 we plot the widths of the hysteresis curves of the field harmonics at 760A, sorted by cable configuration. In this case, 01E and 01B have a similar behavior for b_3, and show differences in b_5, b_7 and b_9. Here, the difference in b_5 and b_9 is 25% (compared to 10% observed for the lower branch only), whereas for b_7 we have 30% as in the previous case. The average main field hysteresis width is 4.5 units lower for the cables 01E with respect to the ones of 01B, see Table 4.22.

The difference between the high order multipoles ($n \geq 5$) of the configuration with inner cable 01E and the others is evident, about 20%. A large difference in b_1 (about 50%) is found between magnets with cable 01B and 01E. A correlation of the values of the b_3 for the configuration 01B/02C and 01E/02C is found: both present the lowest values. Actually the influences of the persistent current on b_3 are dominated by the outer layer cable magnetization [4.11].

Table 4.22: Average and standard deviation of the hysteresis loop multipole width at 760A in the LHC main dipoles measured at 1.9 K and sorted by their cable configuration

	01B/02B		01B/02C		01B/02D		01B/02G		01B/02K	
	μ	σ	μ	σ	μ	σ	μ	σ	μ	σ
b_1	-9.97	2.14	-12.42	1.56	-9.20	0.57	-8.62	2.13	-9.33	3.01
b_3	-14.95	0.44	-15.88	0.48	-14.53	0.12	-15.01	0.32	-14.75	0.30
b_5	1.90	0.12	1.77	0.07	1.81	0.05	1.91	0.07	1.79	0.06
b_7	-0.70	0.04	-0.75	0.04	-0.74	0.03	-0.72	0.03	-0.70	0.04
b_9	0.40	0.02	0.39	0.01	0.39	0.02	0.40	0.01	0.39	0.01
	01E/02B		01E/02C		01E/02D		01E/02G		01E/02K	
	μ	σ	μ	σ	μ	σ	μ	σ	μ	σ
b_1	-5.16	0.78	-6.20	1.27	-4.09	0.51	-4.66	0.41	-4.03	1.89
b_3	-14.57	0.20	-15.38	0.37	-14.50	0.17	-14.44	0.25	-14.57	0.27
b_5	2.14	0.08	2.08	0.11	2.16	0.06	2.13	0.05	2.29	0.12
b_7	-0.81	0.03	-0.80	0.03	-0.81	0.02	-0.80	0.02	-0.92	0.06
b_9	0.44	0.02	0.44	0.02	0.43	0.01	0.42	0.01	0.44	0.03

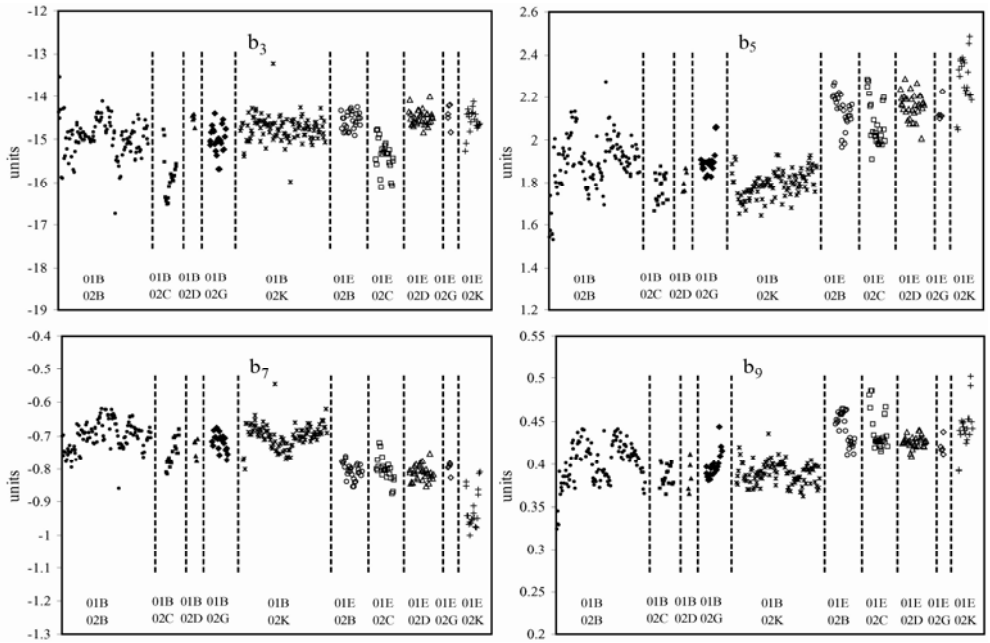

Figure 4.10: Width of the hysteresis loops of the field errors at 760A and 1.9K.

4.8 Expected field harmonics vs. measured at 1.9 K

4.8.1 Calculated magnetization and field quality at injection

We used an existing model that computes persistent current component from the measured cable magnetizations. Several models have been developed in the past. Here, we use the approach developed in [4.15] which allows the calculation of superconductor induced field errors combined with iron induced errors for determining the results for a complete magnet cross-section during ramp. The input of the persistent current model is a fit function for the critical current density j_c that can be obtained from the magnetization measurement on the strand. The model is included in a code [4.17] and is used to calculate geometrically identical magnet cross-sections, feeding the respective current fit functions for the different cable combinations.

The individual strand magnetization depends on the locally applied field and thus on the position within a coil cross-section. Also the applied ramp cycle has to be considered for the calculation of the hysteresis of the strand magnetization. The main feature of this model with respect to previous works is that the impact of the persistent current field on the source field in the coil has been taken into account by an inner iteration cycle since the original local field configuration undergoes a small perturbation when the persistent current field is superposed.

For the calculations, the following ramp cycle is applied, i.e. starting from 0 T, going to 8.4 T, then to 0.25 T (the pre-cycle) and back to the injection field level at 0.54 T. We used a fit function for Nb-Ti [4.18] that has been adjusted for the different cables by modifying the fit parameters accordingly. Figure 4.11 shows the agreement of the measured field errors at 1.9 K with the calculations for a magnet with the cable combination 01B/02K.

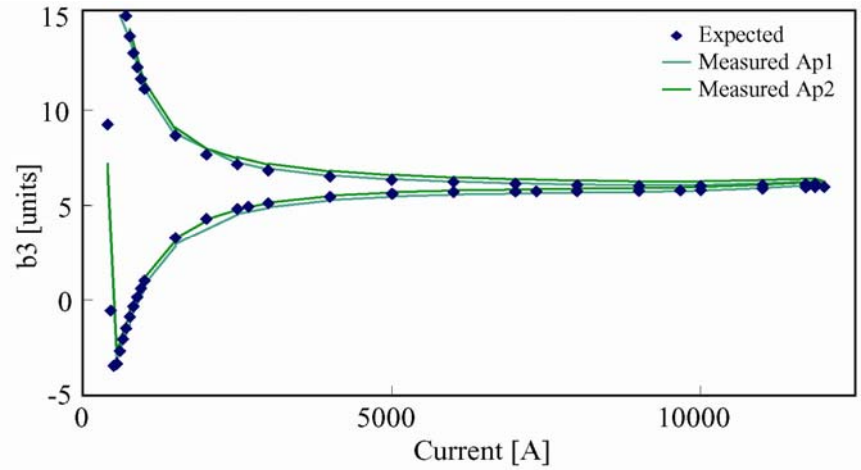

Figure 4.11: Measured b_3 versus excitation current of the two apertures of a magnet (solid lines) and calculated results based on magnetization measurements (dots).

As can be seen, there is a very good agreement between the calculated field errors and the measurement (both apertures are shown). It has to be mentioned, that there can be some small deviations observed on the geometric value measured at cold between different magnets or between the two apertures of the same magnet. Most likely, this

is caused by a small difference in the exact conductor placement between different magnets or by a small difference in the calibration of the pick-up coils for the measurement. In these cases, the calculated and measured values can be brought in agreement by a small adjustment of the vertical shift.

This method allows the calculation of *persistent current induced field errors* and the resulting *hysteresis width* for different cables during a ramp cycle as well as the calculation of a specific magnet equipped with a certain cable combination for which the calculation can be compared with measurements taken at 1.9 K. Expected persistent current field errors and widths of the field error hysteresis loop at injection field level (B=0.54 T or 760 A) at 1.9 K due to cable magnetization are evaluated for all the 10 possible LHC cable combinations (both Cable01 producers can be coupled with each of the 5 Cable02 manufacturers) and the results are given in Table 4.23 and Table 4.24.

The configurations in which the inner layer cable 01E is used present values of persistent current multipoles (with n>5) and widths of the hysteresis loops larger than about 15% with respect to the averages of the respective values of the other configurations. This result was expected since the cable 01E presents a higher magnetization as mentioned in the previous section. For n=1 and 3 this consideration is not valid since the larger effect is given by the outer layer cable. If we compare, see Figure 6, the measured and the expected values we find that all the expected harmonics are within two standard deviations of the measured harmonics except b_1. The simulations and the measurements of the hysteresis loop width of b_1 for the configuration in which the inner cable 01E is used have a difference of 50%, this is due to the deformed shape of the hysteresis loop which has been found in the measurement of such dipoles.

Table 4.23: Calculated *persistent current field errors* at injection (B=0.54T; I=760A) versus cable manufacturer (in units of 10-4 at 17mm).

	01B 02B	01B 02C	01B 02D	01B 02G	01B 02K	01E 02B	01E 02C	01E 02D	01E 02G	01E 02K
b_1	17.57	17.28	17.85	17.99	17.57	17.99	17.57	18.41	17.99	17.57
b_3	-6.85	-6.99	-6.77	-6.73	-6.87	-7.28	-7.42	-7.20	-7.16	-7.29
b_5	0.91	0.93	0.91	0.90	0.92	1.05	1.06	1.04	1.04	1.05
b_7	-0.31	-0.31	-0.31	-0.31	-0.31	-0.36	-0.36	-0.36	-0.36	-0.36
b_9	0.18	0.18	0.18	0.18	0.18	0.20	0.20	0.20	0.20	0.20

Table 4.24: Calculated *widths of error hysteresis loop* at injection (B=0.54T; I=760A) versus cable manufacturer (units of 10-4 at 17mm).

	01B 02B	01B 02C	01B 02D	01B 02G	01B 02K	01E 02B	01E 02C	01E 02D	01E 02G	01E 02K
b_1	10.74	11.45	10.18	9.90	10.74	9.90	10.74	9.05	9.90	10.74
b_3	14.74	15.05	14.54	14.45	14.77	15.56	15.87	15.36	15.26	15.58
b_5	-1.59	-1.61	-1.58	-1.58	-1.59	-1.86	-1.88	-1.85	-1.85	-1.86
b_7	0.64	0.63	0.64	0.65	0.64	0.74	0.73	0.74	0.74	0.74
b_9	-0.35	-0.35	-0.35	-0.35	-0.35	-0.39	-0.39	-0.39	-0.39	-0.39

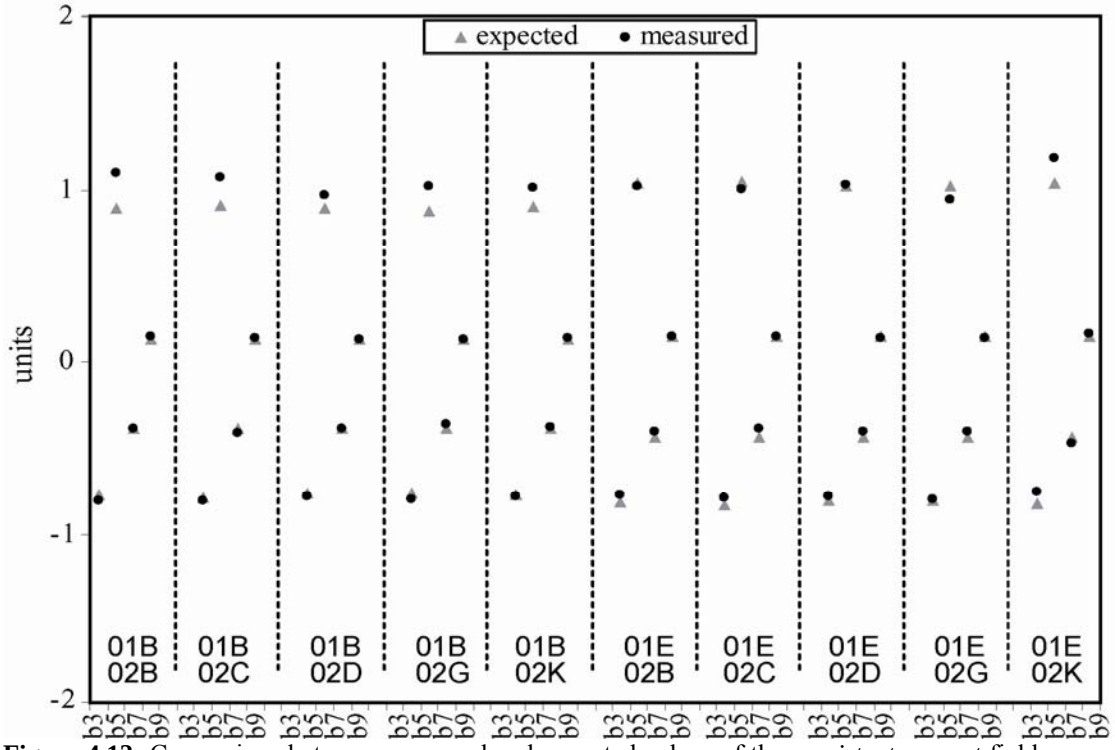

Figure 4.12: Comparison between measured and expected values of the *persistent current* field errors. Due to graphic reasons $b_3/10$ is plotted.

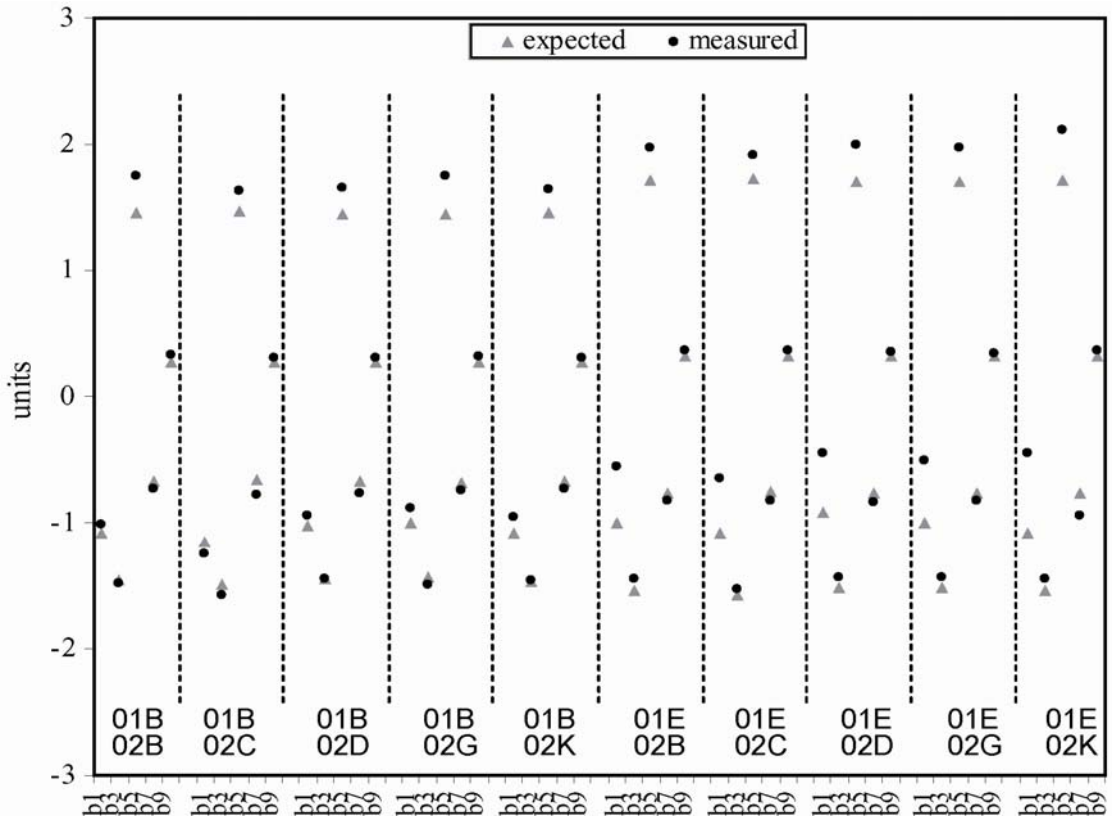

Figure 4.13: Comparison between measured and expected values of the *widths of error hysteresis loop*. Due to graphic reasons $b_1/10$ and $b_3/10$ are plotted.

Finally, we compute the ratio between the contribution of the outer layer and of the inner layer, following [4.4]. Data are given in Table 4.25: for multipoles order $n \geq 5$, the field errors are mainly generated by the inner cable; for lower order the outer layer is important and, in particular, the largest contribution to the sextupole comes from the outer layer cable.

Table 4.25: Ratio between outer and inner layer contribution to persistent current field error generation.

Relative outer layer persistent current effect: $b_{n\ outerlayer}/b_{n\ inner\ layer}$				
b_1	b_3	b_5	b_7	b_9
-1.85	2.17	-0.14	-0.1	-0.02

4.8.2 Dependence of the beam dynamics target at room temperature on the cable magnetization

As discussed in chapter 3, the limits imposed to the field quality are given by the beam dynamics constraints in operational conditions (1.9 K), both at injection field level and at high field. The target ranges for the systematic (i.e., the average multipole over the entire machine) are given in Table 4.26. The geometric component b_n^{geo} at 1.9 K reflects the geometry of the coil at room temperature plus the effect of the cool-down. At injection the field, the harmonics result from the geometric component at 1.9 K plus the persistent current effects (b_n^{pers}); multipoles at high field are mainly the sum of the effects given by the geometric component plus the iron saturation of the surrounding yoke and the deformation caused by the Lorentz forces ($b_n^{iron\_lf}$).

Table 4.26: Field harmonics bounds given by the beam dynamics at injection and high field level (0.54 T and B=8.33 T respectively).

		Lower limit	Upper limit
b_3	Injection	-10.50	10.50
	High field	-3.00	3.00
b_5	Injection	-1.10	1.10
	High field	-0.80	0.80
b_7	Injection	-0.30	0.10
	High field	-	-

We recall from chapter 3 that the limits given at 1.9 K are steered to room temperature measurement by:

$$b_{n\_lower\_limit}^{cm} = \max(b_{n\_lower\,limit}^{inj} - b_n^{off,inj}; b_{n\_lower\,limit}^{high} - b_n^{off,high}) - b_n^{BS} \quad \text{Eq. 4.1}$$

$$b_{n\_upper\_limit}^{cm} = \min(b_{n\_upper\,limit}^{inj} - b_n^{off,inj}; b_{n\_upper\,limit}^{high} - b_n^{off,high}) - b_n^{BS} \quad \text{Eq. 4.2}$$

Normally [10] it was assumed that the offset $b_n^{off,inj}$ is independent of the cable configuration used in the apertures. In the previous section, we showed that there is a sensible difference in magnetization among cables manufacturers and a consequent difference of the persistent current field harmonics measured in dipoles with different

cable combinations. This means that for each cable combination $\overline{b_n^{pers}}$ is different, therefore giving rise to $b_n^{off,\ inj}$ and, hence, different limits have to be applied to the room temperature measurements.

In the followings, we first compute the limits to be applied at room temperature for each combination cable manufacturer. We use averages over magnets measured both at room temperature and at 1.9 K with the same combination of cable manufacturer. Then, we compute the limits for the whole production by weighting the limit of each cable manufacturer with the amount of production foreseen by the baseline. In this section b_1 is not taken in to account since we have no target on the systematic.

Dependence of targets at room temperature on combination of cable manufacturers

In Table 4.27 - Table 4.29 we give the target ranges for b_3, b_5 and b_7 on cold mass measurements at room temperature. Estimates based either on magnetic measurements (when available) or on magnetization measurements and models are carried out independently for each combination of cable manufacturer. One can point out the following features:

- For b_3, the upper limit is always determined by the high field constraint (see Figure 4.14 left – Table 4.27) and therefore it does not depend on cable manufacturer. The lower limit varies up to 0.17 units, compared to the size of the target range of 6 units. Therefore the effect can be considered as negligible.
- For b_5, the lower limit is determined by the high field limit (Figure 4.14 - central) and therefore it does not depend on cable manufacturer. The upper limit varies up to 0.22 units, that is not negligible compared to the size of the target range (0.6 units).
- For b_7, both lower and upper limits are given at injection (there is no target at high field, Figure 4.14 - right), and therefore they depend on the cable manufacturer. Both limits can move up to 0.12 units, and also in this case it is not negligible compared to the size of the target range.

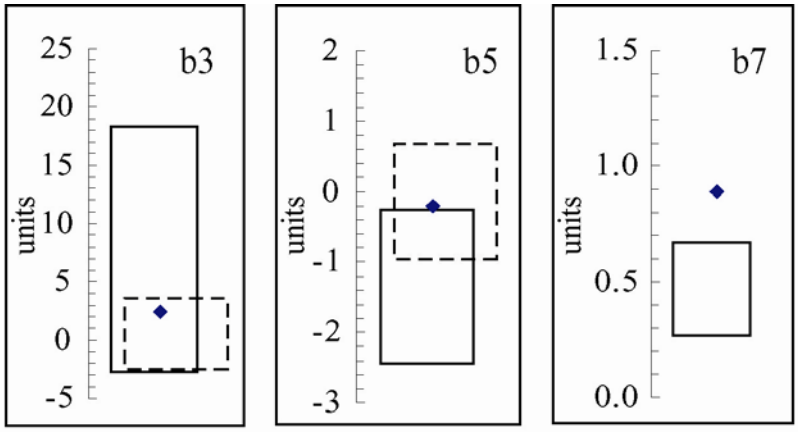

Figure 4.14: Target ranges for systematic at room temperature: inj. field constraints (solid lines) and high field constraints (dotted lines), and present measured values in the production (dots).

Table 4.27: b_3 target ranges on room temperature measurements of cold masses computed on the average of the measured magnets, and separately on each combination of cable manufacturer.

	Lower limit	Upper limit
Limits computed on the average over *all measured magnets*	-2.40	3.60
Limits computed on the average over *single cable combination*	Lower limit	Upper limit
01B/02B	-2.40	3.60
01B/02C	-2.23	3.60
01B/02D	-2.40	3.60
01B/02G	-2.40	3.60
01B/02K	-2.40	3.60
01E/02B	-2.40	3.60
01E/02C	-2.40	3.60
01E/02D	-2.40	3.60
01E/02G	-2.40	3.60
01E/02K	-2.40	3.60
Max Difference among limits	0.17	0

Table 4.28: b_5 target ranges on room temperature measurements of cold masses computed on the average of the measured magnets, and separately on each combination of cable manufacturer.

	Lower limit	Upper limit
Limits computed on the average over *all measured magnets*	-0.94	0.25
Limits computed on the average over *single cable combination*	Lower limit	Upper limit
01B/02B	-0.94	-0.27
01B/02C	-0.94	-0.24
01B/02D	-0.94	-0.13
01B/02G	-0.94	-0.19
01B/02K	-0.94	-0.18
01E/02B	-0.94	-0.19
01E/02C	-0.94	-0.17
01E/02D	-0.94	-0.20
01E/02G	-0.94	-0.12
01E/02K	-0.94	-0.34
Max Difference among limits	0	0.22

Table 4.29: b_7 target ranges on room temperature measurements of cold masses computed on the average of the measured magnets, and separately on each combination of cable manufacturer.

	Lower limit	Upper limit
Limits computed on the average over *all measured magnets*	0.27	0.67
Limits computed on the average over *single cable combination*	Lower limit	Upper limit
01B/02B	0.25	0.65
01B/02C	0.28	0.68
01B/02D	0.25	0.65
01B/02G	0.22	0.62
01B/02K	0.24	0.64
01E/02B	0.27	0.67
01E/02C	0.25	0.65
01E/02D	0.27	0.67
01E/02G	0.27	0.67
01E/02K	0.34	0.74
Max Difference among limits	0.12	0.12

Target ranges for the whole machine weighting different cable manufacturer

We finally evaluate the target ranges for the systematic by taking into account of the final composition of the machine in terms of cable manufacturers. The ranges computed in the previous table are averaged using a weighted sum (each weight represents the fraction of the cable combination with respect to the total production, Table 4.2):

$$b_n^{\text{off,inj}} = \sum_{K=1}^{10} w_K \cdot b_{nK}^{\text{off,inj}} = \left(\sum_{K=1}^{10} w_K \cdot \overline{b_{nK}^{\text{pers}}} \right) + \overline{b_n^{\text{off,geo}}} \qquad \text{Eq. 4.3}$$

Where K=1,…10 are the possible cable combinations.

The results are presented in Table 4.30. Comparing the weighted limits to the old ones, obtained with a simple average over the measured magnets, we see a negligible difference. We conclude that the target ranges used up to now for the steering for the production are not affected by a statistical bias due to a sampling of cable manufacturer that does not reflect the final composition of the machine.

Table 4.30: Tolerance limits imposed to cold mass room temperature magnetic measurements (here on b_5 and b_7): they are evaluated weighting the effect of persistent field harmonics with respect to the sharing of the cable production.

	Lower limit		Upper limit	
	Simple average	Weighted average	Simple average	Weighted average
b_5	-0.94	-0.94	-0.25	-0.26
b_7	0.27	0.26	0.67	0.66

4.9 Conclusion

In this chapter we analysed how the dimensional tolerances associated to the cable geometry and their magnetization influence the magnetic field harmonics.

The *geometrical dimensions* of the LHC main dipole cable have been analysed:

- The measurements show that the tolerances imposed to the production are satisfied by all cable suppliers.
- The effects on the even skew could be relevant if the cables of the upper poles are systematically larger than the lower cables (or vice versa), whilst the impact of the geometrical tolerances on odd normal harmonics is rather small.
- Using a distribution of cable dimensions based on the measured values, we simulated with a Monte Carlo method the impact on field quality through the sensitivity matrix. A negligible effect on random components with respect to both measurements and to targets, with the exception of the cable thickness on a_2 has been found.
- Results show that tolerances on cable thickness can account for most of the measured and specified a2 (and a4), whereas a negligible effect is found on the other multipoles.

- The effect on field quality of coupling cables of different manufacturers in the same aperture is simulated: on odd normal multipoles is negligible and on the even skew multipoles can be large: if some combinations of manufacturers for the upper and lower pole would be systematically met during production, this would give rise to a systematic even skew multipoles out of specifications. On the other hand: we find that it is not mandatory to replace a damaged cable with another cable of the same firm and single cases can be tolerated.
- We have compared the expected harmonics (evaluated from the cable geometry through the sensitivity matrix) with the collared coils field measurements. No correlation is found.

The *magnetization measurements* of the LHC main dipole cable and the effect on the tolerances of the field quality have been analysed:

- The average values of the magnetization of the two inner layer cable manufacturers differ of about 15%. On the other hand, the average magnetizations of the manufacturers of the outer layer cable are within 5%. The spread of the magnetization is within the tight target of 4.5%.
- We analysed the dependence of the measured persistent current field errors at injection on the cable manufacturers. For high order multipoles (b_5 and b_7) there is a difference that can be traced back to the difference in magnetization between inner cable manufacturers.
- For b_3 no dependence on the cable magnetization is found
- A magnetic model of the coil has been used estimate the measurements of persistent current contribution and hysteresis loop width, finding a good agreement.
- The dependence of the target range imposed by beam dynamics projected at room temperature on the cable manufacturer has been taken into account. The difference in the persistent current (and also in cable magnetization) induces slightly different ranges at room temperature. The target ranges compared by weighting the cable manufacturer according to the final composition of the machine are very close to the range computed by taking a simple average over all magnets measured at 1.9 K.

References

[4.1] D. Leroy "*Review of the R&D and Supply of the LHC Superconducting Cables*" **LHC-Project-Report-901**

[4.2] B. Bellesia et al., "*Trends in Cable Magnetization and Persistent Currents during the Production of the Main Dipoles of the Large Hadron Collider*", IEEE Trans. Appl. Supercond. **Vol. 15** (**2005**) 1213-16.

[4.3] *"LHC technical specification for the supply of 1158 cold masses of the superconducting dipole magnets for the LHC collider"*, ***Chap. 6,***, LHC Project Document **LHC–MB A–C1–0006**.

[4.4] R. Wolf "Effect of superconductor filament magnetization on the field errors" **CERN-OPEN-2000-159**

[4.5] Rob Wolf, CERN, Accelerator Techonlogy Department, Private Communication

[4.6] *"LHC technical specification for the supply of 1158 cold masses of the superconducting dipole magnets for the LHC collider"*, ***Annex C1,***, LHC Project Document **LHC–MB A–C1–0006**.

[4.7] L. Oberli, "*Follow up and checkpoints of cable properties*", Workshop on field quality, March 2003,http://lhc-div-mms.web.cern.ch/lhc-div-mms/MMSPAGES/MA/fqwrkshp/fqwrkshp.html

[4.8] Le Naour, S; Wolf, R; Billan, J; Genest, J, "*Test Station for Magnetization Measurements on Large Quantities of Superconducting Strands*" CERN- **LHC Project Report 451**

[4.9] L. Bottura et al "*A Strategy for Sampling the Field Quality of the LHC Dipoles*" **LHC-Project-Report-737**.

[4.10] S. Filippo et al., "*Magnetic measurements for 15 m long dipoles – standard program of cold test* " LHC **MTA-IN-2001-169**

[4.11] R. Wolf, S. Le Naour "*The Expected Persistent Current Field Errors in the LHC Main Dipole and Quadrupole*" **LHC-Prpject Note 230**; Geneva, CERN, 2000

[4.12] P. Ferracin, "*Mechanical and magnetical analysis of the large hadron collider main dipole*", PhD Thesis, **CERN-Thesis, 2002-009**.

[4.13] P. Ferracin, "*Azimuthal coil size and field quality in the main CERN Large Hadron Collider dipoles*", **Phys. Rev. Spec. Top. Accel. Beams 5** (2002).

[4.14] S. Pauletta, "*Field quality analysis to monitor the industrial series production of the dipole magnets for the large hadron collider*", Master Thesis, **CERN-Thesis-2003-024**.

[4.15] C. Vollinger, "*Superconductor Magnetization Modeling for the Numerical Calculation of Field Errors in Accelerator Magnets*", PhD Thesis, **CERN-Thesis - 2003-022**.

[4.16] M. Aleksa, et al, "*A Vector Hysteresis Model for Superconducting Filament Magnetization in Accelerator Magnets*", IEEE Trans. Magn.: **Vol. 40** (**2004**) no. 2 pt.2, pp.864-7.

[4.17] S. Russenschuck, M. Aleksa, M. Bazan, J. Lucas, C. Vollinger, "*Integrated Design of Superconducting Magnets with the CERN Field Computation Program ROXIE*", **CERN-LHC-Project-Report-446**

[4.18] L. Bottura, "*A Practical Fit for the Critical Surface of NbTi*", IEEE Trans. Appl. Supercond.: **Vol 10** (**2000**) no. 1, pp.1054-7

Chapter 5

Copper wedges

In this chapter the attention is focused on the four copper wedges that separate the superconducting blocks of the LHC main dipole coil to achieve the field quality required by the beam dynamics constraints. This analysis was started at the very beginning of the dipoles series-production during the second half of the 2002 [5.1], when about 60 over the 90 scheduled dipoles of the pre-series where completed. The aim was to analyze if the produced copper wedges had an influence on the field quality of the magnets and consequently to foresee the expected effects on the on coming series.

In this chapter we first present the study performed in 2002, and then the whole production is analyzed to check the total effect of the whole copper wedge production on LHC main dipole field quality. A dimensional analysis is performed on the whole production.

First, general information about the copper wedges is presented, the most relevant dimensions of these components are defined and sensitivity matrices on the field harmonics are computed. Then, a dimensional control of the 16 produced batches is presented. Then, the effect of the non nominalities on the odd multipolar components of the dipole field are computed and compared to the results of the magnetic measurements. In order to evaluate the impact of copper wedge dimensions on the final performances of the machine and to explain specific patterns observed in the field shape of the collared coils we performed a Monte-Carlo analysis. Results are compared to the allowed ranges for systematic components imposed by beam dynamics, and to the measured spread of multipoles observed in the production.

5.1 Production

5.1.1 Copper wedges profiles

Each aperture of the main LHC dipole contains by four different profiles of copper wedges as sketched in the ¼ of aperture shown in Figure 5.1. There are three wedges in the inner layer (profiles I-II-III) and one in the outer (profile IV) [5.2]. All wedges are produced by the same manufacturer, Outokumpu – Finland.

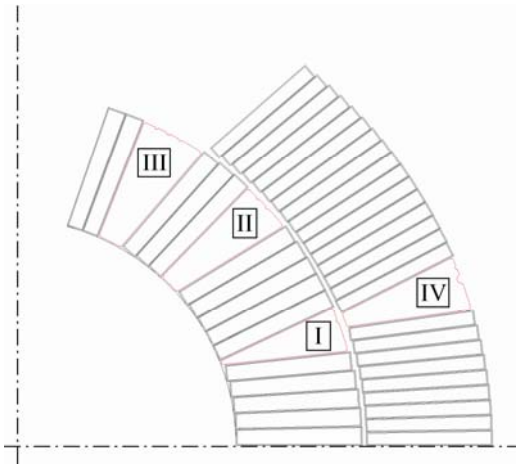

Figure 5.1: Coil cross section of the LHC main dipole: one quarter of the aperture in sketched. The four copper wedges profiles are indicated with Roman numbers.

Each profile is delivered in batche; one batch containing the amount of pieces necessary for assembling of ten dipoles plus one piece for destructive tests. One dipole cold mass contains approximately 114 meters of copper wedges of each profile. The wedges are delivered in 3.6 m long pieces. Consequently, in one dipole cold mass there are 32 copper wedge pieces of each profile. Hence each batch contains 321 pieces [5.3]. The batches are delivered by the supplier directly to the Cold Mass Assemblers. It must be pointed out that two "special" batches used in the early stage of the production that are not relative to 10 magnets: the *batch A* which was used for the production of the first three collared coils (one per Cold Mass Assembler) and the batch PROT, used in the assembly of the first six dipole prototypes, manufactured by BuntMetall (Germany).

In July 2001 a modification of the design of dipole cross section has been adopted in order to improve the field quality in the magnet aperture. The inner layer of the coil was changed by modifying the copper wedge profiles I, II and III while the outer layer was not changed [5.4]. The first batch for each profile done with the new geometry is the number 14. Another adjustment of the cross-section geometry occurred in the 2003 but the wedges profiles were not modified.

5.1.2 Production and dimensional analysis

In order to monitor the production, a certificate of conformity and dimensional control is associated to each batch. The document contains physical and chemical tests (tensile strength, elongation, hardness, chemical composition, electrical conductivity) and dimensional checks. Three pieces per batch are measured: the first produced, the last produced, and one intermediate. The dimensions quoted in the certificate of conformity are shown in Figure 5.2.

There are four lengths (a-b-d-e) and one angle (c), all being referred to the two surfaces A and B. In Table 5.1 the five nominal dimensions of the four profiles are listed. For each of the profiles I, II and III the design relative to both the first and the second-third cross section are reported.

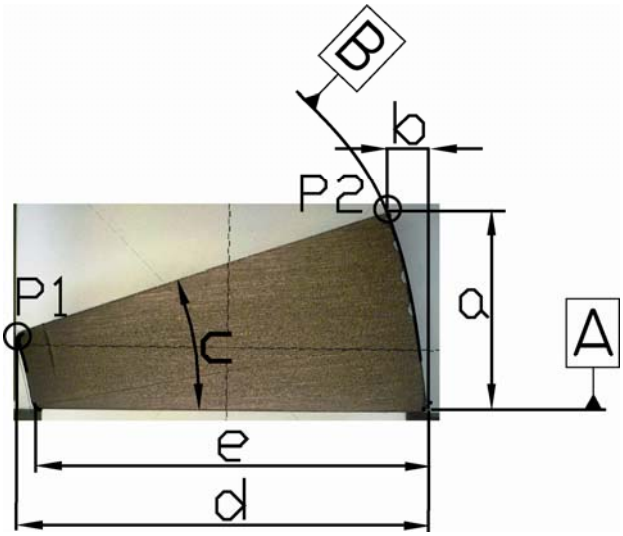

Figure 5.2: Dimensions quoted in the certificate of conformity (a-b-c-d-e) measured with respect to the two surfaces A and B. P1 and P2 are the quantities adopted for the dimensional control.

Table 5.1: Nominal dimensions of the five dimensions quoted in the certificate of conformity. The two designs are presented. Note that the profile IV was not changed [5.2].

		a [mm]	b [mm]	c [deg]	d [mm]	e [mm]
Profile I	Cross section 1	5.41	1.26	19.21	15.54	15.42
	Cross section 2-3	5.06	1.16	17.86	15.54	15.42
Profile II	Cross section 1	6.91	1.55	17.70	15.93	15.33
	Cross section 2-3	6.16	1.22	14.15	15.87	15.28
Profile III	Cross section 1	7.41	1.36	16.77	15.83	15.21
	Cross section 2-3	7.79	1.70	18.97	15.99	15.28
Profile IV	Cross section 1-2-3	6.64	1.38	18.94	15.71	15.32

The position of the surface which is created linking the left and right upper corner (P1 and P2 in Figure 5.2 is the crucial parameter for the magnetic field quality. In our analysis, we assume that the sides of the copper wedges are straight lines. According to the specification [5.3] can be drown that the surface containing P1 and P2 must stay in a band of tolerance of ±0.03 mm around the nominal position. Using the available data a-b-c-d-e, the variation ΔP1 and ΔP2 with respect to the nominal shape are computed for each batch. As mentioned in the beginning, the dimensional control is performed on the whole production.

The results are plotted in Figure 5.3 - Figure 5.6. The dashed lines are the dimensional tolerances of ±0.03 mm. The plotted points are the average values of the shift of P1 and P2 from the nominal position in each batch, whilst the error bars give the maximum and the minimum among the three pieces measured per batch.

The control protocols show batches of components within tolerances with some isolated exceptions, especially in the beginning of the production. Indeed we find that for profile II, III and IV, batch PROT and batch A are rather different from the successive production and they are out of tolerance. The batches of profile I are all inside tolerances with a fluctuation of ±0.02 mm.

Profiles I, II and III showed an upward trend in the beginning of the production, when the first study was performed, and in particular the profiles II and III reached pick values around batches 23-28. As a consequence a carefully monitoring of these

quantities was required, and the production was then periodically adjusted trougth a fine tuning of the tools.

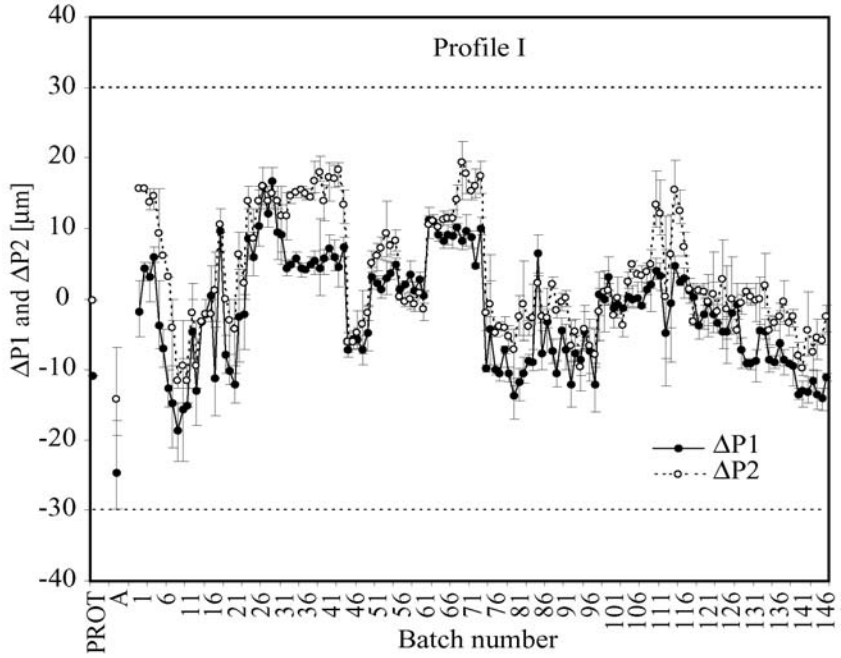

Figure 5.3: Profile I, copper wedge measurements: ΔP1 and ΔP2 - average among the three measured pieces per batch – maximum and minimum – errors bars – and tolerances (dotted lines).

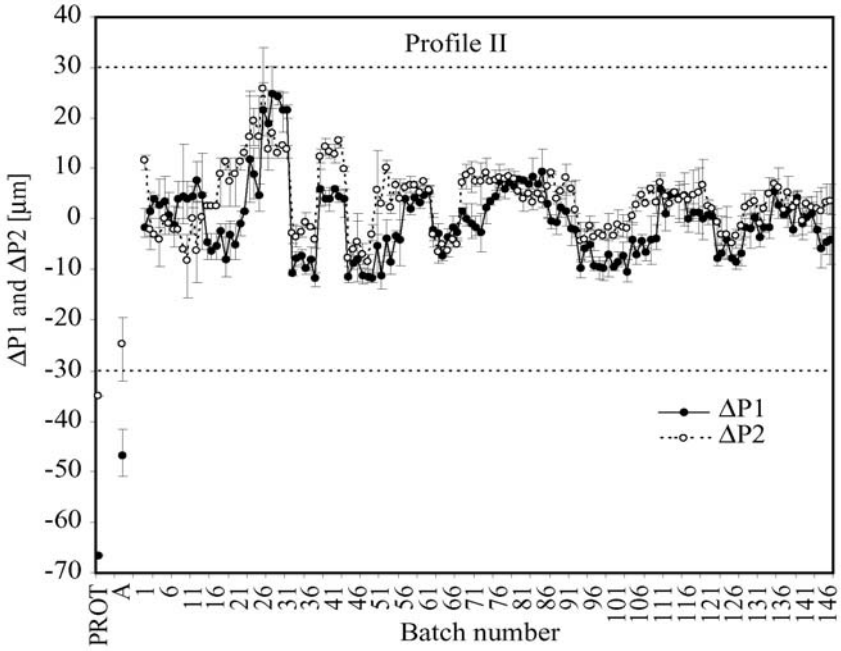

Figure 5.4: Profile II, copper wedge measurements: ΔP1 and ΔP2 - average among the three measured pieces per batch – maximum and minimum – errors bars – and tolerances (dotted lines).

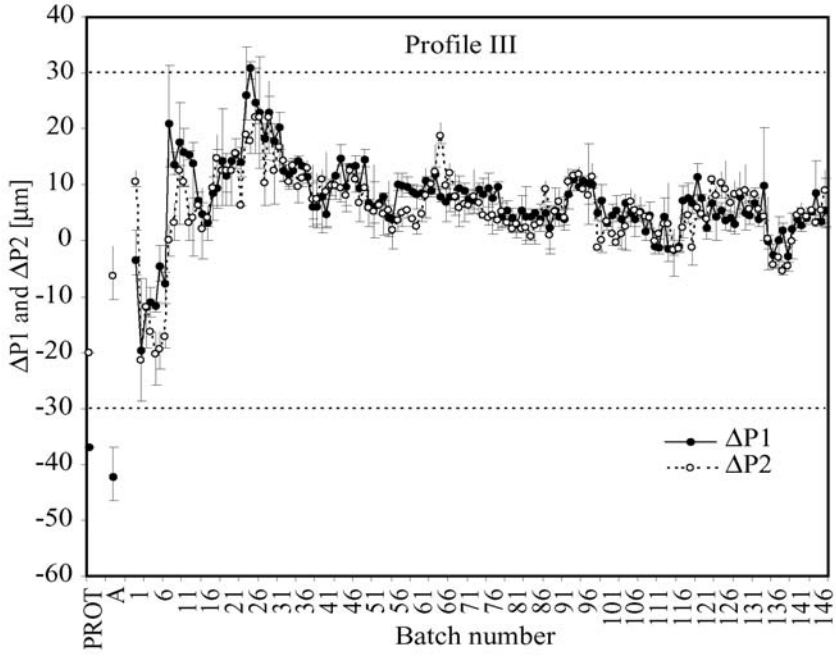

Figure 5.5: Profile III, copper wedge measurements: ΔP1 and ΔP2 - average among the three measured pieces per batch – maximum and minimum – errors bars – and tolerances (dotted lines).

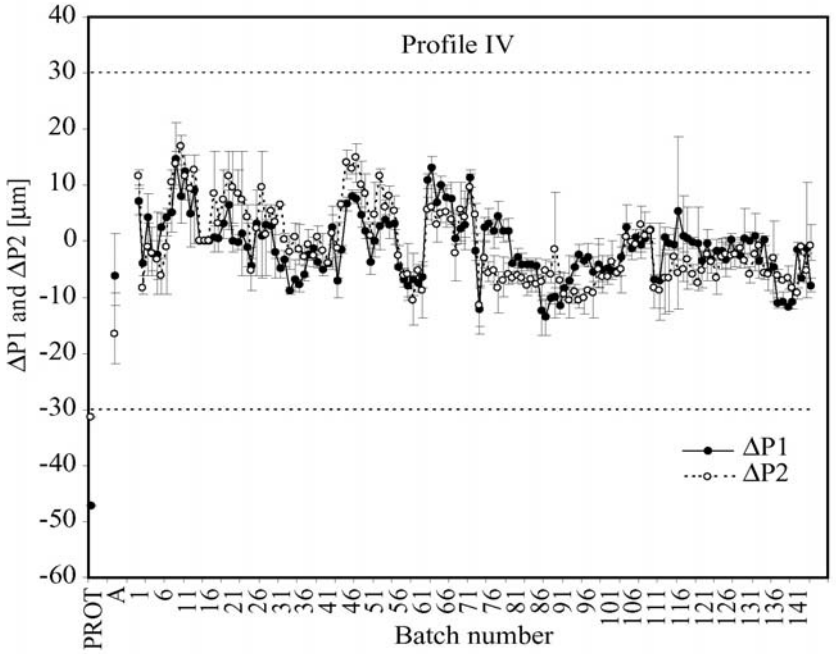

Figure 5.6: Profile IV, copper wedge measurements: ΔP1 and ΔP2 - average among the three measured pieces per batch – maximum and minimum – errors bars – and tolerances (dotted lines).

5.2 Available Data

The copper wedge production was terminated in December 2005. 146 batches of each profile were delivered to the three cold mass assemblers. In this chapter we will analyze the evolution of the field quality along the first 45 magnet produced (15 per cold mass assembler) in order to find if field imperfections were determined by wedges non nominalities. In Table 5.2 the ID of the magnets and the batch numbers of

the copper wedges used to assemble them are reported. The first test batch A and the batch 1 were used in the three firms then the batches were assigned entirely to a single firm. From batch 14 the design of the wedges profile I, II and III were changed for the new cross section design. In the sample given the first collared coils with the new cross section are the 1013 and 1014 for firm 1, the 2011 for firm 2 and the 3012 for firm 3.

Table 5.2: Collared coil ID and relative batch numbers of the copper wedges used in the assembly.

Firm1			Firm2			Firm3		
cc ID	Profile I/II/III	Profile IV	cc ID	Profile I/II/III	Profile IV	cc ID	Profile I/II/III	Profile IV
1001	A/A/A	A	2001	A/A/A	A	3001	A/A/A	A
1002	1/1/1	1	2002	1/1/1	1	3002	1/1/1	1
1003	1/1/1	1	2003	1/1/1	1	3003	1/1/1	1
1004	1/1/1	1	2004	1/1/1	1	3004	1/1/1	1
1005	9/9/9	9	2005	8/8/8	8	3005	6/6/6	6
1006	9/9/9	9	2006	8/8/8	8	3006	6/6/6	6
1007	9/9/9	9	2007	8/8/8	8	3007	6/6/6	6
1008	9/9/9	9	2008	8/8/8	8	3008	6/6/6	6
1009	9/9/9	9	2009	8/8/8	8	3009	6/6/6	6
1010	9/9/9	9	2010	8/8/8	8	3010	6/6/6	6
1011	9/9/9	9	2011	14/14/14	8	3011	6/6/6	6
1012	9/9/9	9	2012	14/14/14	8	3012	16/16/16	6
1013	15/15/15	9	2013	14/14/14	8	3013	16/16/16	6
1014	15/15/15	4	2014	14/14/14	8	3014	16/16/16	6
1015	9/9/9	9	2015	14/14/14	8	3015	16/16/16	6

5.3 Expected field harmonics versus measured

5.3.1 Sensitivity matrix

In this section the influence on the magnetic field induced by the copper wedge dimensions is evaluated. The sensitivity of each copper wedge dimension on multipoles in the hypothesis of an infinite elastic modulus is calculated; this is a good approximation since the ratio between the elastic modulus of the copper wedges and of the insulated cable blocks is larger than 20 [5.5]. Therefore, it has been assumed that cable blocks absorb the overall effect of copper wedges non-nominalities, keeping the same coil size. We also find that the problem is linear within the considered ranges, thus justifying the use of a sensitivity matrix. We considered the separated effects of each copper wedge, giving to the pair [ΔP1, ΔP2] of each profile the maximal allowed configurations: [0, 0.030] mm and [0.030, 0] mm and we computed the induced magnetic effects (see Table 5.3). All the possible configurations can be found as a linear combination of these two.

Table 5.3: Influence o the allowed non-nominalities of each profile on field harmonics in units. In the first two columns the two pairs of maximum displacement (30 μm) given to each profile are listed.

ΔP1 [mm]	ΔP2 [mm]	Δb_3	Δb_5	Δb_7
Profile I				
0.000	0.030	-0.2	-0.002	0.014
0.030	0.000	-0.3	0.04	0.055
Profile II				
0.000	0.030	0.2	0.08	-0.008
0.030	0.000	0.4	0.15	-0.036
Profile III				
0.000	0.030	0.3	-0.02	-0.005
0.030	0.000	0.6	-0.08	-0.008
Profile IV				
0.000	0.030	-0.1	-0.001	0.002
0.030	0.000	-0.1	0.002	0.004

Profile III has the strongest influence on b_3, whilst b_5 is mostly affected by Profile II. The largest effect on b_7 is given by Profile I. Profile IV does not influence in significant way any multipole. These values can be compared to the measured spread (one sigma) of the multipoles in the collared coil and to the width of the allowed range for the systematic according to beam dynamics specifications (see Table 5.4) [5.6]. The effect of a single non nominality - ΔP1 or ΔP2 - of each profile is, at most, one third of the measured sigma.

Therefore, copper wedges non-nominalities are not expected to contribute in a relevant way to the random component of the field harmonics. A detailed analysis of this problem is given in next section.

Table 5.4: Measured random components of the allowed field harmonics (1 sigma r.m.s.) and allowed ranges for the systematics given by beam dynamics [5.6].

	b_3	b_5	b_7
Random (1 sigma)	1.7	0.5	0.2
Allowed band	-4.48/1.12	-1.14/0.3	-0.79/0.31

5.3.2 Expected harmonics: evaluation and comparison with the measured ones

Multiplying the sensitivity matrix (Table 5.3) by the measured copper wedges non-nominalities, the expected shift in the multipoles due to the actual shape of these components is reconstructed.

The estimate is based on two hypotheses about the position of the wedges in the coil assembly; it can be placed either in contact with the external layer radius or with the internal circumference of the coil, with the wedge sliding along surface P (see Figure 5.7).

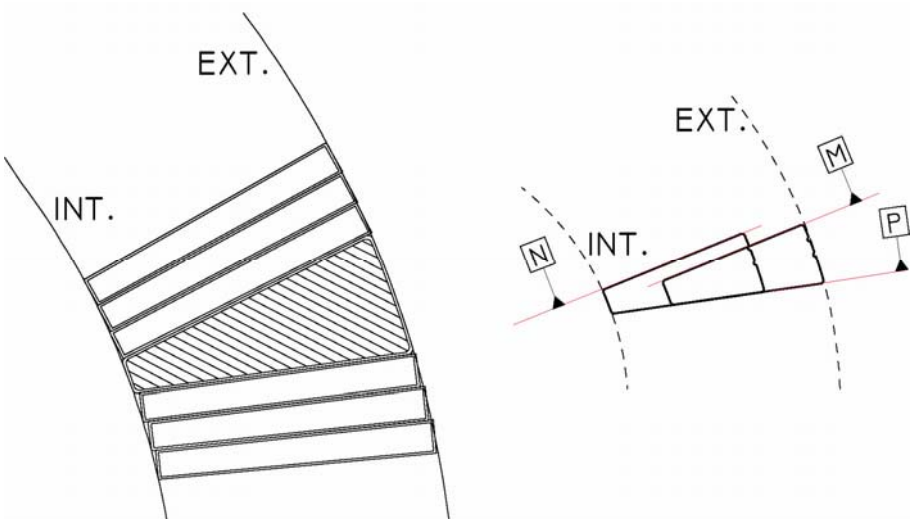

Figure 5.7: Definition of internal and external surfaces on which the copper wedges can be leant. On the right the two extreme configurations of the wedges locations are sketched.

The wedges position will match surfaces M or N depending on the assumption. In Table 5.5 we show the results of the computation of the effects on the first three odd multipoles due to the batches already used in the collared coils. We used both assumptions of internal and external contact. The two assumptions shall be taken as the extreme situations that can occur, the external contact being in general assumed as the most likely situation.

The batches PROT and A induce a non-negligible shift in field harmonics: they both give rise to a shift in b_3 of about -1.5 units, and a contribution of about -0.2 units to b_5 (negligible effect on b_7). For the other batches the effects on b_3 in the external contact hypothesis fluctuate from a minimum of -0.3 units for batch 6 up to a maximum of 0.6 of batch 8 and the average effect is small (less than 0.25 units). On the other hand, using the internal contact assumption, the effect is larger: up to 1.4 units for batch 9 and an average effect of 1 unit. The same happens for b_5, which is not affected in the hypothesis of external contact, whilst for internal contact there is an overall effect of 0.12 units.

Table 5.5: Magnetic effects of the measured copper wedge dimensions assuming both hypothesis of internal and external contact.

	Int. Contact			Ext. Contact		
Batch	Δb_3	Δb_5	Δb_7	Δb_3	Δb_5	Δb_7
PROT	-1.5	-0.26	0.066	-1.9	-0.35	0.071
A	-1.5	-0.18	0.046	-1.4	-0.23	0.017
1	0.2	0.11	0.033	0	0.02	0.006
6	0.5	0.16	0.011	-0.3	0.01	-0.005
8	1.3	0.09	-0.035	0.6	-0.06	-0.039
9	1.4	0.12	-0.051	0.5	-0.05	-0.048
14	0.6	0.09	0.008	0.2	-0.04	0.005
15	0.5	0.12	0.022	0.1	-0.04	0.001
16	0.5	0.11	0.028	0.1	-0.03	0.004
19	1.2	0.06	0.012	0.5	-0.05	-0.018
average	0.9	0.12	0.005	0.2	-0.01	-0.008

We then subtract the calculated effect of the copper wedges non–nominalities on the harmonics from the magnetic measurements of the collared coils (normalized to nominal polar shims [5.5]). Also in this case, we have taken into account both hypotheses for the calculation of ΔP1 and ΔP2; results are plotted in Figure 5.8, Figure 5.9 Figure 5.10 and are summarized in Table 5.6. The main effect is a large reduction of the trend of b_3 in the first dipoles (the first 3 being done with batch A), see Figure 5.8. The effects on b_5 and b_7 are less evident. This means that a relevant part of the initial trend in b_3 was due to the out-of-tolerance of copper wedges of batch A. In the hypothesis of an external contact, the spread in b_3 is reduced from 1.9 to 1.6 units when the effect of copper wedges is taken out (see Table 5.6). In the hypothesis of internal contact the effect is even larger. On the other hand, the situation of b_5 and b_7 is only weakly affected by copper wedges non-nominalities.

Table 5.6: Average and standard deviation of multipoles measured in the collared coils, separated according to different cross-sections, raw values and post-processed values where the effect of copper wedges is taken out.

		Cross section 1		Cross section 2-3	
		μ	σ	μ	σ
b_3	meas.	1.1	1.9	-1.9	1.1
b_3-Δb_3	int.	0.5	1.3	-2.6	1.2
b_3-Δb_3	ext.	1.0	1.6	-2.2	1.2
b_5	meas.	1.18	0.42	0.41	0.39
b_5-Δb_5	int.	1.09	0.41	0.32	0.4
b_5-Δb_5	ext.	1.22	0.43	0.45	0.4
b_7	meas.	0.631	0.161	1.126	0.085
b_7-Δb_7	int.	0.638	0.167	1.113	0.085
b_7-Δb_7	ext.	0.648	0.164	1.13	0.087

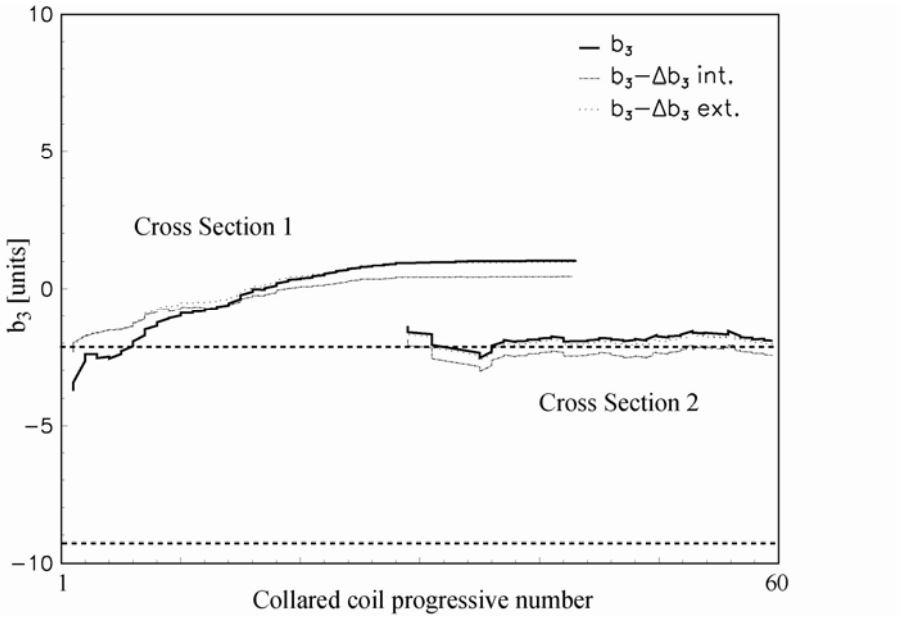

Figure 5.8: Running average of measured b_3 and of b_3 reduced to nominal copper wedges using both the assumptions for the evaluation of the non-nominalities.

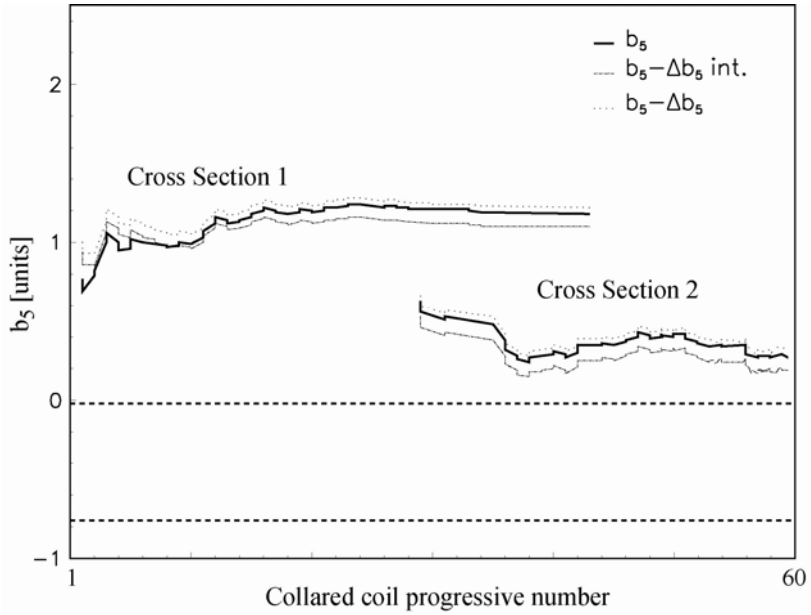

Figure 5.9: Running average of measured b_5 and of b_5 reduced to nominal copper wedges using both the assumptions for the evaluation of the non-nominalities.

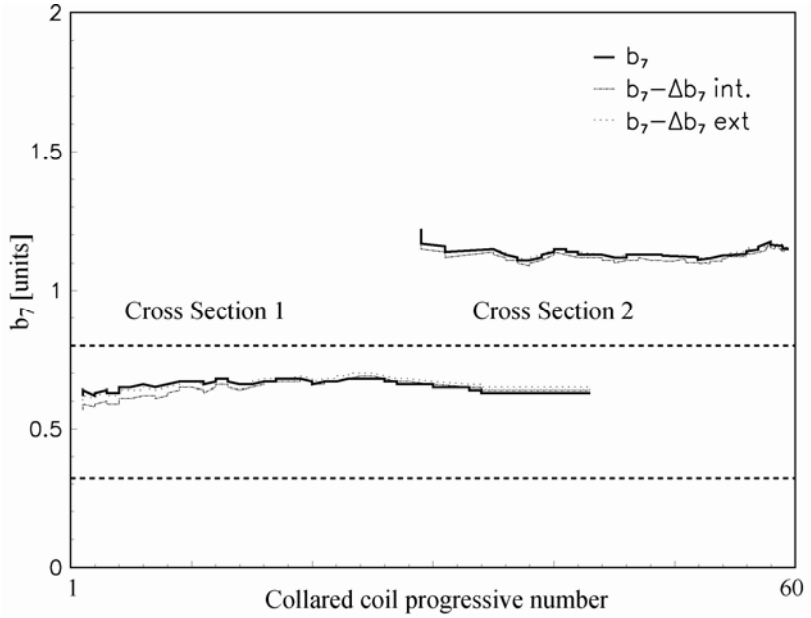

Figure 5.10: Running average of measured b_7 and of b_7 reduced to nominal copper wedges using both the assumptions for the evaluation of the non-nominalities.

5.4 Effect of the wedge successive production on random and systematic field components.

5.4.1 Monte–Carlo analysis

To foresee the effects of the non–nominalities of the whole wedge production on field quality, we analyzed with a Monte–Carlo method two different scenarios. We used this analysis to predict the influence on the random and on the systematic part of the multipoles.

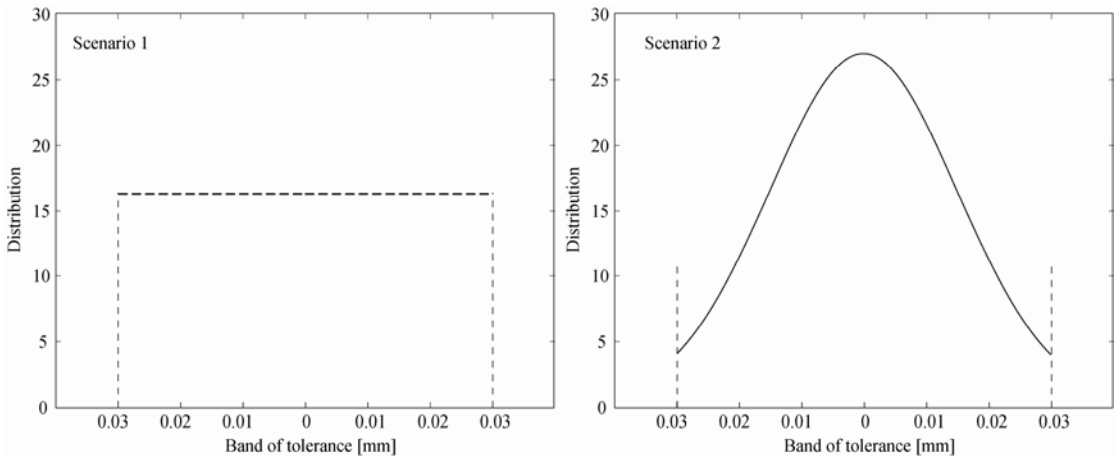

Figure 5.11: Two normalized distributions used for the Monte–Carlo simulation: the flat – scenario 1 - and the Gaussian (it has zero average and a standard deviation of 0.015 mm and truncated at two sigma) - scenario 2.

- Scenario 1. (Conservative) Flat distribution of ΔP1 and ΔP2 (20000 cases) between the dimensional tolerances [-0.030, +0.030] mm for each profile (Figure 5.11, left). With this scenario we simulate a situation in which the supplier is not keeping the production under control, but nevertheless selects and delivers pieces in tolerance.
- Scenario 2. (In–control process) Gaussian distribution of the non–nominalities (20000 cases) of each profile with zero average and a standard deviation equal to 0.015mm (one quarter of the allowed band) truncated at two sigma (Figure 5.11, right).

Using these two scenarios we compute the distributions of the field harmonics. Figure 5.12 refers to the non–nominalities distribution of scenario 1.

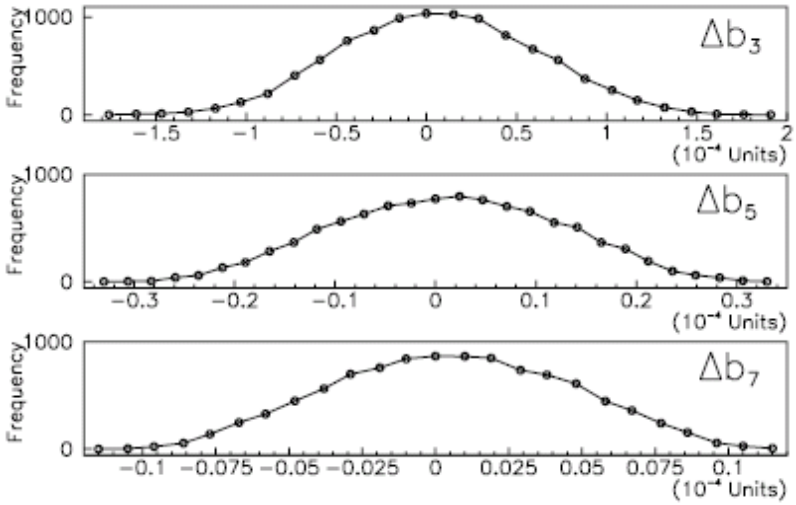

Figure 5.12: Multipoles distribution effects due to the flat distributions - scenario 1 - of the non–nominalities of the CW (10000 cases).

5.4.2 Effect on random components

The calculated standard deviations of the field harmonics due to copper wedge tolerances are listed in Table 5.7. The effect on the random is not relevant: in the worst scenario (the first one) we obtain one half of the measured standard deviation (see Table 5.4) of b_3, and one fifth of b_5 and b_7. As expected, sigma in scenario 1 are larger than in scenario 2.

Table 5.7: Expected standard deviation of the odd field harmonics due to copper wedges within tolerances.

	$\sigma_{\Delta b3}$	$\sigma_{\Delta b5}$	$\sigma_{\Delta b7}$
Scenario 1	0.53	0.11	0.040
Scenario 2	0.41	0.08	0.030
Measured	1.06	0.48	0.143

5.4.3 Effect on systematic components

We now evaluate the impact of the copper wedge tolerances on the systematic components of field harmonics taking into account the ranges allowed by beam dynamics. We assume that the results of the previous simulation, in the worst case (scenario 1), give the distribution of the average shift induced by the copper wedge tolerances on field harmonics. We then evaluate what is the probability that a given systematic multipole is shifted by a quantity equal to the whole allowed range: results show that this probability is close to zero (see Table 5.8, first row). This means that it is very unlikely that copper wedges within tolerances would shift the systematic multipoles of a quantity equal to the allowed range. Indeed, we also computed the probability of shifting the systematic of 1/2, 1/3 and 1/4 of the allowed range. In this case we find non-zero probabilities. For instance, there is a 6 % probability that copper wedges produced within tolerances can shift b_5 by half of the allowed range.

Therefore, there is a non-negligible probability that a relevant fraction of the allowed range for systematic components is “eaten” by the copper wedge tolerances. The situation is critical especially for b_5 and b_7, since the allowed ranges are very narrow. The effects on b_3 are much less critical. In order to avoid these effects on

systematic components, one should carefully control how the average of the copper wedge non–nominalities moves during the production. The above analysis shows that the scenario where average of non–nominalities passes from one edge of the tolerance band to the other one should be avoided. Hence, we must point out that copper wedges should be not only within tolerances but also without large shifts of their non–nominalities average within the allowed band.

Table 5.8: Probability of a shift of the systematics out of the considered fractions of the allowed bands (see Table 2) for copper wedges within tolerances.

Probability of a shift > band fraction [%]			
Band fraction	b_3	b_5	b_7
1	<0.01	<0.01	<0.01
1/2	0.04	6	0.4
1/3	4	26	13
1/4	13	37	21

5.5 End of copper wedge production

In this section the previous study on the initial copper wedge production is extended to the almost one thousand of assembled collared coils that feature the cross section 3. Knowing the batches used in each dipole and their geometry, we reconstruct the effect induced by such components on the field quality. A comparison between values expected from copper wedge measured dimensions and magnetic measurements are given in Figure 5.13. In Table 5.9 and Table 5.10 the systematic and random components of the influence of the copper wedges production are given.

The effect of the production of the copper wedges on the magnetic field of the LHC main dipoles is small. The largest effect is found on the induced random component of b_3, which account for ¼ of the measured values.

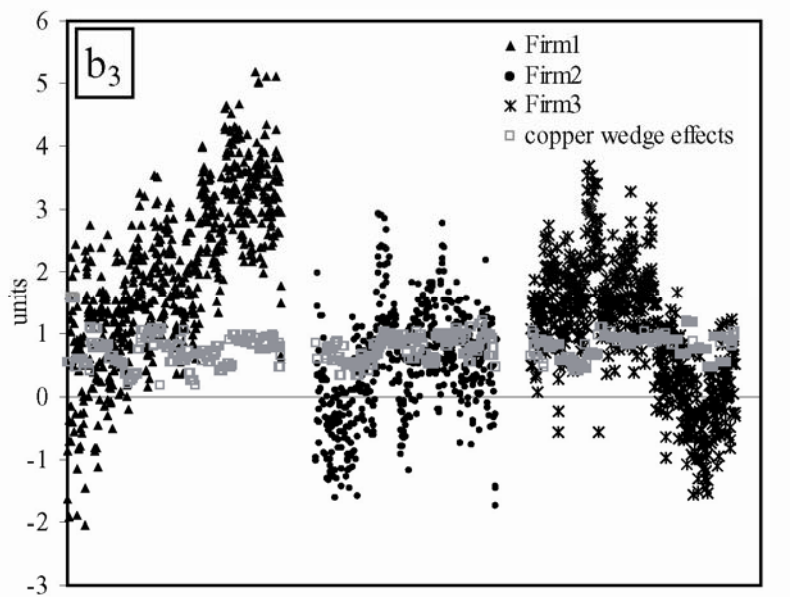

Figure 5.13: Measured b3 in the collared coil of the three cold mass assemblers and the b3 induced by the copper wedges inserted in the apertures.

Table 5.9: Random component of the field harmonic induced by the production of the copper wedges.

CMA - sample	b3	b5	b7
firm1 - 309	0.25	0.05	0.02
firm2 - 261	0.29	0.05	0.02
firm3 - 280	0.19	0.05	0.02
all - 850	0.25	0.05	0.02
all - measured	1.06	0.48	0.143

Table 5.10: Systematic effect of the copper wedges non nominalities on the magnetic field of the collared coil**.**

CMA - sample	Δb3	Δb5	Δb7
firm1 - 309	0.72	0.05	0.01
firm2 - 261	0.82	0.06	0.00
firm3 - 280	0.80	0.07	0.00
all - 850	0.78	0.06	0.01

5.6 Conclusion

We have analyzed the measured dimensions of the copper wedges and therir influence on field quality.

- The first 3 collared coils (one per firm) were produced with one batch (named A) which is out of tolerance and dimensionally very different from the rest of the production. All the other batches are within the tolerances with local point that are out.
- Magnetically, the four profiles have a different effect on multipoles: roughly speaking, b_3 is mostly influenced by profile III, b_5 by profile II and b_7 by profile I. profile IV does not influence significantly any multipole.
- We found a relevant effect on the b_3 (1.5 units) of the copper wedges of batch A, which is visible in the collared coil magnetic measurements. This explains part of the upward trend observed in b_3 measured in the first 25 collared coils. This effect is negligible on b_5 and b_7.
- The copper wedge tolerances are not the main source of the random component measured in the manufactured dipoles: they account only for 1/3 to 1/5 of the measured values. Indeed, there is a non-negligible probability that copper wedges within tolerance drive the systematics b_5 and b_7 towards the edge of the allowed ranges imposed by beam dynamics.
- It has been shown that the advices given at the beginning of the wedges production brought to a more careful control on the manufacturing and as a result, the total influence of the copper wedge dimensions on the collared coil magnetic field is not relevant.

References

[5.1] B. Bellesia et al., *"Influence of copper wedges dimensions on field quality in the main LHC dipole"*, CERN LHC Project Report **630** (**2003**)

[5.2] Drawings: *Cross Section n.1*: LHCMB A0052, LHCMB A0054, LHCMB A0056, LHCMB A0058; *Cross Section n.2*: LHCMB A0177, LHCMB A0178, LHCMB A0179.

[5.3] *"LHC technical specification for the supply of 1158 cold masses of the superconducting dipole magnets for the LHC collider", **Annex C3, G1***, LHC Project Document **LHC–MB A–C1–0006**.

[5.4] E. Todesco, L. Bottura, S. Pauletta, V.Remondino, S. Sanfilippo, W. Scandale, "*Status Report on Field Quality in the Main LHC Dipoles*", CERN **LHC Project Report 579** (**2002**).

[5.5] P. Ferracin, W. Scandale, E.Todesco, D. Tommasini, "*Modeling of Coil Pre-stress Loss During Cool-down in the Main Dipoles of the Large Hadron Collider*" , IEEE Trans. Appl. Supercond. **Vol. 12** (**2002**) 1705–7, also in CERN **LHC Project Report 534** (**2002**).

[5.6] S. Fartoukh, O. Bruning, "*Field quality specification for the LHC main dipole magnets*" CERN **LHC Project Report 501** (**2001**).

Chapter 6

Austenitic steel collars

The austenitic steel collars, which clamp the superconducting coils and retain the Lorentz forces during the powering of the magnet [6.1], are, after the cables, the most complicated LHC dipole component from both mechanical and geometrical point of view. The aim of the chapter is to examine how the austenitic steel collars influence the magnetic field quality of the LHC dipole magnets. An analysis of the dependence of field quality on the collar shape and a comparison of the field quality spread expected from this component with the measured one was carried out in [6.2],[6.3] and [6.4].

The goals of the study are:

- To verify if the geometrical tolerances on collars have been kept and if there are trends in the production of the collars.
- To investigate whether magnets made with different collar suppliers present visible differences in field quality.
- To estimate through models the impact of the different assembly procedures used by the manufactures on the field harmonics, and to compare with the magnetic measurements.
- To evaluate the effect of the measured collar dimensions on field quality, and to compare these estimations to magnetic measurements.

In section 1, general information about collars is provided: types, manufacturers, production procedure and the standard dimensional controls used to monitor the production. The available sets of data are presented in section 2. The geometric dimensions of the collars and their dependence on the manufacturer are studied, and the dependence of measured field quality at room temperature on the collar manufacturer is analyzed in section 3. In section 4, after having computed the sensitivity tables giving the dependence of magnetic field harmonics on the collar geometry, we use the measured dimensions of the collars to estimate their impact on field quality, comparing these results with the magnetic measurements.

6.1 Production

6.1.1 Collar Types

The LHC main dipole cross section features a two-in-one design, i.e. the two particle beams pass in opposite directions through the same magnet in two separated apertures. The cross section in the straight part of the collared coil is sketched in Figure 6.1. The

collars are the structure that keeps the superconducting coils under pre-stress to reduce movements during the magnet powering. The LHC dipole is the only case of magnet using “two in one” collar, i.e. the same pair of collars for the two apertures; all the other magnets have independent retaining structures per aperture. The collars are made of a high Mn content austenitic grade steel (Nippon Steel YUS 130 S) and are manufactured through a process of fine-blanking starting from 3 mm thick austenitic steel coils, with tolerances of the order of 20-30 micrometer. The magnetic permeability must be less than 1.003 (for $H=8\cdot10^4$A/m at 1.9 K) in order not to affect the magnetic field [6.5]. There are three shapes of collars along the magnet length to fit the different geometry of the cross section [6.6]:

- Shape A - straight part collars: about 4400 pieces per magnet
- Shape B - head collars: 120 pieces per magnet
- Shape C - layer jump collars: 95 pieces per magnet

Each shape is manufactured in two different types: a “long” collar (labeled by 1) which is coupled with a “short” one (labeled by 2, see Figure 6.1 for the case of the shape A). The structure is kept in place by the insertion of the three collaring rods. There are six different collars to be manufactured for a total of about 10^7 pieces for the whole magnet production. Since in this study we are interested in the magnetic field quality, which is dominated by the straight part of the magnet, we will analyze only the production of the shape A neglecting the impact of shapes B and C.

6.1.2 Production and quality control

CERN has shared the collar production between two suppliers [6.6]: S_1 (5/8 of the total) and S_2 (3/8 of the total). The same raw material (austenitic steel) is delivered by the same manufacturer to both firms. Each collar type is delivered in batches to the three firms that manufacture the cold masses (after the approval of CERN). The batches produced by S_2 are mainly delivered to the cold mass assembler Firm3, whereas Firm1 and Firm2 use collars produced by S_1. Batches of collar type A1 and A2 contain about 4400 pieces, enough to fill a magnet plus some spare pieces used for the acceptance tests.

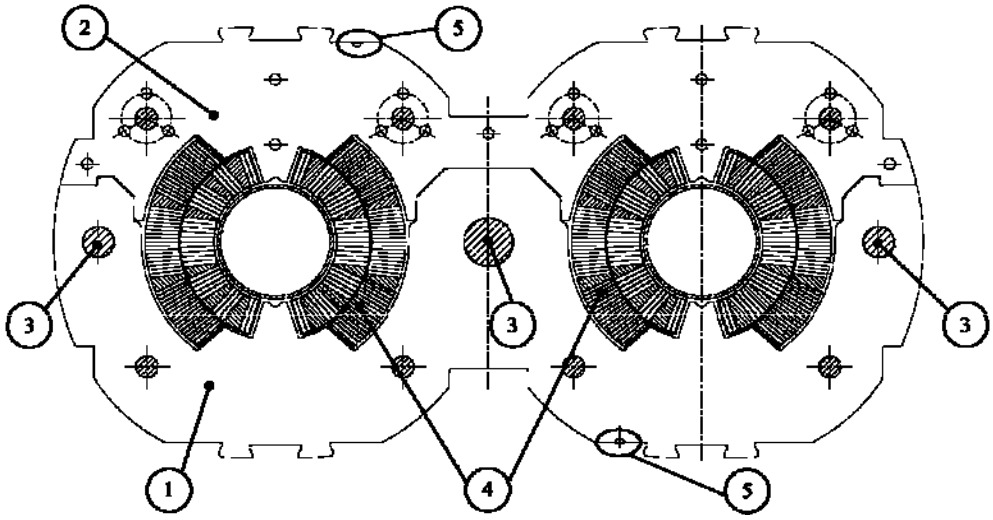

Figure 6.1: Collared coil layout. 1- Collar type A1; 2- Collar type A2; 3- collaring rods; 4- Superconducting coils; 5 – Collar witness marks.

The supplier S_2 measures three collars per batch whereas S_1 only one. The location of the dimensional control of the collars types A1 and A2 are indicated with black spots in Figure 6.2 and Figure 6.3; one has about 90 measured points per collar. All collars have a "witness mark" on one side used to distinguish the right from the left part. In our analysis, we define the different parts of the collars as:

- T1 right aperture
- T2 left aperture
- Dx right part of each aperture
- Sx left part of each aperture

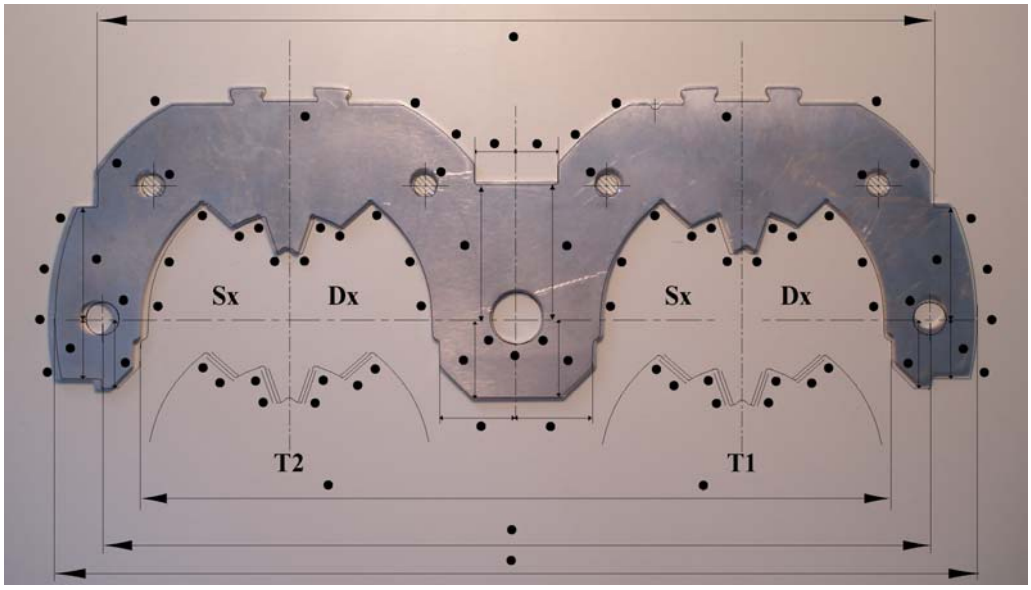

Figure 6.2: Collar type A1. The black spots indicate the positions of the measured points used for the dimensional quality control.

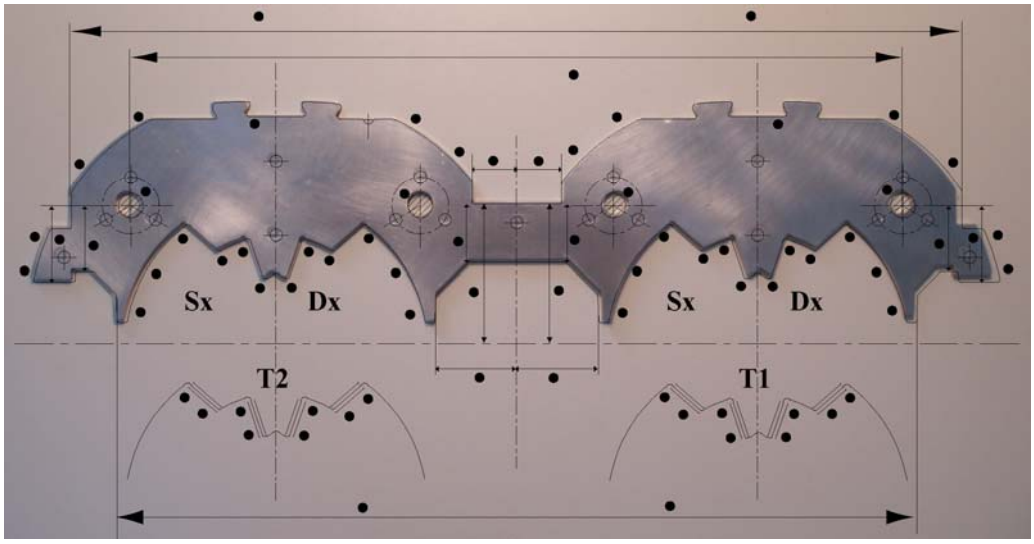

Figure 6.3: Collar type A2. The black spots indicate the position of the measured points used for the dimensional quality control

6.1.3 Collar assembly procedures

Significant differences can be found in the procedure used to assembly the collars around the coil in the three cold mass assemblers. Each collar can be mounted on the coil in four different positions. S_A is the surface of the collar visible during the dimensional measurements (surface of Figure 6.2 and Figure 6.3, witness mark on the right) and S_B the opposite one (witness mark on the left). The collars can be assembled with S_A towards the connection side (in this case the witness will be on the right side, looking from connection side), or towards the non-connection side (witness mark on the left side, looking from connection side). Moreover, each collar can be mounted with the cavity downward (U, witness mark on the top) or upward (L, witness mark on the bottom). All the four assembly possibilities of collar A1 are showed in Figure 6.4; in the same way the assembly positions of the collar A2 are defined. In total eight assembly positions are possible (to assemble a type A1 with a type A2).

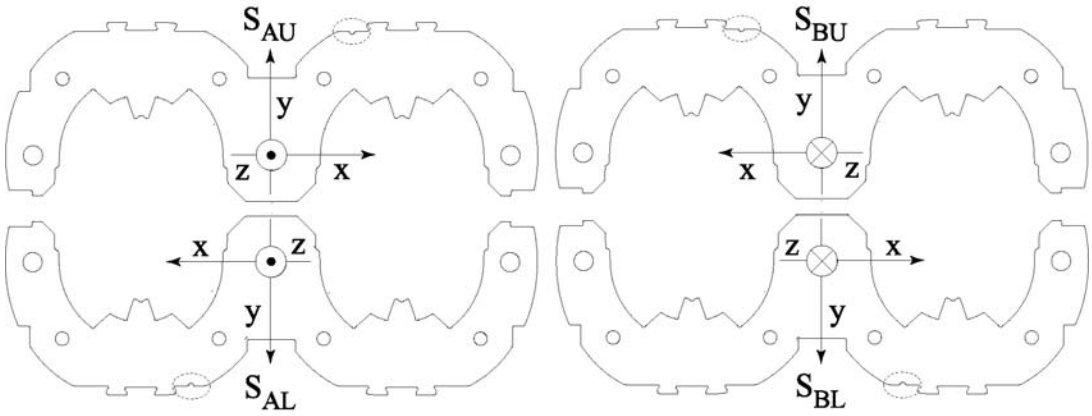

Figure 6.4: The four possible assembly positions for collars of type A1; the witnesses are marked with a dashed circle.

The assembly unit is the “pair of collars” which is a collar type A2 superimposed to a collar type A1, and locked by four pins inserted in the smaller holes (see Figure 6.4). Each of the three CMA has a different procedure to assemble the collars around the superconducting coils:

- Firm1 assembles pair of collars that are then mounted by flipping them around the “x” axis using only two over the four possible configurations (in Figure 6.4: S_{AU} and S_{BL}).
- Firm2 assembles packs of 5 pairs that are then mounted using all the four possible positions of Figure 6.4.
- Firm3 also assembles packs of collars (10 pairs) but the packs are rotated around the “z” axis, perpendicular to the plane of the drawing, hence only two possible mounting positions are used (in Figure 6.4, S_{AU} and S_{AL}: the collars are rotated only along the “z” axis) [6.7].

6.2 Available data

6.2.1 Collars dimensions

At the end of 2005 when this work was carried out, more than 900 batches of collar type A1 and A2 have been manufactured, tested and delivered to the cold mass assemblers (about 400 from S_2 and about 500 from S_1). At the beginning of the production, the measurements of the geometrical dimensions of the collars were not sufficiently precise to perform an adequate quality control. Then, starting from batch 177 of the supplier S_2 and from batch 212 of the supplier S_1, an improvement of the measurement system was implemented. For this reason, in our analysis we only use the geometrical data of collars after the improvement of the measurement system (see Table 6.1).

Table 6.1: Numbers of collar batches used in the geometrical analysis.

Collar supplier	Batches available
S_2	**182 -** used in Firm3
S_1	**76 -** used in Firm1
S_1	**71 -** used in Firm2

6.2.2 Collared coil measurements at room temperature

Magnetic measurements of 741 collared coils were analyzed. During the first period of the production, the cross section lay out of the superconducting coil was modified two times to better match the magnetic field quality targets required by the beam dynamics. About 35 magnets have been produced with cross-section 1, 145 with cross-section 2, and the rest with cross-section 3. These magnets differ in the systematic allowed multipoles, whereas they should have the same behavior as far as the not allowed multipoles are concerned. Therefore, the analysis of the not allowed components of the magnetic field includes the whole amount of data (about 740 collared coils, see Table 6.2). On the other hand, the analysis of the allowed components is restricted to the cross-section 3 magnets (545 collared coils).

Table 6.2: Numbers of collared coils used in the field quality analysis.

Collar manufacturer	Cold mass assembler	Measured collared coils (all)	Measured collared coils (X-section 3)
S_2	Firm1	**13**	**8**
	Firm2	**-**	**-**
	Firm3	**335**	**279**
S_1	Firm1	**199**	**139**
	Firm2	**182**	**119**
	Firm3	**9**	**0**

6.3 Trends in collar geometrical data and in magnetic measurements at room temperature

6.3.1 Dimensional analysis

During the dimensional controls of the collars, about 90 measurements per piece are taken. We chose to analyze all the measurements performed in the “cavity”, which is the part where the superconducting coil is allocated. The nominal shape of the inner cavity of the collar is defined by the arc of circles A and B (Figure 6.5, left)., with a radius of 60.98 mm and 44.88 mm respectively and a tolerance of +/-0.030 mm. The straight lines C and D, both having a tolerance of +/-0.025 mm. A comparison between the measurements carried out at the supplier and at CERN indicates that the precision is about 0.010 mm [6.9].

The surfaces B, C and D are measured in two points at the edges, the surface A is measured in an additional point in a central position. Measurements are always referred to the nominal shape. We do not discuss here the effect of errors in the holes for the locking rods, which is very complex to be analyzed since it can lead to a shift in the position of the collars and to collar deformations during the assembly. An analysis carried out in [6.8] shows that some of these effects are not negligible.

Since no information on the shape between two measured points of a same surface is available, a hypothesis of linearity between the two is adopted as in [6.2],[6.3] and [6.4]. Using this assumption, the non nominalities are split in a shift and a tilt (Figure 6.5, right part). The shift is defined as the average of the measurements (always expressed with respect to the nominal case) taken on the surface and it is positive when one has more material than in the nominal case. The tilt is the difference between the average of the measurements taken on the surface, and one measurement taken on the edge. In right the part of one cavity the positive tilt is defined as an anti-clockwise rotation of the surface whilst the positive tilt of the surfaces of the left side of the cavity is a clockwise rotation (see Figure 6.5). For each of the two collar type we consider 16 surfaces in the two cavities for a total of 16 shifts and 16 tilts.

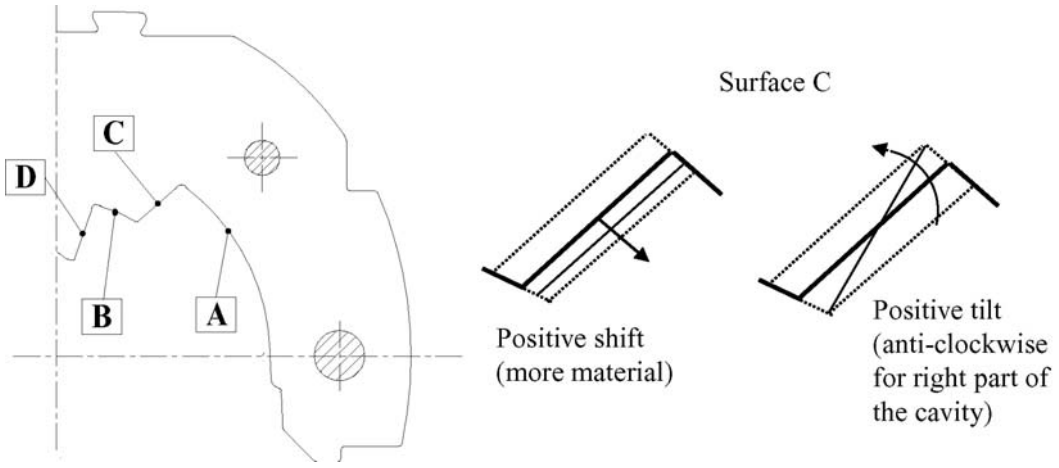

Figure 6.5: Labeling of the analyzed collar surfaces (left), and conventions on signs for a shift and for a tilt (right).

We first divided the collar production according to the collar suppliers, then the two productions are separated with respect to the dipole manufacturer and finally each sub set is ordered with respect to the collar batch number. The dimensional analysis is performed over the sample given in Figure 6.2 and summarized in Table 6.3 and Table 6.4. The results show that there are not significant differences in the geometry between the two suppliers. As an example, in Figure 6.6 the dimensions of shift and tilts of surfaces of the types A1 are showed. The values measured for the shifts are close or slightly above the tolerances, whereas the values measured for the tilts exhibit smaller standard deviations. The shifts of the collars type A1 of the supplier S1 have a larger spread with respect to the ones of the collars of S2.

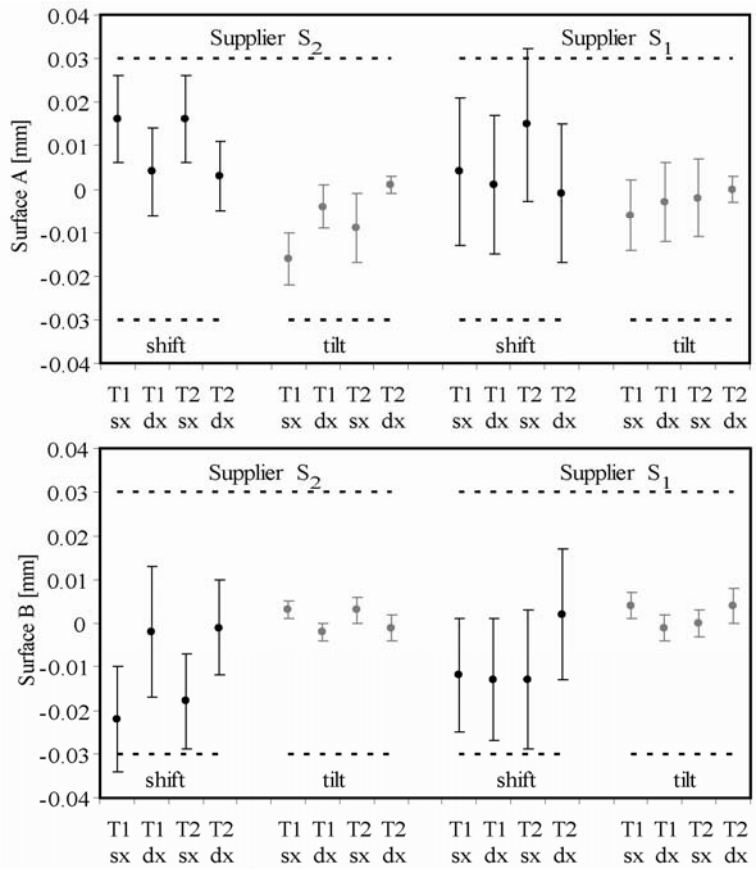

Figure 6.6: Averages and standard deviations (tolerance bars) of the shifts and tilts of surfaces A and B of the collar type A1 taken into account in the analysis divided w.r.t. the two suppliers S_2 and S_1.

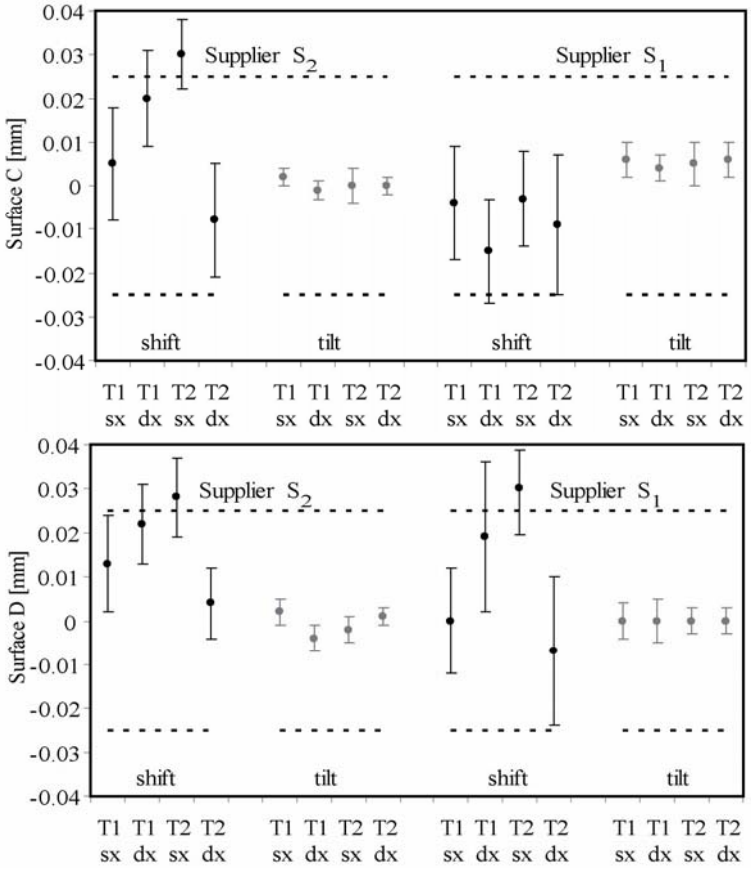

Figure 6.7: Averages and standard deviations (tolerance bars) of the shifts and tilts of surfaces C and D of the collar type A1 taken into account in the analysis divided w.r.t. the two suppliers S_2 and S_1.

Table 6.3: Averages (μ) and standard deviations (σ)of the shifts and tilts of the four surfaces of the collar type A1 taken into account in the analysis divided w.r.t. the two suppliers S_2 and S_1

Shift									
		S_2				S_1			
		T1 - sx	T1 - dx	T2 - sx	T2 - dx	T1 - sx	T1 - dx	T2 - sx	T2 - dx
Surf. A	μ	0.016	0.004	0.016	0.003	0.004	0.001	0.015	-0.001
	σ	0.010	0.010	0.010	0.008	0.017	0.016	0.020	0.016
Surf. B	μ	-0.022	-0.002	-0.018	-0.001	-0.012	-0.013	-0.013	0.002
	σ	0.012	0.015	0.011	0.011	0.013	0.014	0.016	0.015
Surf. C	μ	0.005	0.020	0.030	-0.008	-0.004	-0.015	-0.003	-0.009
	σ	0.013	0.011	0.008	0.013	0.013	0.012	0.011	0.016
Surf. D	μ	0.013	0.022	0.028	0.004	0.000	0.019	0.030	-0.007
	σ	0.011	0.009	0.009	0.008	0.012	0.017	0.016	0.017
Tilt									
		S_2				S_1			
		T1 - sx	T1 - dx	T2 - sx	T2 - dx	T1 - sx	T1 - dx	T2 - sx	T2 - dx
Surf. A	μ	-0.016	-0.004	-0.009	0.001	-0.006	-0.003	-0.002	0.000
	σ	0.006	0.005	0.008	0.002	0.008	0.009	0.009	0.003
Surf. B	μ	0.003	-0.002	0.003	-0.001	0.004	-0.001	0.000	0.004
	σ	0.002	0.002	0.003	0.003	0.003	0.003	0.003	0.004
Surf. C	μ	0.002	-0.001	0.000	0.000	0.006	0.004	0.005	0.006
	σ	0.002	0.002	0.004	0.002	0.004	0.003	0.005	0.004
Surf. D	μ	0.002	-0.004	-0.002	0.001	0.000	0.000	0.000	0.000
	σ	0.003	0.003	0.003	0.002	0.004	0.005	0.003	0.003

Table 6.4: Averages (μ) and standard deviations (σ) of the shifts and tilts of the four surfaces of the collar type A2 taken into account in the analysis divided w.r.t. the two suppliers S_2 and S_1

Shift									
		S_2				S_1			
		T1 - sx	T1 - dx	T2 - sx	T2 - dx	T1 - sx	T1 - dx	T2 - sx	T2 - dx
Surf. A	μ	0.017	-0.012	0.016	0.002	-0.003	-0.009	-0.004	-0.014
	σ	0.009	0.012	0.012	0.007	0.023	0.014	0.026	0.014
Surf. B	μ	0.010	0.003	0.011	0.019	-0.020	-0.011	-0.009	-0.010
	σ	0.009	0.009	0.010	0.013	0.015	0.019	0.017	0.017
Surf. C	μ	0.015	-0.002	0.016	0.022	-0.017	-0.021	-0.010	-0.015
	σ	0.009	0.011	0.010	0.011	0.013	0.015	0.013	0.011
Surf. D	μ	0.003	0.018	0.018	0.017	-0.025	-0.022	-0.014	-0.020
	σ	0.009	0.009	0.010	0.008	0.013	0.013	0.014	0.010
Tilt									
		S_2				S_1			
		T1 - sx	T1 - dx	T2 - sx	T2 - dx	T1 - sx	T1 - dx	T2 - sx	T2 - dx
Surf. A	μ	-0.008	-0.003	-0.005	0.001	0.001	0.006	0.005	0.000
	σ	0.005	0.004	0.004	0.002	0.007	0.008	0.006	0.004
Surf. B	μ	0.001	0.002	0.003	0.001	0.003	0.000	0.001	0.003
	σ	0.003	0.002	0.002	0.002	0.004	0.003	0.003	0.004
Surf. C	μ	-0.001	-0.001	-0.001	-0.001	0.002	-0.001	0.000	0.002
	σ	0.003	0.002	0.003	0.002	0.003	0.004	0.004	0.003
Surf. D	μ	0.001	0.001	0.000	0.001	0.000	-0.002	-0.003	0.000
	σ	0.002	0.003	0.003	0.002	0.004	0.004	0.004	0.004

6.3.2 Harmonics versus cold mass assembler and collar supplier

The aim of this computation is to understand if there is a mark of the collar manufacturer on field harmonics. For each multipole mean value and standard deviations were calculated, splitting the data according to the collar manufacturer and to the cold mass assembler. Results are given in Table 6.5 and Table 6.6 and trend plots are given in Figure 6.8, Figure 6.9 and Figure 6.10. The results can be summarized as follow:

- Allowed multipoles:
  - The collar manufacturer does not affect the allowed multipoles: Firm1 has 8 magnets made with collars S_2 and 139 with collars S_1, and the two sets have similar averages for b_3, b_5, b_7. This means that the two collar productions give same effect on the allowed multipoles.
  - Systematic differences between firms observed for b_5 (Firm1 has 1 unit more than Firm2-3) and b_7 (Firm2 has 0.2-0.3 units less that Firm1-3) cannot be due to the collar manufacturer, since Firm1 and Firm2 mostly use the same collar manufacturer S_1.
- Not allowed multipoles:
  - Also in this case the comparison of 13 magnet of Firm1 assembled with collars S_2 to the 199 assembled with collars S_1 shows no relevant systematic difference in the not-allowed harmonics.
  - The strong negative systematic a_3 component in Firm1 (around 0.4 units) is observed both with collars S_2 and S_1 and therefore it is not due to the collar supplier. A similar remark can be made for the

systematic a_4 observed in Firm2 with S_1 collars if compared with the values of the same multipole of Firm1 with collars S_1 and S_2.

Table 6.5: Average of magnetic field harmonics, in units of 10^{-4} at R_{ref}=17mm, measured at room temperature and sorted with respect to the collar and dipole manufacturer

Col	Dipole	N	b3	b5	b7	N	b2	b4	a2	a4	a3	a5
	Firm1	8	-2.10	**0.05**	1.17	13	-0.18	-0.03	0.07	-0.03	**-0.23**	0.06
S_2	Firm2	-	-	-	-	0	-	-	-	-	-	-
	Firm3	279	-1.59	-0.56	1.17	335	-0.10	-0.05	0.64	-0.09	0.51	0.18
	Firm1	139	-1.88	**0.29**	1.21	199	-0.08	-0.02	0.26	-0.02	**-0.31**	0.04
S_1	Firm2	119	-2.87	-0.79	**0.87**	182	-0.14	-0.05	0.12	**0.37**	**-0.44**	0.00
	Firm3	-	-	-	-	9	0.05	-0.04	-0.04	-0.05	0.16	0.07

Table 6.6: Standard deviation of magnetic field harmonics, in units of 10^{-4} at R_{ref}=17mm, measured at room temperature and sorted with respect to the collar and dipole manufacturer.

Col	Dipole	N	b3	b5	b7	N	b2	b4	a2	a4	a3	a5
	Firm1	8	0.88	0.38	0.08	13	1.00	0.15	1.11	0.28	0.30	0.06
S_2	Firm2	0	-	-	-	0	-	-	-	-	-	-
	Firm3	279	0.80	0.22	0.06	335	0.78	0.09	0.94	0.29	0.32	0.09
	Firm1	139	1.10	0.32	0.08	199	0.52	0.12	1.21	0.26	0.27	0.08
S_1	Firm2	119	0.92	0.31	0.12	182	0.41	0.09	1.07	0.31	0.28	0.08
	Firm3	-	-	-	-	9	0.58	0.12	0.90	0.18	0.29	0.05

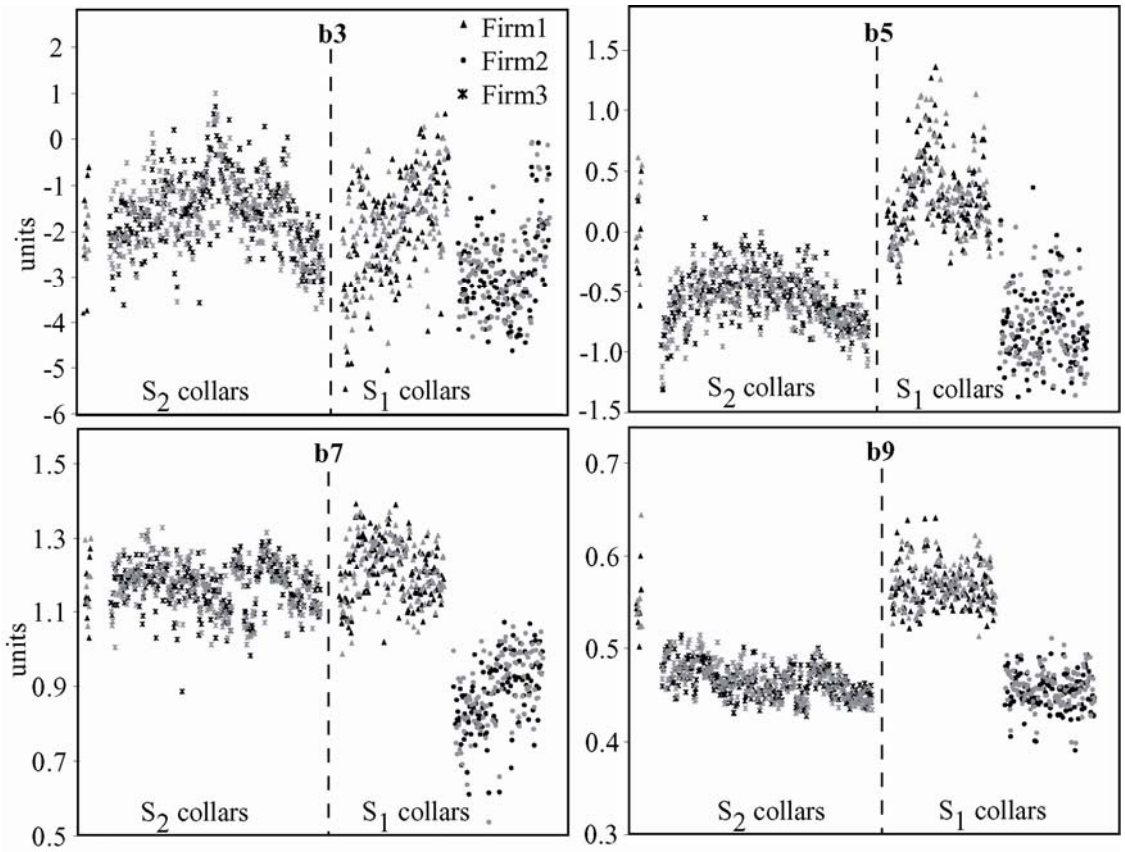

Figure 6.8: Allowed magnetic field harmonics measured at room temperature, sorted with respect to the collar and dipole manufacturer. The black markers are the measurement of aperture 1 and the grey of aperture 2.

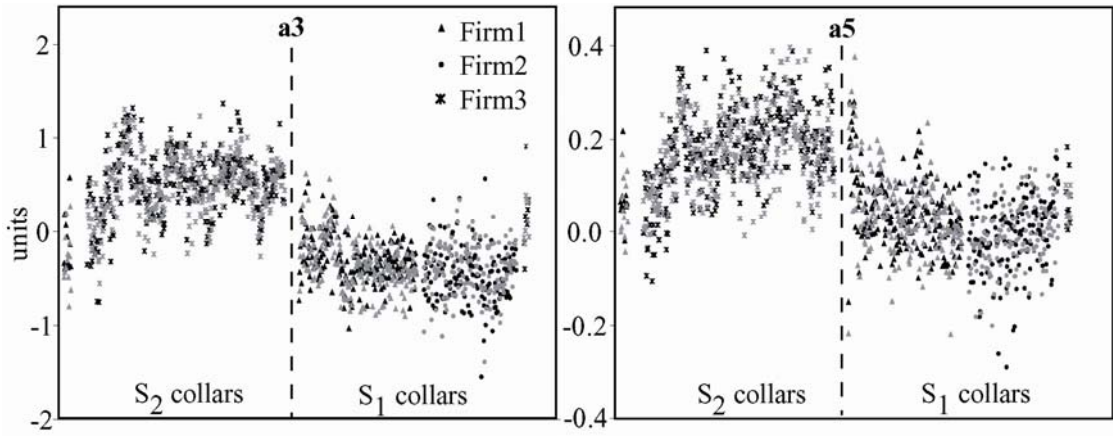

Figure 6.9: Odd skew harmonics measured at room temperature, sorted with respect to the collar and dipole manufacturer. The black markers are the measurement of aperture 1 and the grey of aperture 2.

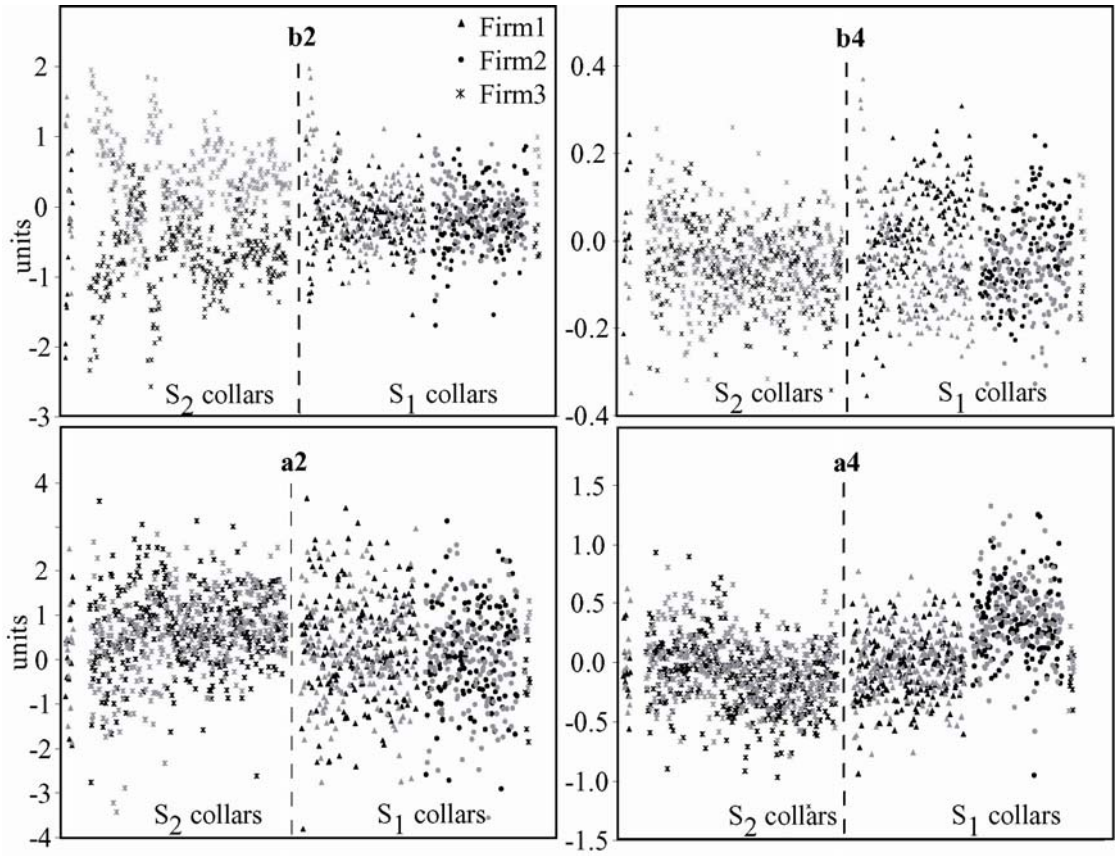

Figure 6.10: Even normal and skew field harmonics measured at room temperature, sorted with respect to the collar and dipole manufacturer. The black markers are the measurement of aperture 1 and the greys of aperture 2.

6.3.3 Harmonics vs collar assembly procedures

The three assembly procedures adopted by the three cold mass assemblers have a different impact on the field harmonic classes:

- Firm1: Since the collars are flipped around the horizontal axis, but not around the vertical one, any up-down asymmetry is cancelled, but not a

left-right asymmetry with respect to the magnet center. Therefore, even skew multipoles are zero by construction, and no correlation of field harmonics is expected between the two apertures.

- Firm2: Since the collars are flipped around both the horizontal and the vertical axis, any up-down and any left-right asymmetry are cancelled. Therefore, even skew multipoles are zero by construction, and there is a perfect correlation between the two apertures.
- Firm3: Since the collars are rotated by 180° around the magnet center, a systematic asymmetry between the two cavities of the collars would create up-down systematic asymmetries in each one of the apertures, with opposite sign. Therefore, even skew multipoles can be different from zero, but the correlation between apertures is intrinsically perfect.

The results are given in Table 6.7, where only the samples of more than 30 magnets have been considered to have statistical significance. One can make the following remarks:

- Allowed multipoles of the different apertures of a same magnet are always correlated. This correlation cannot be due to the assembly procedure, since it is different in the Firms and according to it, no correlation should be found for Firm1. This unexplained phenomenon was observed already for the pre-series; we remind the reader that the LHC dipoles are the first one to have a twin collar, and therefore no previous experience on the correlation between apertures of the same magnet is available.
- In Firm3, where a complete correlation between apertures is expected according to the assembly procedure, we see it for b_2, a_3, and partially for a_5. This means that the collar shape is the driving mechanism for these multipoles in this Firm. The fact that this correlation is not observed for b_4, a_2 and a_4, implies that for these multipoles the main source of imperfections is given by other components that are not correlated between apertures.
- In Firm1, we observe no correlation between apertures on not allowed multipoles, as expected from the collar assembly procedure. A weak correlation is observed for a_3 and a_5. This could come from a systematic asymmetry in the production of the coils, whose assembly procedure creates odd skews if the coil has a left-right asymmetry. If the only source of a_2 and a_4 were the collars, they should be zero because of the assembly procedure. The non-zero values measured for Firm1 are driven by other mechanisms, which are not correlated between apertures.
- In Firm2, we observe no correlation on even normal multipoles. Since from the assembly procedure a good correlation is expected for all multipoles, also in this case one can state that for Firm2 the main source of imperfections affecting b_2 and b_4 are not the collars. The weak correlation observed for a_3 and a_5 could be either due to the collars or to the production of the coil as discussed for Firm1. For a_2 and a_4 the same argument used for Firm1 holds.

Table 6.7: Coefficients of the correlations between the field harmonics measured in the two magnet apertures. In bold correlations coefficients larger than 0.7.

Col	Dipole	N	b_3	b_5	b_7	N	b_2	b_4	a_2	a_4	a_3	a_5
S_2	Firm3	279	**0.70**	**0.83**	**0.80**	335	**0.77**	0.29	0.09	0.04	**0.71**	0.59
S_1	Firm1	139	**0.76**	**0.83**	**0.79**	199	0.22	0.38	0.07	0.05	0.55	0.49
S_1	Firm2	119	**0.78**	**0.81**	**0.89**	182	0.29	0.30	0.06	0.14	0.60	0.56

6.4 Expected field harmonics versus measured

6.4.1 Sensitivity Matrix

A numerical magneto-static model was used to determine the dependence of the harmonics on the geometrical dimensions of the collars. In this case we assumed the collars to be infinitely rigid; under this assumption the superconducting cable and the cable insulation absorb all changes of the collar shape.

In the numerical calculation, it is assumed that each part of the inner collar contributes in an independent manner. We determined the sensitivities of the shifts and tilts of the surfaces A, B, C and D of the right part of the aperture T1; the calculated values for a positive geometrical error of +0.1 mm are shown in Table 6.8. For the surface B, the sensitivity of the positive and negative tilt since they do not give rise to opposite geometrical movements of the coils were evaluated. We marked in bold the highest sources of field errors: the largest effect on multipoles is given by the geometry of the surface A. It is interesting to note that the surface B, which is much shorter than A, is also relevant for high order multipoles; this surface determines the radial position of the pole of the inner layer.

Table 6.8: Multipole shift due to collar non nominalities of +0.1mm. The higher sources of field errors are marked in bold.

	A		B			C		D	
	shift	tilt	shift	tilt+	tilt -	shift	tilt	shift	tilt
Δb_3	0.31	**0.85**	-0.43	-0.40	-0.56	0.41	-0.10	0.55	-0.10
Δb_5	**-0.17**	0.01	0.06	**0.18**	**0.20**	-0.02	0.01	-0.10	0.04
Δb_7	0.05	0.01	0.05	-0.04	-0.02	-0.01	0.00	0.04	-0.02
Δb_2	**2.71**	1.29	-0.10	-0.45	-0.55	0.95	-0.22	**1.62**	-0.34
Δb_4	-0.31	0.33	**-0.35**	0.03	-0.04	0.07	-0.01	-0.10	0.07
Δa_2	**-3.92**	-1.34	-0.52	-0.41	0.10	1.04	-0.16	1.22	-0.13
Δa_4	**-0.93**	**-0.75**	0.22	0.30	**-0.60**	-0.10	0.04	-0.16	0.06
Δa_3	**-2.42**	-1.00	-0.34	0.20	0.19	0.08	0.01	-0.13	0.11
Δa_5	**-0.22**	**-0.40**	**0.28**	0.05	-0.08	-0.05	0.01	0.06	-0.03

6.4.2 Expected harmonics: evaluation and comparison with the measured ones

Multiplying the sensitivity matrix by the measured collar geometrical errors, the expected shift in the multipoles due to the actual shape of the collar can be reconstructed. We showed that the three dipoles manufacturers use three different procedures to assembly the collars and therefore the global effect on each field error

class has to be evaluated taking into account the assembly procedure. The expected field harmonics are evaluated for aperture 1.

- *Allowed harmonics:* the assembly procedures of Firm2 and 3 are equivalent and the expected values are

$$b_{2n+1,T1} = \frac{b_{2n+1,T1,A1} + b_{2n+1,T2,A1} + b_{2n+1,T1,A2} + b_{2n+1,T2,A2}}{2}$$

  i.e. an average effect between the two apertures is taken. For the expected values of the collared coils assembled at Firm1 we only sum the terms $b_{2n+1,T1,A1}$ and $b_{2n+1,T1,A2}$ (section 2) and therefore it is not necessary to divide by two.
- *Even normal harmonics*: the collar position S_{AU} is magnetically equivalent to S_{BL}, the collar position S_{AL} is magnetically equivalent to S_{BU}, and the effects produced by S_{AU} are opposite in sign to the ones produced when the collar is in the position S_{AL}. Therefore:
  - Collared coils assembled by Firms2 and Firm3:

$$b_{2n} = \frac{b_{2n,T1,A1} - b_{2n,T2,A1} + b_{2n,T1,A2} - b_{2n,T2,A2}}{2}$$

  - Collared coils assembled by Firm1:

$$b_{2n} = b_{2n,T1,A1} + b_{2n,T1,A2}$$

- *Even skew harmonics:* the same collar assembled in positions S_{AU} and S_{BL} gives zero contribution to these harmonics. Therefore:
  - Firm1 and Firm2 use the positions S_{AU} and S_{BD} thus giving a global zero effect.
  - Firm3 uses the position S_{AU} and S_{AL}: the effects are evaluated as

$$a_{2n} = \frac{a_{2n,T1,A1} - a_{2n,T2,A1} + a_{2n,T1,A2} - a_{2n,T2,A2}}{2}$$

- *Odd skew harmonics:* these multipoles are influenced by a rotational symmetry, and the conclusions are the same drawn for the even skew multipoles.
  - Firm1 and 2 have zero effect due to the assembly procedure.
  - In Firm3 the effect is evaluated according to

$$a_{2n+1} = \frac{a_{2n+1,T1,A1} - a_{2n+1,T2,A1} + a_{2n+1,T1,A2} - a_{2n+1,T2,A2}}{2}$$

The results of the calculation are showed in Figure 6.11 and in Table 6.9 and Table 6.10. We compare the measurements of the aperture 1 to the expected values evaluated as mentioned above. It can be concluded that:

- We have shown in the previous section that b_3, b_5, b_7… are not driven by the collar imperfections. The comparison of expected versus measured multipoles confirms this result: the expected contribution of the collars to the spread of b_3, b_5, b_7 is one third of what measured.

Moreover, the expected shift in the average multipoles between firms is negligible, not justifying the large measured differences in b_5 and b_7.

- For Firm3, where we have proven through correlations that b_2 and a_3 are strongly affected by the collars, a good agreement between measured and expected values both for the average and for the standard deviation is found.
- For the skew multipoles in Firm1 and Firm2 the assembly procedure guarantees no contribution from the collars, and therefore the observed spreads are due to other components.
- The only inconsistency found is that from the collar measurements we expect a much larger standard deviation of what measured for b_2 and b_4 in Firm1 and Firm2.

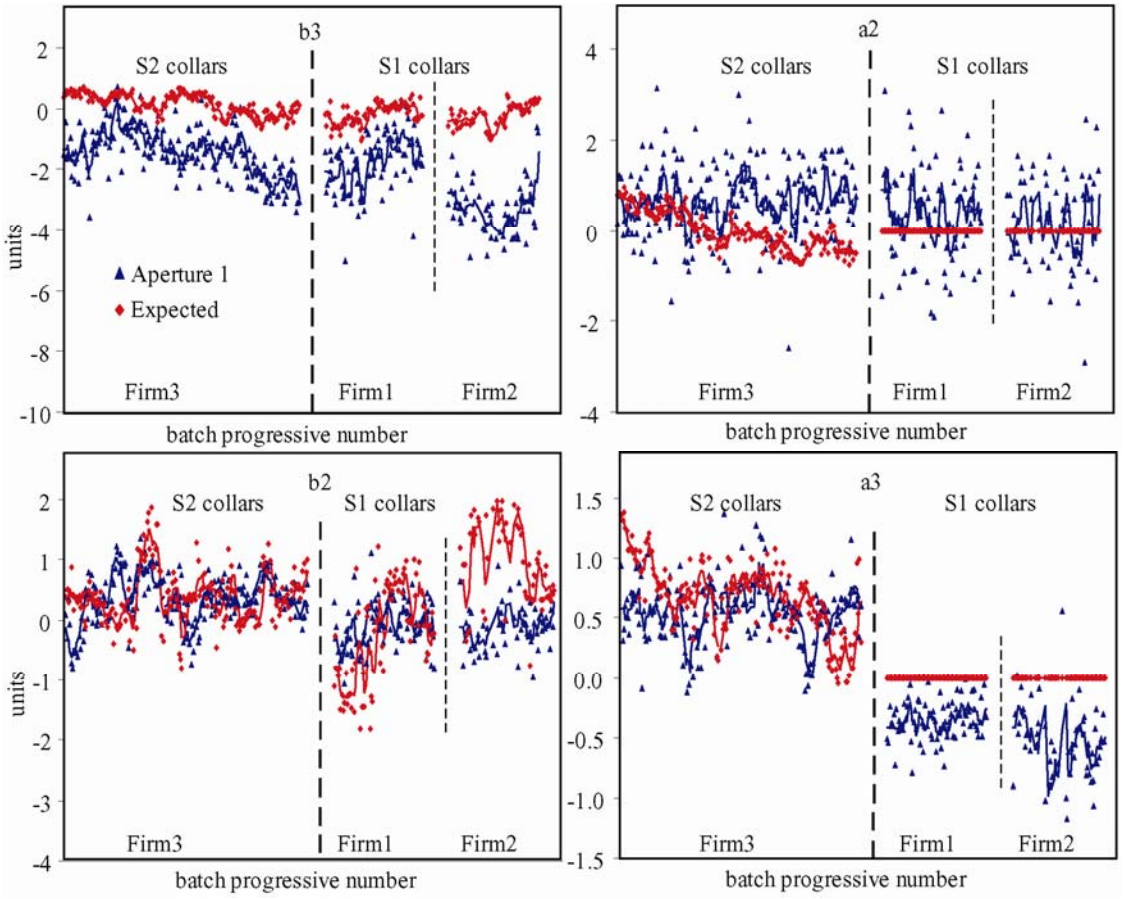

Figure 6.11: Expected and measured field harmonics, and moving averages (solid lines).

Table 6.9: Measured and expected average magnetic field harmonics.

Collar	Dipole		Δb_3	Δb_5	Δb_7	b_2	b_4	a_2	a_4	a_3	a_5
S_2	Firm3	meas	0.52	-0.26	0.06	**0.35**	**-0.05**	0.84	-0.12	**0.53**	0.19
		exp	0.16	-0.07	0.06	**0.39**	**0.03**	0.00	0.03	**0.67**	-0.01
S_1	Firm1	meas	0.39	0.71	0.13	-0.10	-0.09	0.15	0.02	-0.44	0.02
		exp	-0.17	0.00	0.01	-0.21	0.02	-	-	-	-
	Firm2	meas	-0.92	-0.45	-0.19	-0.13	-0.10	-0.29	0.40	-0.48	0.00
		exp	-0.19	-0.01	0.01	0.94	0.00	-	-	-	-

Table 6.10: Measured and expected standard deviation of magnetic field harmonics.

Collar	Dipole		b_3	b_5	b_7	b_2	b_4	a_2	a_4	a_3	a_5
S_2	Firm3	meas	0.85	0.20	0.07	**0.42**	**0.08**	0.67	0.24	**0.26**	0.09
		exp	0.34	0.05	0.02	**0.45**	**0.05**	0.44	0.10	**0.30**	0.06
S_1	Firm1	meas	0.83	0.32	0.07	0.41	0.08	1.00	0.26	0.22	0.07
		exp	0.33	0.08	0.03	0.83	0.14	-	-	-	-
	Firm2	meas	0.95	0.31	0.10	0.36	0.09	1.06	0.28	0.30	0.07
		exp	0.38	0.07	0.02	0.68	0.06	-	-	-	-

6.5 Conclusion

The main results of the analysis are:

- Collar dimensions: there are not significant differences in the geometry between the two collar suppliers. The values measured for the shifts are close or slightly above the tolerances, whereas the values measured for the tilts exhibit smaller standard deviations. The shifts of the collars type A1 of the supplier S_1 have a larger spreads with respect to the ones of the collars of S_2
- The collar shape is the driving mechanism of field harmonics only for b_2 and a_3 in Firm3, where collars of the supplier S_2 are used. Two independent observations support this fact: firstly, we have strong correlations between apertures of the same magnet as expected from the assembly procedure. Secondly, the expected values based on the measured dimension of the collars agree with magnetic measurements both for the average and for the standard deviation.
- For all the other cases the collar imperfections are not the driving mechanism of the field harmonics. In particular, we point out that the large systematic differences between dipole manufacturers observed for b_5 and b_7 cannot be due to the collars. Moreover, the spread due to the measured imperfections of the collars is only one third of the measured spread of the allowed field harmonics.
- The collar specifications and the collar suppliers have reached the difficult goal of minimizing the impact of collar geometry on the magnetic field harmonics.

References

[6.1] P. Fessia, D. Perini, S. Russenschuck, C. Völlinger, R. Vuillermet, C. Wyss, **"***Selection of the Cross-Section Design for the LHC Main Dipole"* IEEE Trans. Appl. Supercond **Vol. 10** (**2000**), 65-8 also **CERN-LHC-Project-Report-347**.

[6.2] P. Tropea, W. Scandale, E. Todesco, *"Influence of mechanical tolerances on field quality in the LHC main dipoles"*, IEEE Trans. Appl. Supercond. **Vol. 10** (**2000**) 73-6, also in **CERN LHC Project Report 351**.

[6.3] P. Ferracin, W. Scandale, E. Todesco, P. Tropea, *"A method to evaluate the field-shape multipoles induced by coil deformation"* ,1999 Particle Accelerator Conference, New York, USA, 1999, also in **CERN LHC Project Report 287**.

[6.4] B. Bellesia, V. Remondino, W. Scandale, E. Todesco, C. Völlinger, *"Correlations between Field Quality and Geometry of Components in the Collared Coils of the LHC Main Dipoles"*, IEEE Trans. Appl. Supercond. **Vol. 14** (**2003**) 219-222, , also as **CERN LHC Project Report 705**.

[6.5] F. Bertinelli, F. Fudanoki, T. Komori, G. Peiro, L. Rossi, "*Production of austenitic steel for the LHC superconducting magnets*", IEEE Trans. Appl. Supercond. **Vol. 16** (**2006**) 1773-6.

[6.6] *"LHC technical specification for the supply of 1158 cold masses of the superconducting dipole magnets for the LHC collider", **Annex: C1, G4*** – LHC-MB-C1-0006

[6.7] Private communication with project engineers of CERN – AT department – Magnet and Superconducting Group

[6.8] I. Vanenkov, F. Bertinelli, E. Boter-Rebollo, S. Berthollon-Vitte, D. Glaude, *"A correlation study between geometry of collared coils and normal quadrupole multipole in the main LHC dipoles"*, IEEE Trans. Appl. Supercond. **Vol. 16** (**2006**) 219-222.

[6.9] Private communication, F. Bertinelli – CERN/AT/CRI

Chapter 7

Random errors in the LHC dipoles

In previous work [7.1]-[7.3] estimates of the geometric random errors are usually based on estimating field perturbations induced by a random displacement of the coil blocks with a spread of ~50 μm. Here, we developed a Monte Carlo code aiming at giving a more precise calculation of this value.

From the LHC dipole field quality measurements, the random components of the field harmonics show a saw-tooth pattern, i.e. that for the odd multipoles, the normal components are always larger than the skew ones of the same order, and vice versa for the even ones; this feature has suggested that the random displacements are not equally spread along all the possible geometries and symmetries. Hence, differently from [7.3] - [7.6] the Monte Carlo simulations have been worked out to separately excite the four classes of field harmonics. Thus providing four parameters (one for each class of multipole) that better model the random field components.

In section 1 we present the sets of data we deal with: the *r.m.s.* of each LHC dipole integrated multipole, and all the values measured along the axis of each dipole. In section 2 numerical simulations are performed associating random displacement to the coil blocks; in section 3, a parameter, the coil positioning - defined as the standard deviation of the geometrical displacement associated to the blocks needed to reconstruct the field random errors - of each class of multipoles are computed. Finally, in section 4 the study is extended also the dipoles production of Tevatron [7.7], HERA [7.8], and RHIC [7.9] comparing them to the LHC one.

7.1 Available data and phenomenology

The magnetic field of the LHC main dipoles is measured along eighteen consecutive positions with a rotating coil to cover all the magnet length, and an integral value of the multipoles is built by computing an average over the positions, weighted with the main field component (see chapter 3). Having a set of magnets, one defines the random component as the standard deviation of the integral multipoles. The random component can be taken over all the production of magnets with the same design, or it can be split according to the different manufacturers to evaluate the influence of the production tooling and procedures on the field quality. In Table 7.1 the numbers of collared coils manufactured by the three magnet assemblers used in this analysis are given.

Table 7.1: Number of collared coil used in the study, split with respect to the dipole assembler.

All	Firm1	Firm2	Firm3
836	263	169	404

The magnetic harmonics, along the magnet length, feature random oscillations and usually for each magnet the average along its axis is recorded. It can be proven from chapter 3, that a current line at a radius r moved randomly from its nominal position of $\Delta r << r$, generates random multipoles that decay following the power law:

$$\sigma_{b_n}, \sigma_{a_n} \propto \left(\frac{R_{ref}}{r} \right)^n \qquad \text{Eq. 7.1}$$

where the R_{ref} is the reference radius, and usually taken equal to 2/3 of the inner radius of the magnet aperture. The random components present the same behavior; in Appendix A the analytical formulation for a simple dipole configuration is given.

Then when a set of magnets is taken into account each multipole presents a systematic component (the average of the averages of the magnets) and a random part (the *r.m.s.* of the magnet averages). In Table 7.2 and in Figure 7.1 the *r.m.s.* of the distribution of the average along the production are given. The *r.m.s.* are computed for the whole production and splitting the production among the three firms. For the theoretical curve only the slope has a meaning: actually the random component should follow a decay which is proportional to the ratio between the adopted reference radius and the inner radius of the aperture to the power of the multipole order - for LHC magnets the ratio R_{ref}/r_{in}=0.60 as shown in Eq. 7.1. The values are within the control limits given in Table 3.2.

Table 7.2: Measured standard deviations of the averages of the LHC collared coils.

multipole	All	Firm1	Firm2	Firm3
b_2	0.55	0.48	0.42	0.55
b_3	1.06	1.06	0.96	1.06
b_4	0.100	0.118	0.094	0.086
b_5	0.475	0.318	0.301	0.222
b_6	0.035	0.031	0.035	0.029
b_7	0.143	0.077	0.122	0.068
b_8	0.013	0.014	0.015	0.011
b_9	0.052	0.024	0.020	0.019
a_2	1.04	1.22	1.10	0.87
a_3	0.52	0.26	0.29	0.33
a_4	0.351	0.265	0.321	0.296
a_5	0.117	0.079	0.075	0.096
a_6	0.074	0.069	0.080	0.074
a_7	0.043	0.041	0.044	0.039
a_8	0.028	0.021	0.027	0.023
a_9	0.023	0.025	0.025	0.017

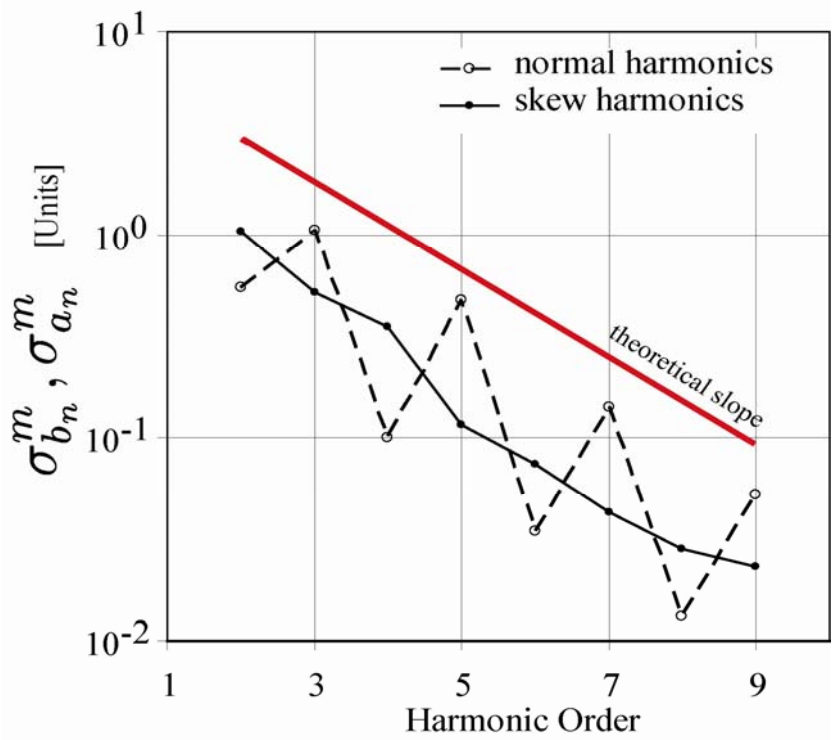

Figure 7.1: Measured standard deviations of the averages of the LHC collared coils (markers) and theoretical slope

The random fluctuations of the field harmonics measured along the magnet length have also been computed. In order to remove the effect of the different averages per each magnet the multipole average of each magnet is subtracted to the values of each position. Values are given in Table 7.3 and in Figure 7.2.

Table 7.3: Measured standard deviations of the positions of the LHC collared coil.

Multipole	All	Firm1	Firm2	Firm3
b_2	0.49	0.59	0.51	0.41
b_3	0.78	0.78	0.61	0.85
b_4	0.134	0.155	0.130	0.121
b_5	0.198	0.171	0.168	0.226
b_6	0.058	0.066	0.059	0.052
b_7	0.056	0.055	0.050	0.059
b_8	0.022	0.025	0.024	0.019
b_9	0.015	0.016	0.013	0.014
a_2	0.69	0.79	0.63	0.65
a_3	0.32	0.34	0.35	0.29
a_4	0.28	0.30	0.29	0.26
a_5	0.14	0.14	0.14	0.14
a_6	0.071	0.078	0.073	0.065
a_7	0.049	0.049	0.052	0.048
a_8	0.024	0.026	0.024	0.023
a_9	0.019	0.018	0.021	0.018

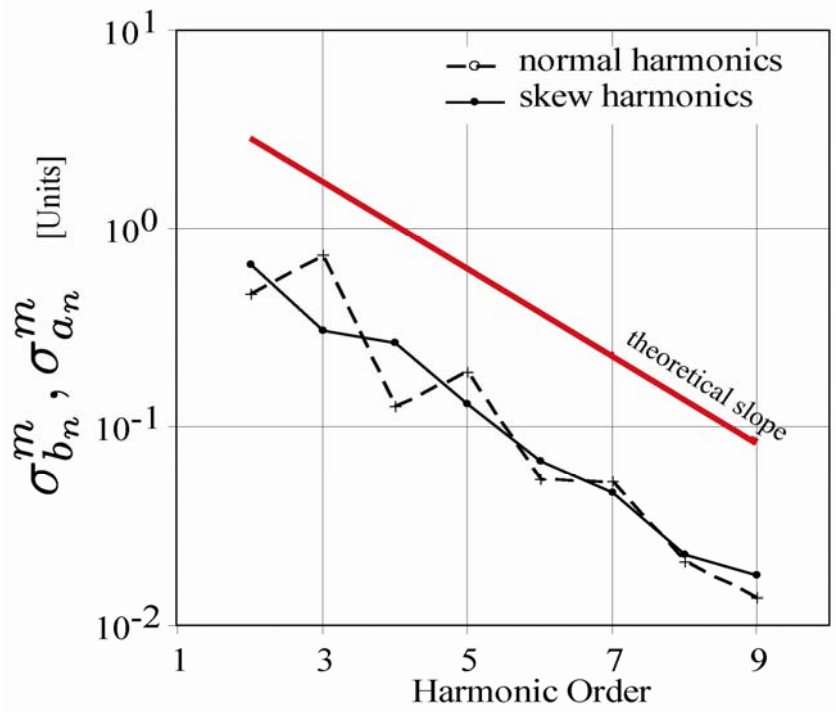

Figure 7.2: Measured standard deviations positions of the LHC collared coils (markers) and theoretical slope.

The main points of the analysis are the following:

- a saw-tooth pattern of the normal random components is evident: the standard deviations of the odd normal (b_3, b_5, b_7...) and of the even normal (b_2, b_4, b_6 ...) decay with the same theoretical slope but independently but different intercepts
- the decays of the skew multipoles has no saw-tooth and their slopes follows the theoretical values, their intercepts being in between the odd and the even normal
- the standard deviation of b_5, b_7 and b_9 are around 50% less if computed separately for each firm.
- The width of the saw tooth for the averages is two times wider with respect to the case of the positions.

7.2 Generation of field random errors

The random parts of the field harmonics measured along the magnet production can be analyzed through Monte Carlo methods. The approach is to interpret the field random components as a random variation of the block positions; here the conductor blocks are assumed as a rigid structure which can be shifted along the three degrees of freedom in the magnet cross section plane: radially, azimuthally and tilting around the center-of-gravity (see Figure 7.3).

When not specified differently, the blocks are shifted by two orthogonal vectors (in the cross section plane) whose amplitudes belong to a Gaussian distribution of $d/\sqrt{3}$, and they are also tilted around the baricentre by an angle such as the block corner movements are a Gaussian distribution with the standard deviation equal to $d/\sqrt{3}$. In this way the total random displacement of each block is d.

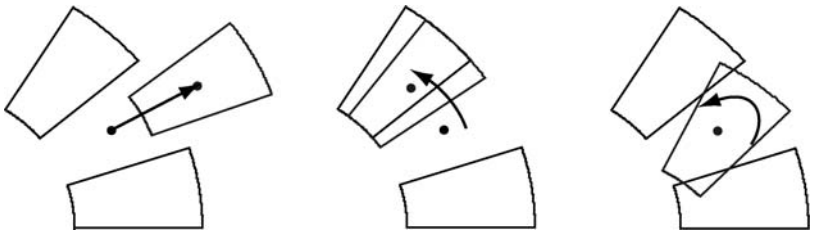

Figure 7.3: Block displacements used in the simulation.

For each run of the simulation the code generates 1000 apertures with the blocks shifted randomly, multipoles are computed and their standard deviation is evaluated. The associated maximum statistical error of the evaluation of the standard deviation of the distribution of the multipoles is 3%. The simulations for a given amplitude d provide a set of random components $\sigma_{bn}^{s}(d)$ and $\sigma_{an}^{s}(d)$ (the label s denoting "simulation").

A sensitivity study of the method is performed in order

- To evaluate the effect on the random components of the three movements: radial, azimuthal and tilt.
- To calculate the influence of each coil block
- To estimate the difference when block of single cables are moved

In all cases the geometric random displacements belong to Gaussian distribution with standard deviations of d=0.1 mm.

7.2.1 Random field errors generated by coil block displacements

Here, the random parts of the magnetic field harmonics induced by the three movements of the blocks are considered separately. The radial, azimuthal and tilted displacements are taken as a normal distributions with standard deviations equal to d=0.1 mm. For the block rotations, the angular distributions of the displacements are chosen such as the block baricentre (in the case of an azimuthal movement) and the block corners (in the case of a tilt) belong to Gaussian distributions with the standard deviations equal to d.

The results are shown in Figure 7.4. The radial and azimuthal movements give rise to same effect on the random harmonics; moreover they have an orthogonal behavior as it is also analytically evaluated in the Appendix A for simplified cross-sections. The effects of the tilting are smaller but not negligible, their value being about 10% of the radial and azimuthal. The decay of the standard deviations as a function of the multipole order is equal in the three cases.

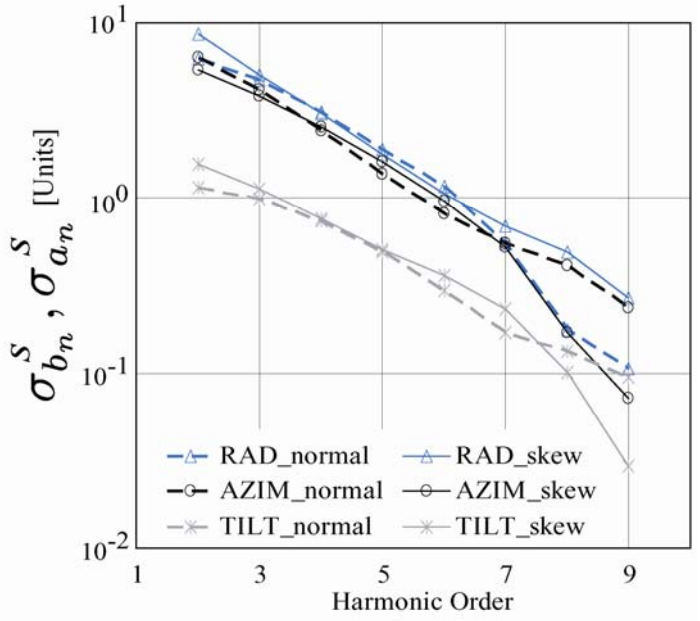

Figure 7.4: Random part of the magnetic field harmonics induced by the three allowed displacements of the coil blocks: radial, azimuthal and tilt. All the given displacements belong to normal distributions with standard deviations equal to d=0.1 mm.

7.2.2 Random field errors generated by single block

We now consider that each block of the dipole cross section is shifted separately. The three allowed displacement distributions, radial, azimuthal and tilt, given to the blocks belong to Gaussian distributions with the standard deviations equal to d=0.1/√3 mm, giving a total random displacement of 0.1 mm.

As shown in Figure 7.5, the decay of the randoms when the outer layer blocks are moved is faster that the one induced by movements of the inner layer blocks. This is due to dependence of the σ_{bn} on the term $1/(r)^n$: the larger r the faster is the decay. Eventually, it can be stated that blocks of the outer layer have a smaller influence on high order harmonics. Moreover the differences of the absolute values of the random harmonics due to the movements of the inner layer blocks are due to the different number of cables contained in each block. For instance the 3rd and 4th blocks contain the same number of cables and induce the same random field errors. Therefore the only dependence for the field errors is the radial position and the number of cable that each block contains whilst the azimuthal position is not relevant.

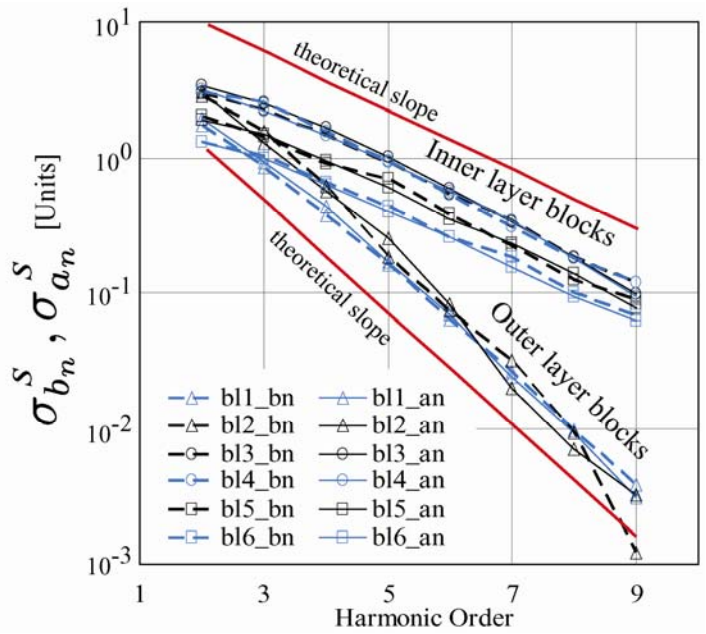

Figure 7.5: Random field harmonics induced by random geometrical displacements along the three degree of freedom of the 6 blocks of the LHC main dipole aperture. The total random displacement of each block is d=0.1 mm. Blocks 1-2 outer layer, blocks 3-6 inner layer.

7.2.3 Random field errors generated by block and cable displacements

A Monte Carlo simulation has been performed by moving randomly the single cables. The results are showed in Figure 7.6 and in Table 7.4 where a comparison with the random movement of blocks is carried out. The logarithmic decays in the two simulations are similar, but, since, the decay of higher order multipoles is dependent on the azimuthal thickness of the blocks [7.6], the decay is slower. The absolute values of the standard deviations due to the block motions are around of factor of two larger than the ones evaluated for the cable displacements.

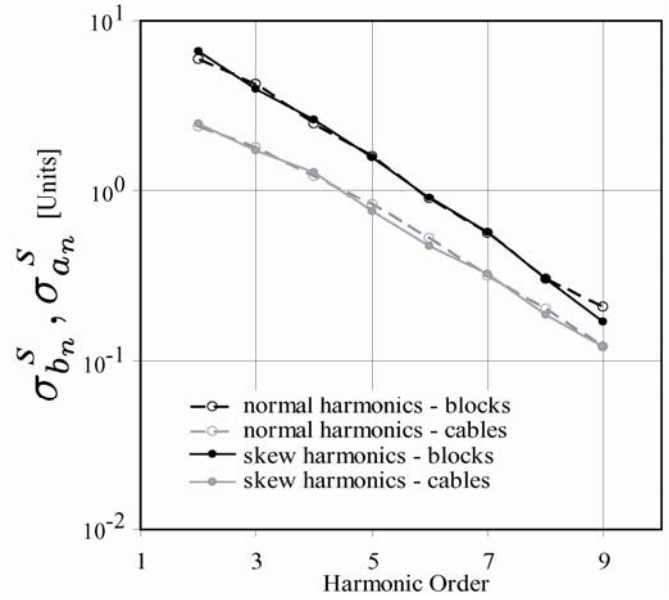

Figure 7.6: Random part of the magnetic field harmonics induced by blocks and cables random movements gaussianly distributed with a standard deviation d=0.1mm.

Table 7.4: Random part of the magnetic field harmonics induced by blocks and cable random movements gaussianly distributed with a standard deviation d=0.1mm.

	blocks	cables
b_2	5.957	2.386
b_3	4.251	1.793
b_4	2.487	1.220
b_5	1.593	0.822
b_6	0.889	0.517
b_7	0.552	0.313
b_8	0.300	0.199
b_9	0.206	0.120
a_2	6.637	2.484
a_3	3.961	1.711
a_4	2.596	1.276
a_5	1.571	0.744
a_6	0.901	0.465
a_7	0.565	0.318
a_8	0.300	0.185
a_9	0.168	0.120

7.2.4 Asymmetries of normal and skew random components

The same values for the standard deviation of the normal and skew multipoles of the same order are foreseen from the analytical formulation [7.6]. On the other hand, when the calculation is performed on the blocks, this symmetry has not been found, showing differences up to 10-15% for lower order harmonics, see Table 7.4. For instance, in the LHC dipole case one finds that the random a_2 is 10% larger that b_2, whereas the random b_3 is 8% larger than a_3 (the difference are reliable since are larger than the maximum statistical error associated to the simulation – 3%). This asymmetry is due to the block tilt: if in the Monte Carlo only azimuthal and radial displacements are implemented a perfect symmetry between normal and skew is recovered. Moreover, in Appendix B it is shown that taking into a dipole configuration with radial blocks the results are observed, because the block layout breaks the azimuthal homogeneity of the coil. The asymmetry is qualitatively similar to what observed in movements. Indeed the measured difference between normal and skew can be up to a factor of two, whereas simulations give 10-15% maxium.

7.3 Coil positioning definition and calculation

Estimates of the geometric random errors are usually based on estimating field perturbations induced by a random displacement of the coil blocks with a spread of ~50 μm *r.m.s.*. The developed Monte Carlo code aims to give a more precise calculation of this value.

First, we evaluate the amplitude needed to reconstruct all the classes of the multipole random components. Then we propose to associate different amplitudes to generate the random components of each class of multipoles in order to better fit the saw-tooth observed in the experimental data of Table 7.2 and Table 7.3.

The coil blocks are all randomly moved in order to excite all the harmonic classes at the same time. We evaluate the discrepancy - $\eta(d)$ - of the measured standard deviations - $\sigma_{bn}{}^{m}$ and $\sigma_{an}{}^{m}$ - with respect to the simulated - $\sigma_{bn}{}^{s}(d)$ and $\sigma_{an}{}^{s}(d)$; actually, since the discrepancy is evaluated taking into account the standard deviations of each order n and since the decay is a power law of the order (Eq. 7.1) we compared the logarithms of the standard deviation to not be driven only by the low orders:

$$\eta(d) = \sum_{n=2}^{N} \left[\log \sigma_{bn}^{m} - \log \sigma_{bn}^{s}(d)\right]^2 + \left[\log \sigma_{an}^{m} - \log \sigma_{an}^{s}(d)\right]^2 \qquad \text{Eq. 7.2}$$

where N is the highest order of harmonic considered in the analysis (for LHC N=9).

Since in the range of interest ($0.005<d<0.5$) $\sigma_{bn}{}^{s}(d)$ and $\sigma_{an}{}^{s}(d)$ are proportional to d, we can perform only one simulation for $d=d_s=0.1$ mm evaluating $\sigma_{bn}{}^{s}(d_s)$ and $\sigma_{an}{}^{s}(d_s)$ and therefore $\eta(d)$ can be re-formulated as:

$$\eta(d) = \sum_{n=2}^{N} \left[\log \sigma_{bn}^{m} - \log \frac{d\,\sigma_{bn}^{s}(d_s)}{d_s}\right]^2 + \left[\log \sigma_{an}^{m} - \log \frac{d\,\sigma_{an}^{s}(d_s)}{d_s}\right]^2 \qquad \text{Eq. 7.3}$$

minimizing $\eta(d)$:

$$\frac{\partial \eta}{\partial d} = 0 \qquad \text{Eq. 7.4}$$

the value d_0 – the "**coil positioning**" – is calculated:

$$d_0 = d_s 10\text{^}\left\{\frac{1}{2(N-1)} \sum_{n=2}^{N} \left[\log \frac{\sigma_{bn}^{m}}{\sigma_{bn}^{s}(d_s)} + \log \frac{\sigma_{an}^{m}}{\sigma_{an}^{s}(d_s)}\right]\right\} \qquad \text{Eq. 7.5}$$

For LHC dipoles one finds d_0=25 μm (Figure 7.7 and Table 7.5) which is, not far from the average tolerance adopted for the geometrical components of the collared coil. This can be taken as the indication of the good monitoring of the productions and tuning of the machineries. Actually according to this analysis, the smaller *r.m.s.* of the measured multipoles corresponds to a better positioning of the blocks. We define the uncertainties of the positioning as the maximum distance between the evaluated multipoles and the measured ones (see Eq. 7.5): 43% of the LHC dipoles.

$$\text{Error} = \frac{1}{2N}\left(\sum_{n=2}^{N} \frac{\sigma_{bn}^{m} - \sigma_{bn}^{s}(d_0)}{\sigma_{bn}^{m}} + \frac{\sigma_{an}^{m} - \sigma_{an}^{s}(d_0)}{\sigma_{an}^{m}}\right) \qquad \text{Eq. 7.6}$$

This large value is mainly due to the saw-tooth pattern of the measured random field components.

Table 7.5: Coil positioning and the associated error for the LHC main dipoles.

	d_0 [μm]	error [%]
LHC – main dipoles	25	43

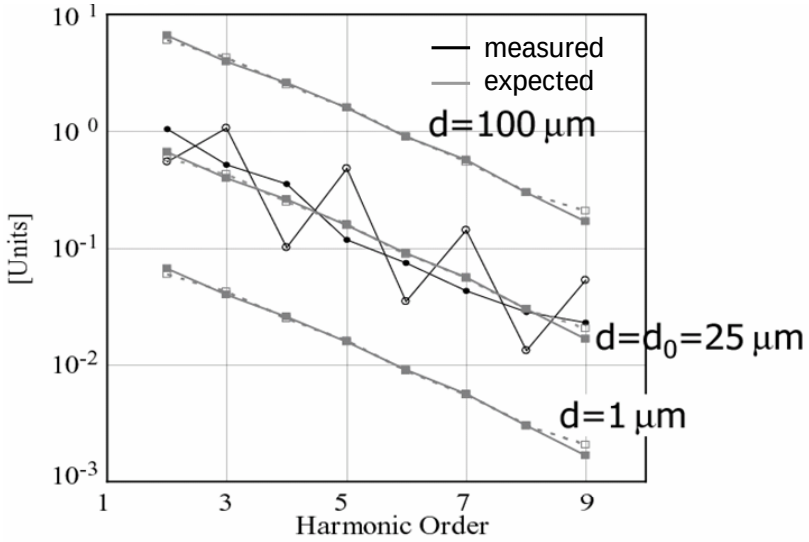

Figure 7.7: Coil positioning calculation of the LHC main dipole magnets.

To obtain the observed difference between normal and skew components, we split the random movements in the four dipole orthogonal families, associating different amplitude to each family, as suggested in [7.1] and [7.2]. We therefore define four η functions, two for the normal harmonics:

$$\eta_1(d) = \sum_{n=2}^{N} \left[\log \sigma^{m}_{b2n-1} - \log \sigma^{s}_{b2n-1}(d)\right]^2 \qquad \text{Eq. 7.7}$$

$$\eta_2(d) = \sum_{n=2}^{N} \left[\log \sigma^{m}_{b2n} - \log \sigma^{s}_{b2n}(d)\right]^2 \qquad \text{Eq. 7.8}$$

And two for the skew harmonics:

$$\eta_3(d) = \sum_{n=2}^{N} \left[\log \sigma^{m}_{a2n-1} - \log \sigma^{s}_{a2n-1}(d)\right]^2 \qquad \text{Eq. 7.9}$$

$$\eta_4(d) = \sum_{n=2}^{N} \left[\log \sigma^{m}_{a2n} - \log \sigma^{s}_{a2n}(d)\right]^2 \qquad \text{Eq. 7.10}$$

Minimizing, as before, Eq. 7.3 - 7.6, four coil positioning - d_1, d_2, d_3, d_4 – are computed, one for each dipole field harmonic class (Table 7.6). Optimizing the data with these four parameters the error between simulation and model drops to about 20%.

We find that for the LHC dipole production, the order of magnitude of geometric random components is compatible with a random movement of the blocks of ~50 μm r.m.s. for the odd normal multipoles, ~30 μm for the even skew, and 5 to 20 μm for the even normal and for the odd skew, see Table 7.6. Moreover if the LHC the data are split according to the dipole assembler, the random components of odd normal and skew are nearly 1/3 less, corresponding to smaller amplitudes.

Table 7.6: Coil positioning and the associated error for the LHC main dipoles. Reference measurements are the random of the averages.

	d_1 [μm] b_{2n+1}	d_2 [μm] b_{2n}	d_3 [μm] a_{2n+1}	d_4 [μm] a_{2n}	error [%]
LHC	54	12	18	26	25
LHC – Firm1	38	10	12	22	19
LHC – Firm2	42	8	12	24	13
LHC – Firm3	32	10	14	22	17

The same study is performed on the measurements of the random components along the magnet axis. The results are given in Table 7.7. The coil positioning considering the total production are equal to the ones evaluated for each firm. This is a consequence of the results given in the data analysis of section 7.1, the three distributions of the positions are more homogeneous is compared with the ones of the averages.

With respect to Table 7.6 the d_1 values (relative to the odd normal) are 50% smaller, whereas d_2 values (relative to the even normal) are 50% larger. This is due to the reduction of the width of the saw-tooth of the normal field harmonics. This unexplained feature corresponds to the reduction of the amplitude of the saw tooth as described in section 1. On the other hand the coil positioning of the a_{2n+1} and a_{2n} are only slightly smaller than what found in Table 7.6.

Table 7.7: Coil positioning and the associated error for the LHC main dipoles. Reference measurements are the random of the positions.

	d_1 [μm] b_{2n+1}	d_2 [μm] b_{2n}	d_3 [μm] a_{2n+1}	d_4 [μm] a_{2n}	error [%]
LHC	20	17	14	21	26
LHC – Firm1	19	17	13	21	20
LHC – Firm2	16	15	14	21	19
LHC – Firm3	21	13	13	20	21

7.4 Comparison to Tevatron, HERA, RHIC dipoles productions

In this section the random components of the measured field errors of the main dipoles in operating accelerators, namely Tevatron, HERA and RHIC, are analyzed (see Table 7.8). The aim is to compare these dipole productions to the LHC. The measured standard deviations of the integral field harmonics are shown Table 7.9 and in Figure 7.8 - Figure 7.10 where are also sketched the cross sections and the theoretical decay of the random components evaluated as $(R_{ref}/r_i)^n$.

Table 7.8: Parameters of the analyzed dipoles

	Number	Aperture radius [mm]	coil width [mm]	Layers	Blocks	R_{ref}[mm]	R_{ref}/r_i
Tevatron	774	38.1	16.3	2	2	25.4	0.666
HERA	416	37.5	21.2	2	4	25	0.666
RHIC	296	40.0	10.06	1	4	25	0.625

The following remarks can be made:

- the random components follow the thoretical decay law for all machines considered but saturate at 0.3 units for Tevatron and at 0.1 units for HERA. This is probably given by the precision of the measurement system. Therefore, we used Tevatron data up to order 6, HERA up to order 7 and RHIC up to order 8.
- In RHIC and HERA cases one observes a saw-tooth pattern, where the standard deviation of the odd normal is larger than the odd skew of the same order, and vice-versa for the even. This is a first difference with respect to the LHC, which does show a saw-tooth only for the normal components.

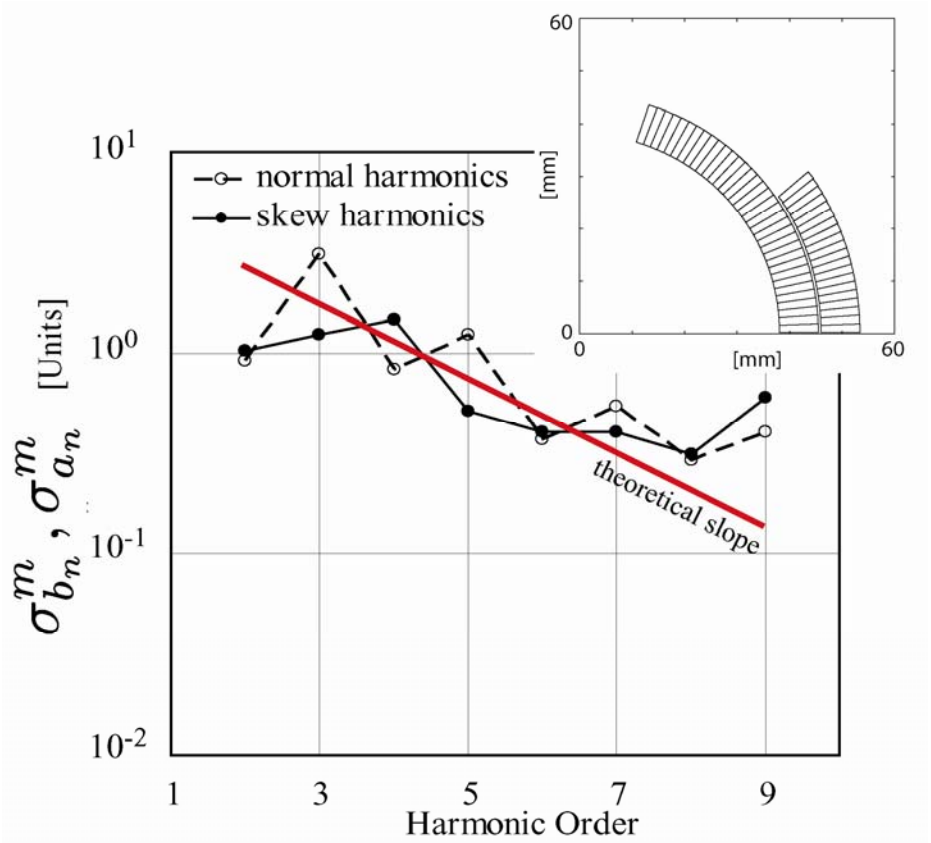

Figure 7.8: Random components measured in the Tevatron dipoles. The red line is the ideal slope: R_{ref}/r_i

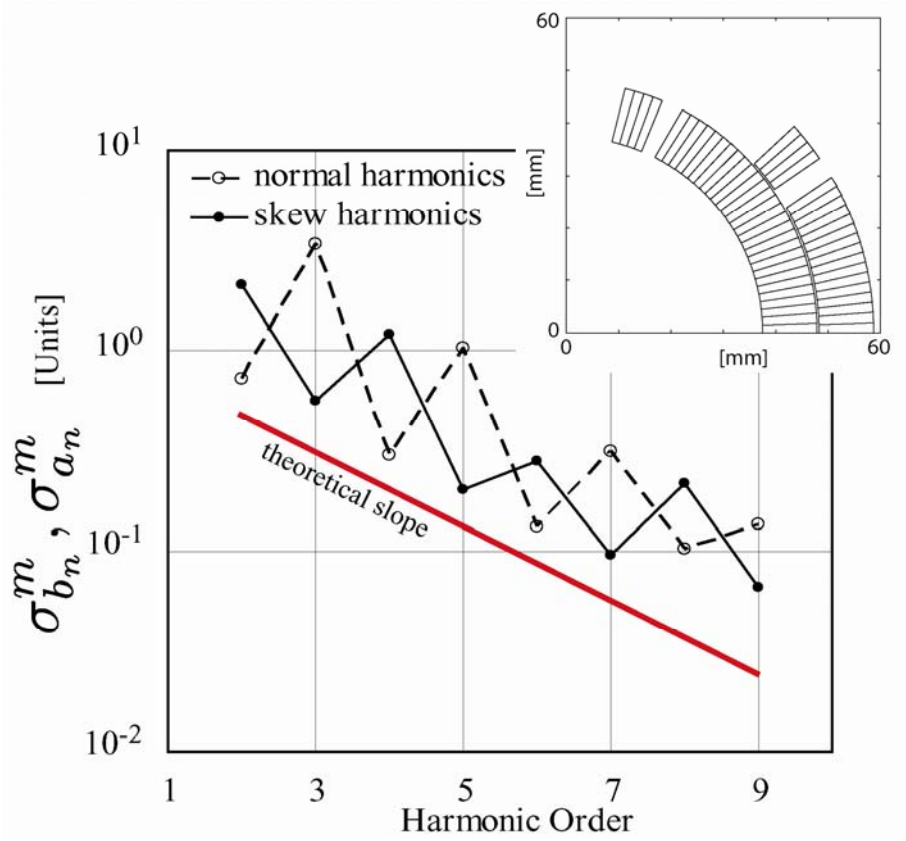

Figure 7.9: Random components measured in the HERA dipoles. The red line is the ideal slope: R_{ref}/r_i

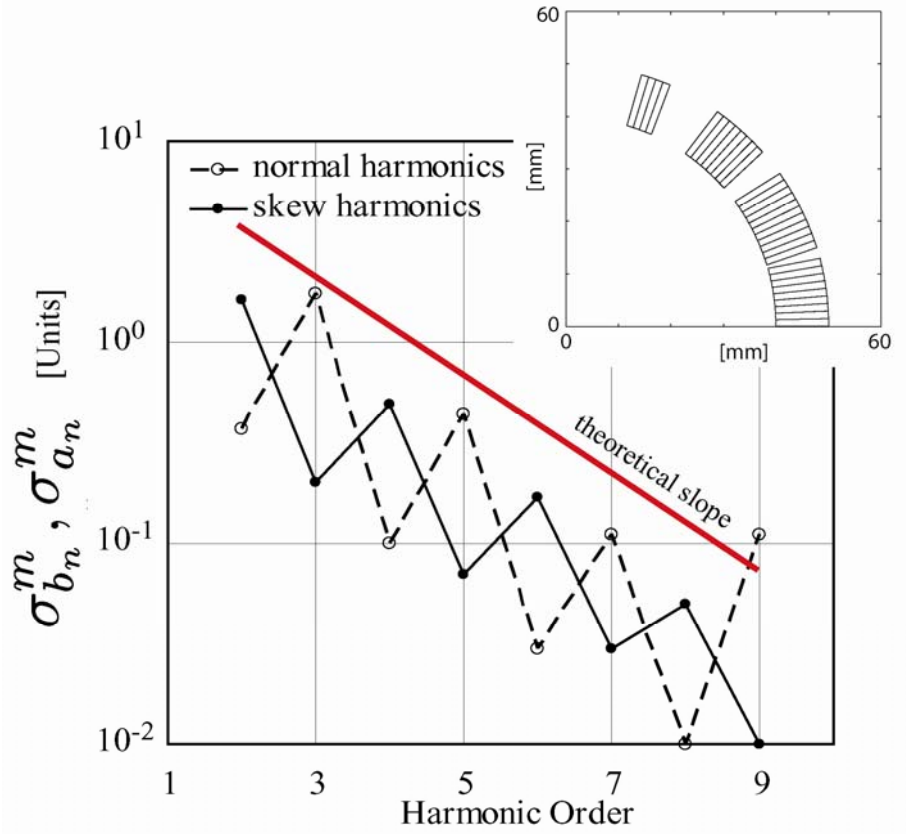

Figure 7.10: Random components measured in the RHIC dipoles. The red line is the ideal slope: R_{ref}/r_i

Table 7.9: Random components measured in the Tevatron, HERA and RHIC dipoles

	Tevatron	HERA	RHIC
b_2	0.92	0.73	0.37
b_3	3.08	3.42	1.74
b_4	0.830	0.300	0.100
b_5	1.230	1.037	0.440
b_6	0.370	0.133	0.030
b_7	0.540	0.313	0.110
b_8	0.290	0.102	0.010
b_9	0.400	0.136	0.110
a_2	1.03	2.14	1.62
a_3	1.23	0.56	0.20
a_4	1.460	1.210	0.490
a_5	0.510	0.202	0.070
a_6	0.400	0.279	0.170
a_7	0.400	0.095	0.030
a_8	0.310	0.217	0.050
a_9	0.600	0.066	0.010

Following the algorithm adopted for the LHC magnets production, the coil positioning of Tevatron, HERA and RHIC dipoles are evaluated first for the whole field quality and then differentiating the four classes of harmonics. In Table 7.10 we give d_0 for the dipoles of the three accelerators, together with the average relative error and in Table 7.11 the values of d_1-d_4 for the four harmonic families. Recalling that smaller values of coil positioning corresponds to an improvement in the precision in positioning the blocks:

- There is a clear pattern along the time scale. The eldest production (Tevatron, 1985) has the higher values.
- The RHIC dipole (production completed in 2001), whose lay-out is a single layer with a thin cable width (10 mm), assembled by the same firm, has reached the smallest coil positioning (16 μm).
- The LHC case, notwithstanding the more complicated 2-layer structure, with a 30 mm cable width, and three different assemblers, corresponds to amplitudes which are only 50% larger than RHIC (25 μm).
- The technological improvement along the time is well underline by at the values of b_{2n} and a_{2n+1} : the RHIC-LHC values (~10 μm) have about one order of magnitude less with respect the Tevatron ones (70 μm). The low values of the coil positioning of these two classes of multipoles underline a stable reliable production of the aperture poles since the two classes of harmonics are related to a respect of a Left-Right symmetry.

Table 7.10: Coil positioning and the associated error for the four considered dipole production (in brackets the year of production completion).

	d_0 [μm]	error [%]
Tevatron (1980)	65	35
HERA (1990)	41	40
RHIC (1997)	16	63
LHC (2006)	25	43

Table 7.11: Coil positioning and the associated error for the four considered dipole production (in brackets the year of production completion).

	d_1 [μm] b_{2n+1}	d_2 [μm] b_{2n}	d_3 [μm] a_{2n+1}	d_4 [μm] a_{2n}	error [%]
Tevatron (1985)	128	52	70	52	30
HERA (1990)	122	20	24	58	25
RHIC (2001)	52	6	8	32	30
LHC (2006)	54	12	18	26	25

7.5 Conclusion

Summarizing, the main results of the chapter are:

- The random parts of the field harmonics of the LHC main dipole follow the expected logarithmic decay, i.e. $(\sigma_{bn}, \sigma_{an}) \propto (R_{ref}/r)^n$ where r is the aperture radius.
- A parameter, the **coil positioning** - d_0 -, is introduced to evaluating the degree of precision for block positioning inside the magnets through the magnetic measurements.
- For the LHC dipoles, the measured random components agree with simulation results based on a d_0 =25 μm with an average error of 50%.
- For LHC dipoles, the random parts of normal harmonics show a saw tooth in a semi-logarithm plot. It has been found that the measurement of the random components of the dipole production of Tevatron, HERA and RHIC feature a similar pattern.
- The coil positioning of the Tevatron dipoles has the higher value of the coil positioning (65 μm) whilst the more recent productions (LHC and RHIC) have the lowest (52 - 54 μm).
- In order to better estimate the field errors the four classes of harmonics are separately considered and four coil positioning are calculated. For RHIC and LHC dipole production the order of magnitude of geometric random components is compatible with a random movement of the blocks of ~50 μm r.m.s. for the odd normal multipoles, ~30 μm for the even skew, and 5 to 20 μm for the even normal and for the odd skew. Such parameters allow estimating the random geometric errors with an average error of ~20%.

References

[7.1] J. Herrera et al, "*Random errors in the magnetic field coefficients of superconducting magnets*", IEEE Trans. Appl. Supercond., **Vol. NS-32**, No.5 (**1985**) 3689-3691.

[7.2] J. Herrera et al, "*Random Errors in the Magnetic Field Coefficients of Superconducting Quadrupole Magnets*" IEEE Trans. Nuclear Science (**1987**) pp 1477-1479

[7.3] R. Gupta, Part. Accel. **Vol 55** (**1996**) 129-39.

[7.4] P. Ferracin et al, "*Modeling of random geometric errors in superconducting magnets with application to the CERN Large Hadron Collider*", Physiscal Review Special Topics – Accelerators and Beams, **Vol. 3** (**2000**) 122403.

[7.5] W. Scandale, E. Todesco; R. Wolf, "*Random errors induced by the superconducting windings in the LHC dipoles*", IEEE Trans. Appl. Supercond., **Vol. 10**, Issue 1, (**2000**),93 - 97.

[7.6] R. Wolf, "*Analytical calculation of field errors due to small and random coil motion in cosine-theta type accelerator magnets*", LHC Internal Note

[7.7] P. Bauer et al, "*Tevatron magnetic Models Geometric and Hysteretic Multipoles in the Tevatron Dipole*" **Fermilab Internal Note TD-02-040** (**2004**).

[7.8] B.H. Wiik, "*Design and Status of the HERA Superconducting Magnets*", Progress in high Temperature Superconductivity, **Vol 8**, Ed. C.G. Burnham, R.D. Kane, World Scientific, World Congress on Superconductivity, (**1988**).

[7.9] P. Wanderer et al, "*The RHIC magnet system*", Nuclear Instruments and Methods in Physics Research, **A 499** (**2003**) pp. 280-315.

[7.10] E. Todesco et al, "*Trends in field quality along the production of the LHC dipoles and differences among manufacturers*", IEEE Trans. Appl. Supercond. **Vol. 16** (**2006**).

[7.11] K.-H. Mess, P. Schmuser, S. Wolff, "*Superconducting accelerator magnets*", Word Scientific Publishing, (**1996**)

Chapter 8

Collared coil inter-turn short-circuit: localization with magnetic measurement

The active part of the LHC dipole is the collared coil, i.e. the superconducting coils clamped in the stainless steel collars. The assembly of the coils in the collars takes place under the collaring press. At each applied load of the press, cable insulation tests are performed to check the electrical integrity of the coil. Since December 2003, a few cases of electrical shorts during collaring have been detected. In some of them the short disappeared after the disassembly of the coil, making impossible its localization. For this reason, following the experience given in [8.1] and [8.2], the use of the warm magnetic measurements performed on the collared coils has been proposed [8.3] to locate the shorts during the collaring procedure using its strong signature on the magnetic field harmonics.

In this chapter, we present a method to localize the short circuits by means of the magnetic field measurement at room temperature. The localization goes through the following steps, identifying:

- the aperture and pole
- the longitudinal position,
- the radial position in the transverse cross-section,
- the cables.

Before the development of this method when a short circuit was detected with the coil resistive measurement the cold mass assembler could only identify the affected pole. Without a finer localization the indetermination of the position was the total length of the coil (two times 15 m), which made improbable the repair. The method lowers the indetermination to the length of the magnetic measurement mole (0.75 m), and it can also distinguish between inner or outer layer, making possible the precise localization and reparation of the damage. For these reason, since the very first time that the method was applied, the three cold mass assemblers adopted it as an essential tool to rescue the faulty collared coil with considerable money and time savings.

In sections 2, 3 and 4 method is applied in detail to three cases, to underline the qualities but also the limits. An overview of all the analyzed cases is reported in section 5.

8.1 The method

Magnetic measurements at room temperature give a deep insight on the distribution of the current lines. For this reason, when a short circuit occurs it produces an anomaly in the magnetic field whose signature can be used to detect the short location. A standard warm magnetic measurement is performed on both apertures of the collared coil and the measurement of the aperture without the short is used as a reference.
The localization of a short circuit in a collared coil goes through the following steps:

- Computation of the field anomaly
- Identification of the aperture and the pole
- Localization of the longitudinal and radial position
- Identification of the cables inside the coil, the "short configuration".

8.1.1 Field anomaly identification

The main issue for the method is the comparison of the magnetic measurement of the faulty aperture with a good reference so that subtracting the reference from the measurement one obtains the field anomaly. This procedure is important for the allowed multipoles, which always have a systematic component, and for measurements carried out under the collaring press, which induces a strong magnetic perturbation on normal multipoles.

Normally, the short circuits are detected when the collared coil is under the collaring press and when the load is released the defect disappears. Therefore the magnetic measurement has to be performed when the collared coil is still under the press. Since the measured magnetic field is strongly influenced by the iron of the press a reference aperture has to be measured under the press in order to single out the defect. Normally the reference and the defective aperture belong to the same magnet. In order to face difficulties in measuring the sane aperture a special magnetic measurement of a collared coil was performed under the press having always a reference measurement.

In practice if the short is detected under the collaring press both aperture will be measured and the sane one is used as reference; if the short appear under the collaring press but, for any reason, the sane aperture can not be measured the mentioned reference aperture measured at the beginning is used; if the short is detected out of the press the collared coil goes through a standard magnetic measurement and, still, the sane aperture is used as the reference. There was a case (see section 3) of a collared coil in which the short circuit appeared after a first successful magnetic measurement (probably due to a bad handling): the magnet was then re-measured with the short. In that case the reference and the faulty aperture were the same.

The field anomaly is then compared to the control limits of the production which have been set for each multipole at ±3.5 standard deviation of the distributions of the collared coils that are considered as "normal" [8.4]. The comparison to the control limit allows to judge if a field anomaly is relevant or not. We will show that electrical shorts, in the inner layer, give very strong effects on multipoles that are well beyond the control limits of the production. This makes the method to detect short very

reliable. On the other hand, if the shorts are located in the outer layer the signature on the field quality is much lower (see section 4) giving some indetermination in the localization.

To analyze the problem we can use the simplified aperture model with three cable turns pole (see Figure 8.1). Let us consider a short circuit in a given longitudinal position along the magnet axis, where the current by-passes an entire turn, as shown by the dashed line in Figure 8.1a. A coil cross section taken between the short and the connection side features a current distribution with a left-right asymmetry (see Figure 8.1b, were the crossed cables are the ones that do not carry current). On the other hand, a coil cross-section taken between the short and the non connection side has a left-right current symmetry (see Figure 8.1c). This gives a tool to longitudinally locate the short through magnetic measurements:

- If anomalies are seen in all the four families of multipoles, the short is between this location and the non connection side;
- If anomalies are seen in odd normal and even skew multipoles only, the short is between this location and the connection side.

Therefore, looking at the pattern of the even normal and odd skew harmonics along the aperture, we can locate the short in the magnetic measuring position where the anomaly in these multipoles falls to zero. We also have two extreme cases, i.e., when the short is located in one of the coil ends:

- If the even normal and odd skew field harmonics show no anomaly all along the axis, the short will be located in the connection side end.
- If the even normal and odd skew field harmonics show anomalies all along the axis, the short will be located in the non connection side end.

The indetermination in the longitudinal localization is given by the length of the measuring position: 534 mm in the ends and 750 in the straight part. A shorter mole of 125 mm is available to better locate the short in the longitudinal coordinate [8.5].

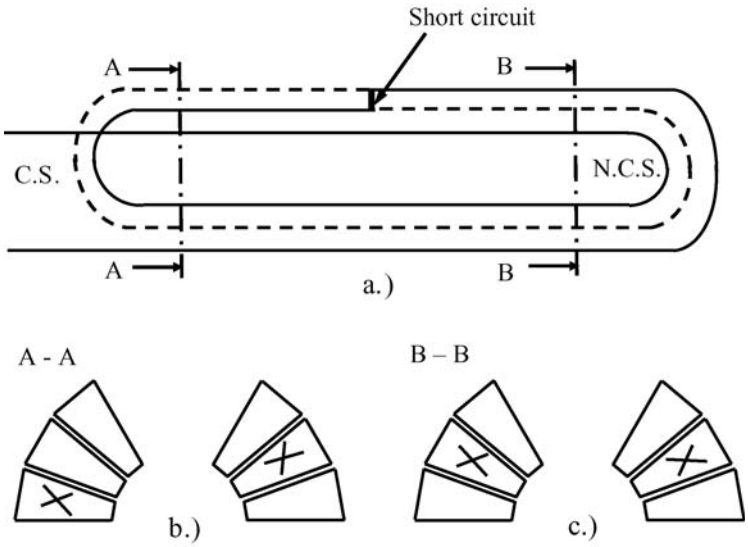

Figure 8.1: a.) Simplified model of a layer with three cable turns; the dashed line represent the turn bypassed by the current. b.-c.) Cross section of the coil respectively toward the connection side and the non connection side with respect to the short; the crosses inside the cables indicate that no current is flowing inside.

8.1.2 Pole localization

An electrical short circuit occurs either in the upper or in the lower pole, and therefore it generates a strong up-down asymmetry. Let us take again the simple dipole cross section made of two poles of three cable turns each (Figure 8.2). With a short circuit placed somewhere in the coil length of the upper pole the ideal current pattern is lost: in two cables (one in the right and the other in the left side of the pole) the current is not flowing (crossed cables in Figure 8.2).

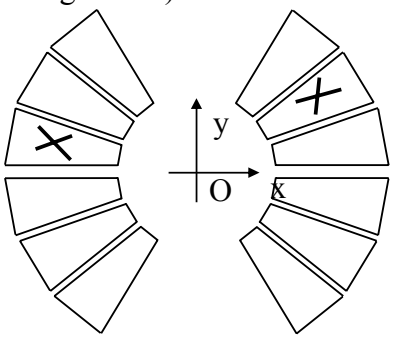

Figure 8.2: Schematic dipole cross section made of two poles of three cables turns each. The crossed cables do not transport current.

In the showed example all the symmetries are broken but the Up-Down asymmetry is stronger then the Left-Right. This is a general feature since we assume that the short can appear only among two contiguous cables; therefore the most affected classes of multipoles are the odd normal (b_3, b_5, b_7…) and the even skew (a_2, a_4, a_6…), and mainly a_2 and b_3.

Using a magnetic field model we can evaluate the effect of a short on two neighbour cables as 5-60 units of a_2, which are well beyond the control limit of 3.2 units (3.5s) established for the production. The smallest contribution (5 units) is given for shorts close to the mid plane. In this case there is a strong effect on b_3 (45 units) that can also be used to double check the analysis on a_2. The aperture that is featuring a field anomaly in a_2 has the electrical short.

To define the pole where the short is located one can computes the derivative in the center of the aperture of the magnetic field expansion with respect to "y" direction:

$$\left.\frac{\partial B_y}{\partial y}\right|_{x,y=0} = \left(- a_2 - 2b_3 \frac{y}{R_{ref}} - 2a_3 \frac{x}{R_{ref}} + o(x,y) \right)\Bigg|_{x,y=0} = -a_2 \qquad \text{Eq. 8.1}$$

the sign of a_2, according to the above equation, is the index which gives the information of the localization of the short:

- a positive a_2 means that the short is in the upper pole
- a negative a_2 means that the short is in the lower pole

8.1.3 Radial localization: layer identification

We now proceed to the identification of the position in the coil cross-section. A simple method can be used to detect if the short is in the inner or in the outer layer,

following the approach given in [8.6]. The used principle is that the field anomaly has a slow decay with the multipole order if the short is close to the aperture (inner layer), and a fast one if it is far (outer layer).

In Section 3.1.2 we have shown that the magnetic field featured by a single current line, placed in $z_c=x_c+iy_c$, can be expanded in a convergent series in the following way:

$$B(z) = B_{ref} 10^{-4} \sum_{n=1}^{\infty} c_n \left(\frac{z}{R_{ref}} \right)^{n-1} = B_{ref} 10^{-4} \sum_{n=1}^{\infty} (b_n + ia_n) \left(\frac{z}{R_{ref}} \right)^{n-1} \quad \text{Eq. 8.2}$$

and the coefficients are:

$$c_n = b_n + ia_n = -\frac{\mu_0 I}{2\pi B_1 R_{ref}^{n-1}} \frac{1}{z_c^n} \quad \text{Eq. 8.3}$$

where $B1$ is the main field magnitude at the reference radius R_{ref} and ,$z=x+iy$ is the complex coordinate. If we group all terms not depending on the multipole order n in a constant A, we obtain:

$$c_n = -A \left(\frac{R_{ref}}{z_c} \right)^n \quad \text{Eq. 8.4}$$

From Eq. 8.3, it can be seen that multipoles magnitude *decay* naturally, because the bigger is n, the smaller becomes the term $\left(\frac{R_{ref}}{z_c} \right)^n$, since R_{ref} is 17 mm and z_c is greater than 28 mm (the inner radius of the aperture of the LHC dipole). A small variation of the conductor position Δz_c leads to a variation in c_n as following:

$$\Delta c_n = \frac{nA\Delta z_c}{R_{ref}} \left(\frac{R_{ref}}{|z_c|} \right)^{n+1} \quad \text{Eq. 8.5}$$

computing the logarithm, we find:

$$\ln|\Delta c_n| = ln(n) + n\, ln\left(\frac{R_{ref}}{|z_c|} \right) + ln \frac{A|\Delta z_c|}{|z_c|} \quad \text{Eq. 8.6}$$

where $|z_c|$ is the conductor distance R_c from the aperture center. Expressing the complex coefficient with their real and imaginary parts (Δb_n,Δa_n) we can also write the relation:

$$f(n) \equiv ln\sqrt{(\Delta b_n)^2 + (\Delta a_n)^2} - ln\, n \approx n \ln \frac{R_{\text{ref}}}{R_c} + log\, A \qquad \text{Eq. 8.7}$$

and making a linear fit of the function $f(n)$:

$$f(n) \approx P + Qn \qquad \text{Eq. 8.8}$$

We can deduce R_c through the fitted slope Q (where Q>0):

$$R_c = R_{\text{ref}} \exp(Q) \qquad \text{Eq. 8.9}$$

Therefore, if R_s is between 28 and 43 mm, the short is in the inner layer, and if it is between 43 to 59 mm is in the outer layer. In Figure 8.3, as an example, the calculation of the $f(n)$ for two cases of a defect occurred in the inner layer and one in the outer layer are plotted. The different slopes discriminate the location of the defect.

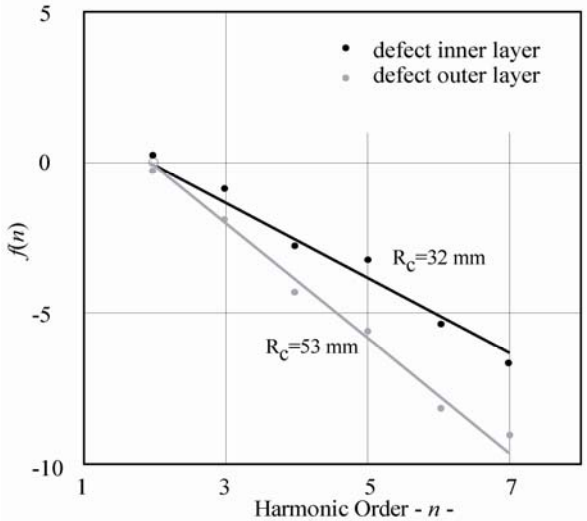

Figure 8.3: Decay of the function f(n) for a defect occurred in the inner layer and one occurred in the outer.

8.1.4 Cable localization

The convention used for numbering cables of the coil cross-section is shown in Figure 8.4, where the upper pole of a LHC aperture is sketched. For both left and right quadrants, the lowest cable of the first block is the cable number 1, then, moving azimuthally, the last cable of the outer layer is the number 25; cable number 26 is the lowest one of the inner layer and cable 40 is the upper one.

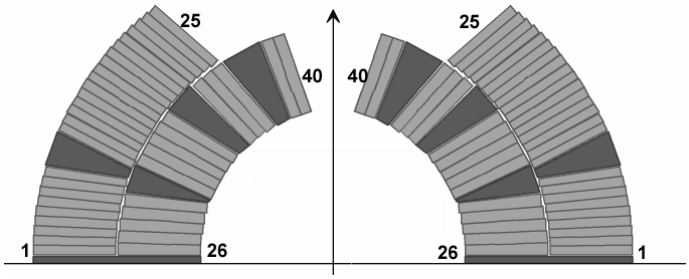

Figure 8.4: Cable numbering for half aperture of a LHC dipole.

As we already discussed, when a short occurs an entire turn of the coil is by-passed. This means that there are two cables in the coil cross-section, one on the left and one on the right part, that do not transport any current. From here on we assume that the short is located in the upper pole of the aperture (all the considerations are also valid for a short in the lower pole, taking care to apply the right symmetries: the effects on b_{2n+1} and a_{2n+1} are the same whilst they change sign for b_{2n} and a_{2n}). We have to define all the possible short circuits that can be detected in a pole. We assume that:

- Shorts between inner and outer layer are not allowed: an inter layer shim is interposed between the two layers.
- Short can appear only among two contiguous cables (it is physically improbable that two cable that do not share a surface can be short-circuited).

Let m be the cable of the right quadrant of the pole which does not transport any current: we denote by (k,l) the "short configuration", i.e. the couple of cables in the left and in the right part of the coil respectively where no current flows. Using the simplified models of the inner and outer layer of Figure 8.5 one can state that the possible shorts are:

- For the inner layer, we have $(m+1,m)$ between the short and the connection side, and (m,m) between the short and the non connection side
- For the outer layer we have $(m,m+1)$ for the cross-section between the short and the connection side, and $(m+1,m+1)$ for the short between the short and the non connection side.

According to our hypothesis, a few combinations are forbidden, such as, for instance, 9-10, as a wedge is placed between the 9^{th} and the 10^{th}.

The two cables that do not transport current create a different current distribution with respect to design; this causes a field anomaly. Anomalies given by all the possible short circuits have been evaluated using a magneto-static model of the cross section [8.6]. It is worth to point out that the field anomalies are strongly dependent on the angular positions (θ) of the cables that are "switched off": the effects on b_{2n+1} and on a_{2n+1} can be approximated with $cos[(2n+1)\theta]$ whilst the ones on b_{2n} and on a_{2n} with $sin[(2n)\theta]$.

The largest effects on field quality are observed for short circuits placed in the inner layer, the most affected harmonics being b_3 and a_2 ([-40;40] and [0;90]units respectively): this is why we use these two multipoles as proof of the presence of the short. By comparing the measured anomaly with the expected effects of all possible

shorts we identify the short location in the coil cross-section. Since we are using several multipoles, the solution is always unique.

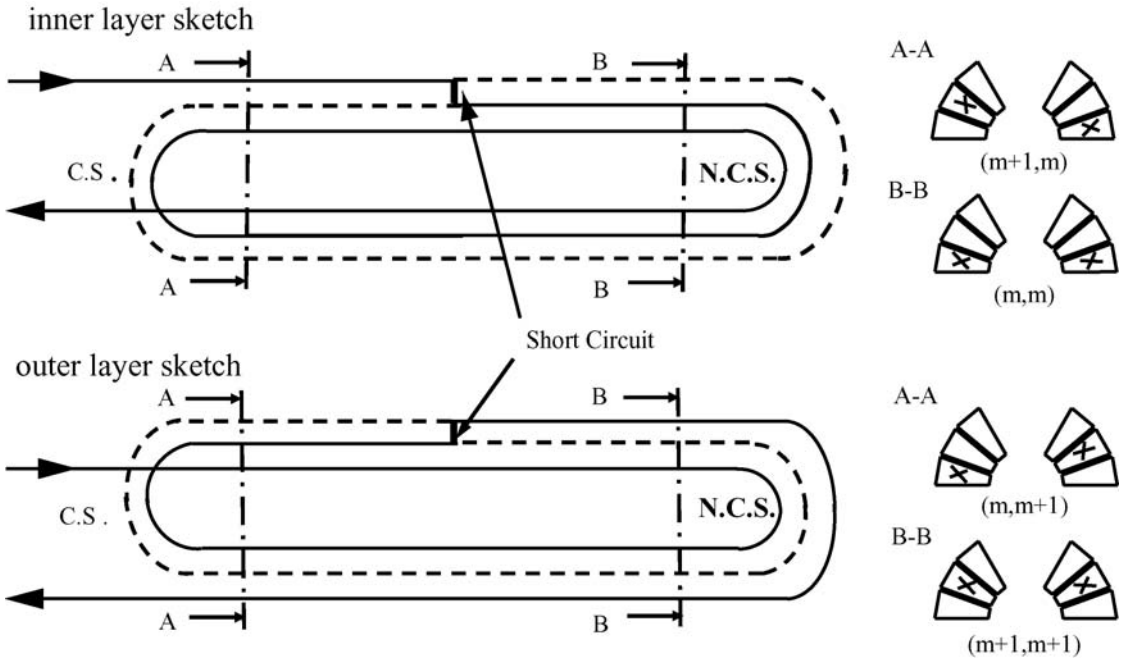

Figure 8.5: Short in the inner and outer layer, longitudinal view (left) and cross-section view (right).

Short in the inner layer give anomalies on several multipoles: therefore in general only one configuration can match these anomalies and the obtained solution is unique. On the other hand, outer layer shorts give rise to low impact on the high order multipoles, and therefore one can have different solutions matching the field measurement. It can happen that the short circuit is not “perfect”; this means that a certain amount of the total current still flows inside the cable. In this case, after an approximate localization, one can improve the simulations by having a non-zero current in the cables that are affected by the short. We will give examples in the next sections.

8.2 Application 1: perfect short on collared coil 2101

8.2.1 Detection of the case and field anomaly

The first measurement of this collared coil showed no anomalies. Then, during an insulation test, a drop of about 30 mΩ of the resistance of the coil was measured in aperture 2, corresponding to a short circuit of one turn. The magnetic field of aperture 2 was then measured again, and the measurement of aperture 2 without the short was used as a reference. The anomaly is uniform along the axis, thus suggesting that the short is in the coil end. In Table 8.1 we present the field harmonics averaged over the measuring positions of the straight part with and without the short circuit. We evaluate the field anomaly as the difference between these values, and we express them in units of the control limits set on the production (that are 3.5 times the measured standard deviation).

Table 8.1: Field harmonics averaged over the straight part of aperture 2 of the two measurements of collared coil 2101, difference, control limits on the production, and ratio between the difference and the control limits.

Harmonic	With Defect	Without Defect	Δ	Control Limits (3.5σ)	Δ/Control Limits
b2	0.15	-0.69	0.83	1.82	0.5
b3	5.87	-5.87	11.73	2.59	**4.5**
b4	0.47	0.02	0.45	0.46	1.0
b5	12.44	0.04	12.40	0.70	**17.7**
b6	-0.05	0.05	-0.10	0.21	-0.5
b7	2.22	0.79	1.42	0.22	**6.3**
b8	-0.04	-0.02	-0.02	0.08	-0.2
b9	-0.22	0.45	-0.66	0.05	**-12.6**
b10	0.00	-0.00	0.01	-	-
b11	0.51	0.71	-0.19	0.02	-8.9
a2	89.02	0.17	88.85	2.45	**36.3**
a3	-0.57	-0.48	-0.08	1.12	-0.1
a4	15.18	0.43	14.75	0.98	**15.1**
a5	-0.42	-0.17	-0.25	0.46	-0.5
a6	-3.15	-0.10	-3.05	0.25	**-12.4**
a7	-0.08	-0.04	-0.04	0.17	-0.2
a8	-1.70	0.07	-1.77	0.08	**-21.1**
a9	-0.00	-0.04	0.04	0.07	0.6
a10	-0.00	0.00	-0.00	-	-
a11	-0.02	-0.06	0.05	0.03	1.7

8.2.2 Short localization

Aperture and Pole: as already said the fault is in the aperture 2 and is confirmed by our method: average a_2 is about 35 times the control limits of the production. Since the a_2 is positive, the pole with the short is the *upper* one.

Measuring position and *layer identification*: in the last column of Table 8.2 the field anomaly is divided by the control limits set on the production. It is clear that the field anomaly is only on odd normal and even skew multipoles: therefore, the short is

in the connection side end. The linear fit of the function $f(n)$ defined in Eq. 8.7 gives a slope of 0.79 (see Figure 8.6). Using Eq. 8.9 we evaluate the distance of the short from the centre as R_s=37 mm, i.e. in the *inner layer* (whose distance from the centre is 28 to 43.9 mm).

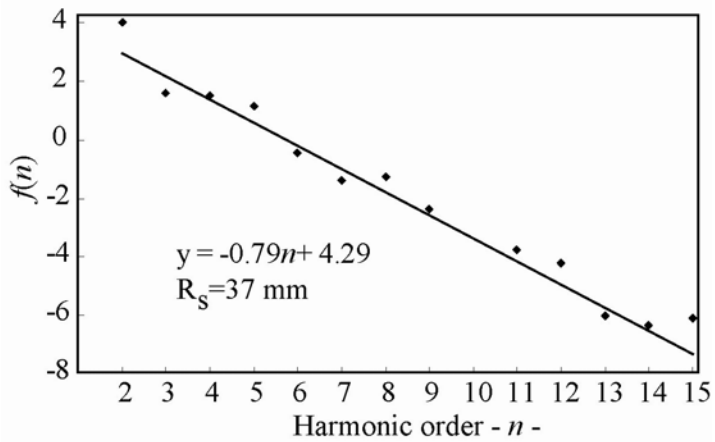

Figure 8.6: Function $f(n)$ as defined in Eq. 8.7 versus multipole order n for the field anomaly of collared coil 2101, and linear fit.

Cables identification: The short circuit configuration that minimizes the difference between the measurement and the model is the 34-34 (see Table 8.2): expected and measured values match within a fraction of unit. In Figure 8.7 and Figure 8.8 expected and measured effects on the even normal and odd skew multipoles are plotted. The short is placed somewhere within the first magnetic measuring position among the cable 34 and the cable 33, as shown in Figure 8.9.

Table 8.2: Field harmonics anomaly induced by a short: measured and expected.

Field Harmonics	Measured	Expected: 34-34	Meas.-Exp.
b3	11.74	11.89	-0.15
b5	12.40	12.12	0.29
b7	1.42	1.35	0.07
b9	-0.66	-0.69	0.03
b11	-0.19	-0.23	0.04
a2	88.85	88.69	0.15
a4	14.75	15.37	-0.62
a6	-3.05	-3.21	0.16
a8	-1.77	-1.72	-0.05
a10	-0.00	-0.06	0.06

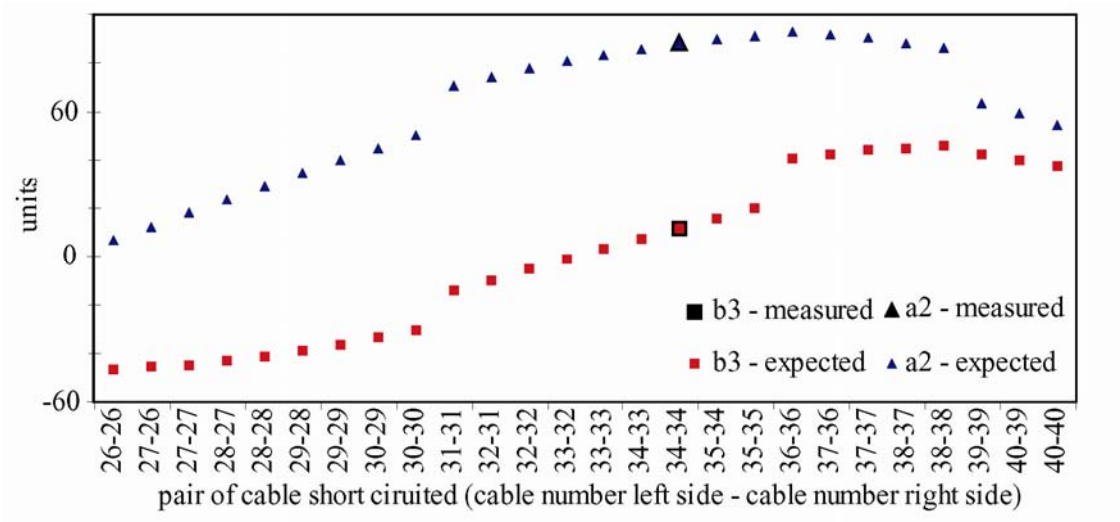

Figure 8.7: Expected and measured (case 2101) field anomalies in a_2, b_3 versus short position.

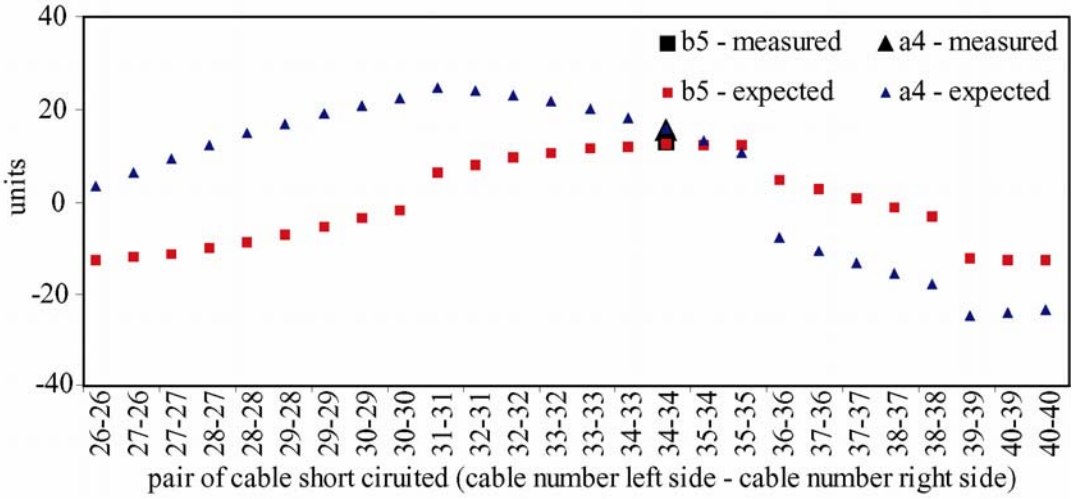

Figure 8.8: Expected and measured (case 2101) field anomalies in a_4, b_5 versus short position.

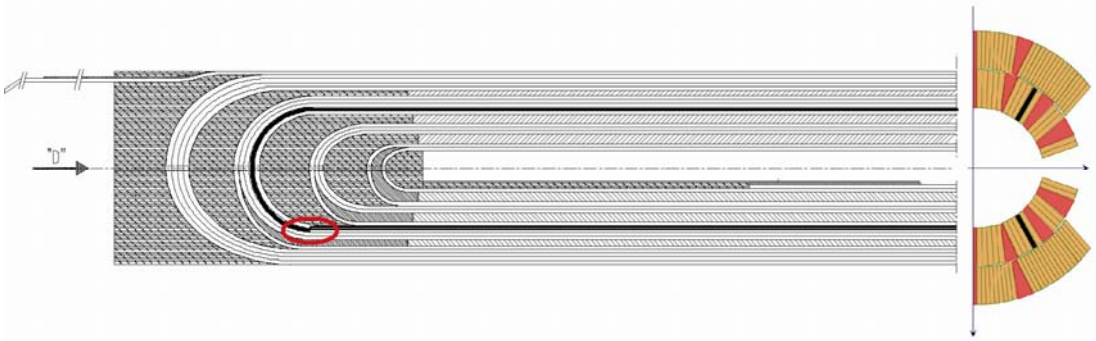

Figure 8.9: Location of the short circuit detected in the inner layer of cc 2101. The black line indicates the path that the current does not follow.

8.3 Application 2: partial short on collared coil 1154

8.3.1 Detection of the case and field anomaly

A short circuit has been detected in aperture 1 under the press during the collaring at 450 bars. A standard magnetic measurement has been performed on both apertures. In this case the other aperture has been taken as a reference. In both measurements we have very large values of b_2, due to the magnetic perturbation induced by the iron of the press, that disappears in the difference, see Table 8.3.

Table 8.3 Field harmonics averaged over the straight part of aperture 1 and 2 of collared coil 1154, difference, control limits on the production, and ratio between the difference and the control limits.

Harmonics	Defect Ap. 1	Reference Ap. 2	Δ	Control Limits (3.5σ)	Δ/control limits
b2	32.21	31.38	0.83	1.82	0.5
b3	26.13	-9.11	35.24	2.59	**13.6**
b4	0.92	1.28	-0.36	0.46	-0.8
b5	-1.47	0.28	-1.75	0.70	**-2.5**
b6	-0.06	-0.09	0.03	0.21	0.1
b7	-1.10	0.98	-2.08	0.22	**-9.3**
b8	0.10	0.03	0.07	0.08	0.9
b9	1.13	0.46	0.66	0.05	**12.6**
b10	0.00	0.00	0.00	-	-
b11	0.70	0.68	0.02	0.02	0.9
a2	64.97	0.18	64.78	2.45	**26.4**
a3	0.35	0.16	0.18	1.12	0.2
a4	-13.00	-0.06	-12.94	0.98	**-13.2**
a5	0.17	-0.02	0.19	0.46	0.4
a6	-1.65	0.03	-1.69	0.25	**-6.9**
a7	0.03	-0.08	0.11	0.17	0.7
a8	1.51	-0.01	1.52	0.08	**18.1**
a9	-0.09	-0.04	-0.05	0.07	-0.7
a10	0.00	0.00	0.00	-	-
a11	-0.07	-0.07	0.00	0.03	0.0

8.3.2 Short localization

Aperture and Pole: b_3 and a_2 more than ten times out of the production control limits. Since $\Delta a_2>0$, the faulty pole is the upper one.

Measuring position and *layer identification:* the even normal and odd skew multipoles show no anomaly and are within the production control limits; therefore it is on the connection side. The evaluation of the slope of the anomaly decay $f(n)$ gives Q=0.63 and R_c=31.9 mm, i.e. the inner layer.

Cables identification: 38-38 is the short circuit configuration that minimizes the difference between the measurement and the model. The match between expected and measured values is worse than the previous case (see Table 8.4): 20 units of a_2 and 10 of b_3 are not accounted. We can have a better agreement by assuming that the short is partial. The best agreement is obtained for 28% of current flowing in the conductor: here we recover an agreement within a fraction of unit. The short is placed in the first magnetic measuring position among the cables 38 - 37 (Figure 8.10 - Figure 8.12).

Table 8.4: Field harmonics anomaly induced by a short: measured (cc 1154) and expected for a complete and partial short.

Field Harmonics	Measured	I=0% inside short circuited cable		I=28% inside short circuited cable	
		Expected 38-38	Meas-Exp.	Expected 38-38	Meas-Exp.
b3	35.24	46.24	-11.01	34.68	0.56
b5	-1.75	-2.97	1.22	-2.23	0.47
b7	-2.08	-2.57	0.49	-1.93	-0.15
b9	0.66	0.85	-0.18	0.63	0.03
b11	0.02	0.01	0.01	0.01	0.01
a2	64.78	86.64	-21.86	64.98	-0.20
a4	-12.94	-17.32	4.38	-12.99	0.05
a6	-1.69	-2.01	0.32	-1.51	-0.18
a8	1.52	1.75	-0.23	1.31	0.21
a10	0.00	-0.26	0.27	-0.20	0.20

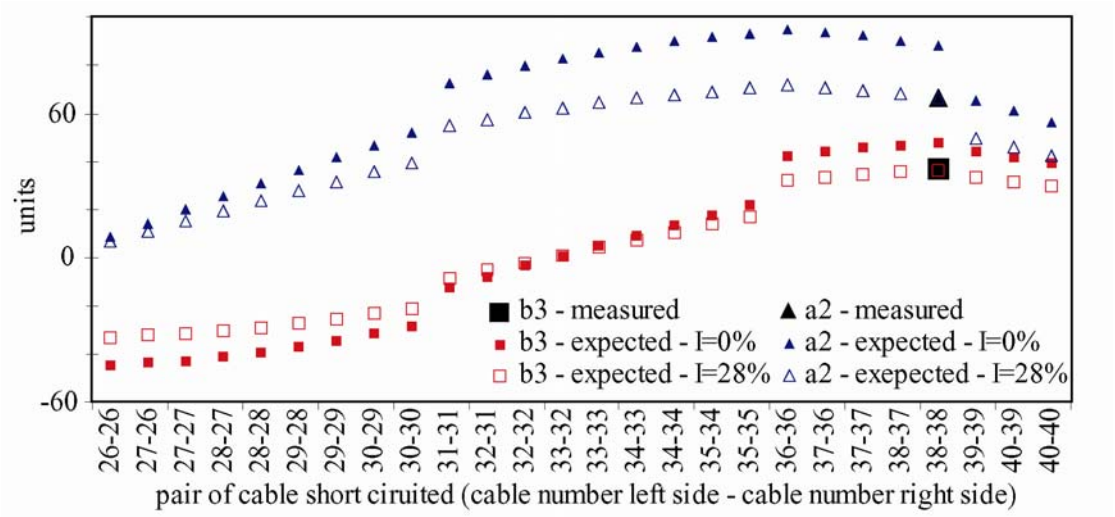

Figure 8.10: Expected and measured (case 1154) field anomalies in a_2, b_3 versus short position.

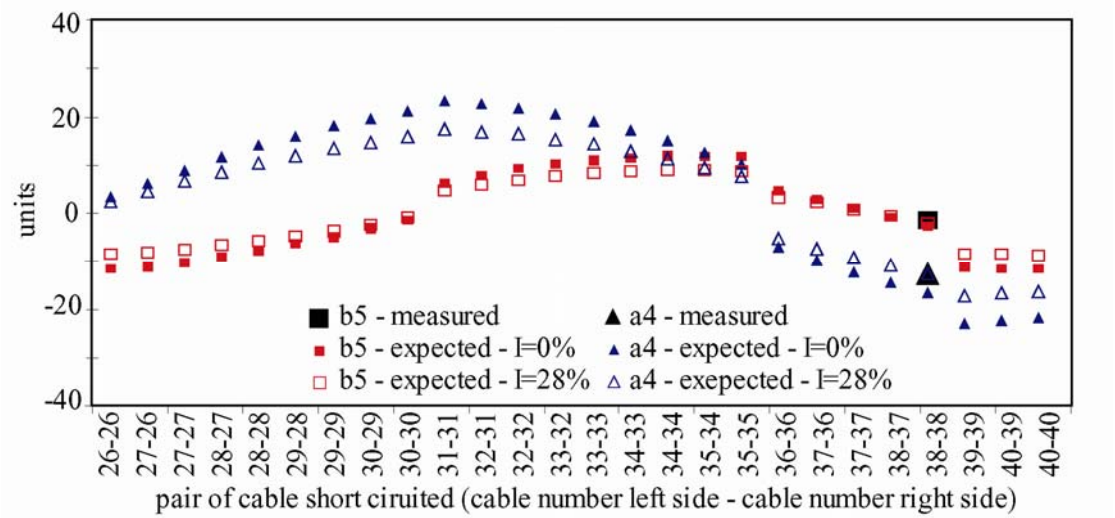

Figure 8.11: Expected and measured (case 2101) field anomalies in a_2, b_3 versus short position.

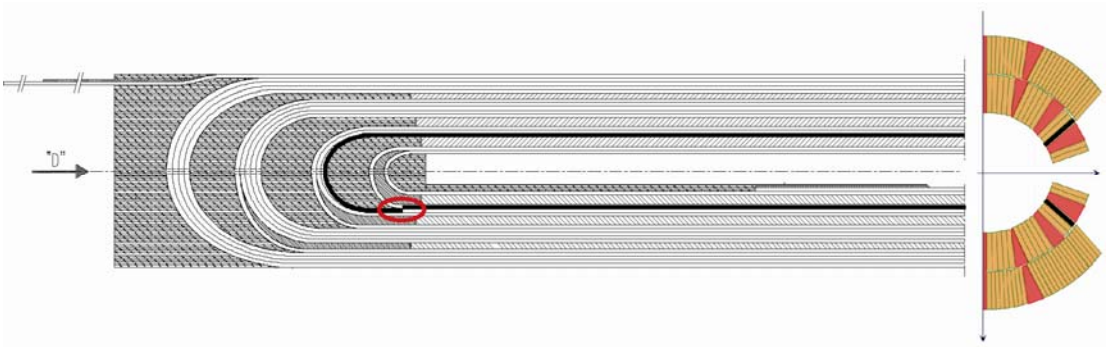

Figure 8.12: Location of the short circuit detected in the inner layer of cc 1154. The black line indicates the path that the current does not follow.

8.4 Application 3: limit of the method, short on c.c. 2230

8.4.1 Detection of the case and field anomaly

The short was detected on aperture 1 under the collaring press and it persisted after removal from the press. The collared coil was measured on the normal test bench and then the aperture 2 was taken as the reference. With respect to the other two cases analyzed the value of the b_3 of the faulty aperture is one order of magnitude less.

Table 8.5: Field harmonics averaged over the straight part of aperture 1 and 2 of collared coil 2230, difference, control limits on the production, and ratio between the difference and the control limits.

Harmonics	Defect Ap. 1	Reference Ap. 2	Δ	Control Limits (3.5σ)	Δ/control limits
b2	1.276	0.072	1.348	1.82	0.74
b3	1.722	-3.381	5.103	2.59	1.97
b4	0.274	0.079	0.354	0.46	0.77
b5	1.032	-0.612	1.643	0.70	2.35
b6	-0.047	0.006	-0.041	0.21	-0.20
b7	0.945	0.919	0.026	0.22	0.12
b8	-0.013	-0.012	-0.025	0.08	-0.31
b9	0.405	0.426	-0.021	0.05	-0.42
b10	-0.003	0.003	0.000	-	-
b11	0.734	0.736	-0.001	0.02	-0.05
a2	41.005	-1.258	42.263	2.45	17.25
a3	-0.610	-0.209	-0.401	1.12	-0.36
a4	2.676	-0.175	2.851	0.98	2.91
a5	-0.282	-0.108	-0.174	0.46	-0.38
a6	-0.361	-0.058	-0.303	0.25	-1.21
a7	-0.038	0.023	-0.061	0.17	-0.36
a8	-0.060	0.032	-0.093	0.08	-1.16
a9	-0.007	0.010	-0.017	0.07	-0.24
a10	0.001	0.002	-0.001	-	-
a11	-0.050	0.005	-0.055	0.03	-1.83

8.4.2 Short localization

Aperture and Pole: a_2 more than ten times out of the production control limits. Since $\Delta a_2>0$, the faulty pole is the upper one.

Measuring position: the measurements of the positions of the faulty aperture are within 1σ along the aperture axis. This gives the information that the short is located in one of the ends.

Layer identification: the evaluation of the slope of the anomaly decay $f(n)$ gives Q=1.21 and R_c=56.9 mm, i.e. the outer layer.

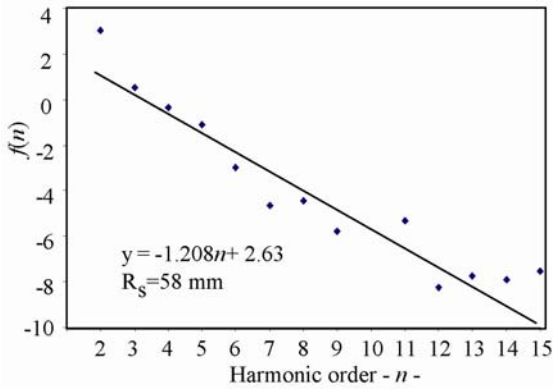

Figure 8.13: Layer localization of the short circuit occurred in collared coil 2230; function $f(n)$ versus multipole order n and linear fit.

Cables identification and measuring position: there are four possible configurations that match the measurements: 15-16, 16-17 (on the non-connection side end) and 16-16, 17-17 (on the connection side end), see Table 8.6.

In principle the four locations are reasonable, after the inspection performed on the given positions the short was localized non-connection side end between the cables 15-16, see Figure 8.14.

Table 8.6: Field harmonics anomaly induced by a short: measured (cc 2230) and expected for the four possible matches.

Field Harmonics	Measured	Expected: 15-16	Expected: 16-16	Expected: 16-17	Expected: 17-17
b2	1.348	1.400	0.000	1.431	0.000
b3	5.103	3.365	4.103	4.818	5.534
b4	0.354	0.231	0.000	0.194	0.000
b5	1.643	1.682	1.702	1.697	1.692
b6	-0.041	-0.027	0.000	-0.038	0.000
b7	0.026	0.108	0.086	0.062	0.038
b8	-0.025	-0.010	0.000	-0.009	0.000
b9	-0.021	-0.014	-0.017	-0.019	-0.021
a2	42.263	40.893	41.427	41.865	42.303
a3	-0.401	-0.177	0.000	-0.251	0.000
a4	2.851	3.394	3.139	2.855	2.570
a5	-0.174	-0.146	0.000	-0.147	0.000
a6	-0.303	-0.258	-0.313	-0.361	-0.408
a7	-0.061	-0.012	0.000	-0.006	0.000
a8	-0.093	-0.070	-0.069	-0.066	-0.062
a9	-0.017	0.003	0.000	0.003	0.000

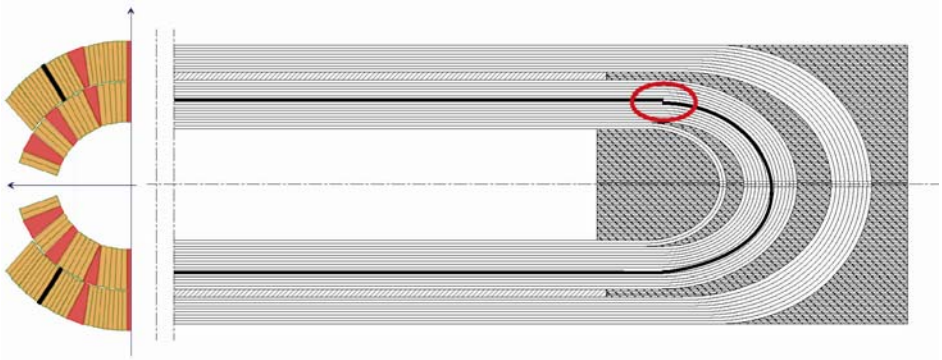

Figure 8.14: Location of the short circuit detected in the outer layer of cc 2230. The black line indicates the path that the current does not follow.

8.5 Overview of the detected cases of electric shorts

Using an electromagnetic code, the effect of shorts between adjacent cables on field quality can be forecast, and the analysis of experimental data gives a location of the short. The method is very sensitive, also allowing to detecting if the short is perfect or only partial. For short located in the inner layer of the coil the method has been revealed to be very reliable since the field anomalies generated by the defect are very large compared to the natural spread in field quality induced by tolerances and assembly procedures. On the other hand, when the short is in the outer layer, the effect on the field quality is not large enough to have a perfect localization and hence, the location is given with a certain indetermination.

Eighteen collared coils presenting electrical shorts have been analyzed and the affected coil have been rescued using this procedure. They belong to two cold mass manufacturers (11 of Firm1 and 7 of Firm2). The main features of all the detected shorts are given in Table 8.7: all have been localized in the magnet ends, and 11 out of 18 in the connection side, which is most critical one due to the asymmetry of the assembly. In most of the cases the short is in the inner layer. They are equally shared among upper and lower poles, and aperture 1 and 2 as expected. Different locations in the cross-section have been found; we had several cases of short in the cable 38-38, corresponding to the same manufacturing problem.

In the first two cases, due to the insufficient experience on the problem, it has not been possible to verify the presence of the short where foreseen by the method. These were difficult cases were the short appeared only during the collaring at a given pressure and disappeared after the disassembly of the collared coil. Dedicated procedures to have an experimental evidence of the short have been developed, and have been applied successfully to all the successive cases. In all cases the location of the short matched the result of the method presented here. For the four last collared coil analyzed, the defect was found in the outer layer, and, as mentioned above, a not precise localization could be done. For each case a set of probable location were worked out and only after the inspection of the collared coils the exact position could be determined.

Table 8.7: Main features of all the detected shorts

Firm	Dipole	Short – Circuit Localization				
		Aperture	Pole	Meas. Position	Layer	Short Configuration
01	1103	1	Upper	1	Inner	38-38
01	1124	2	Upper	1	Inner	38-38
01	1127	1	Lower	1	Inner	38-38
01	1141	1	Upper	1	Inner	38-38
01	1154	2	Upper	1	Inner	38-38
01	1165	1	Lower	1	Inner	38-38
01	1178	1	Lower	1	Inner	38-38
01	1217	1	Upper	20	Inner	38-37
01	1326	1	Lower	1	Inner	40-40
01	1332	2	Upper	1	Inner	30-30
01	1526	2	Upper	20	Inner	40-39
02	2087	2	Upper	1	Inner	34-34
02	2101	2	Upper	1	Inner	34-34
02	2202	2	Lower	1	Inner	38-38
02	2278	1	Upper	20	Outer	19-20
02	2321	2	Lower	1	Outer	3-3
02	2330	1	Upper	20	Outer	15-16
02	2342	1	Lower	20	Outer	24-25

References

[8.1] P. Komorowski, D. Tommasini,*"Localization of electrical insulation failures in superconducting collared coils by analysis of the distortion of a pulsed magnetic field"*, CERN **LHC-Project-Report-343** – 1999

[8.2] www.bnl.gov/magnets/Staff/Gupta/scmag-course/uspas03/AJ03/AJ_ProductionTool.pdf - A. Jain.

[8.3] Private communication, G. Molinari CERN/AT/MAS

[8.4] E. Wildner; S. Pauletta, V. Remondino, W. Scandale, E. Todesco, C. Völlinger *"Production Follow-Up of the LHC Main Dipoles through Magnetic Measurements at Room Temperature"*, CERN **LHC-Project-Report-703** – 2004 .

[8.5] J. Billan et al., *"Magnetic measurements of the LHC quadrupole and dipole magnets at room temperature",* CERN **LHC–Project Note 283** - 2002

[8.6] S. Pauletta et al., "*Field quality analysis to monitor the industrial series production of the dipole magnets for the Large Hadron Collider"*, CERN-Thesis-2003-002

[8.7] B. Bellesia et al, "*Room Temperature magnetic Field Measurements as a Tool to localize Inter-Turn electrical short circuits in the LHC Main Dipoles"*, IEEE Trans. Appl. Supercond. **Vol. 16** (**2005**) 208-11, also as CERN **LHC Project Report 871**.

Chapter 9

Conclusion

In this work a detailed analysis of the influence of the mechanical components and the assembly procedures of the LHC main dipole on the field shape at room and cryogenic temperatures has been done.

The analysis of the productions of cables, copper wedges and austenitic steel collars showed that the dimensions are inside the tolerance limits with some exceptions for the early productions of the wedges and for few dimensions of the collars. Moreover, the productions of the six suppliers of cables and of the two of collars are very homogeneous. Some differences (~15%) have been found only in the magnetization of the two suppliers of the inner layer cable of about 15%.

Coupling magneto-static models and the geometrical measurements of the mechanical components the influence of the dimensions on the field quality of the dipoles has been investigated; in particular, the main results are:

Superconducting cables:

- The simulations show that the cable dimension variations could account for most of the specified random components of a_2 and a_4 and it is negligible for the other multipoles.
- For high order allowed harmonics (b_5 and b_7) measured at 1.9 K there is a difference between magnets that can be traced back to the difference in magnetization between inner cable manufacturers.

Copper wedges:

- A relevant systematic effect on the b_3 (1.5 units) of the first produced wedges is visible in the collared coil magnetic measurements at room temperature. This explains part of the upward trend observed in b_3 in the first 25 collared coils.
- It has been shown that the advices given at the beginning of the wedge production brought to a more careful control on the manufacturing and as a result the total influence of the copper wedge dimensions on the collared coil magnetic field is not relevant

Austenitic steel collars:

- The collar shape is the driving mechanism of field harmonics only for the even normal and odd skew in particular for b_2 and a_3 in Firm3, where collars of the supplier S_2 are used. Two independent observations support this fact: firstly, we have strong correlations between apertures of the same magnet as expected from the assembly procedure. Secondly, the

expected values based on the measured dimension of the collars agree with magnetic measurements both for the average and for the standard deviation.

A more general study on the random components of the field harmonics has been worked out in order to evaluate the uncertainty in the coil position in the transverse cross-section generated by mechanical tolerances. This is one of the main sources of random components of the field harmonics, limiting the possibility of obtaining a perfect field quality. We reviewed the data of the production of dipoles relative to four accelerators to analyze the agreement of the Monte-Carlo estimates with the measured values. The above quoted Monte-Carlo method, widely used in the past, gives similar estimates for normal and skew harmonics of the same order. However, already in the Tevatron production it has been observed that random components of normal and skew harmonics of the same order can differ of a factor 4 to 6. We proposed to associate different amplitudes to generate normal and skew harmonics, in order to better fit the experimental data. The final result of the analysis is an improved phenomenological model based on the acquired experience of the four large scale dipole productions to describe and forecast the random errors in a superconducting dipole. With these studies we found that there is an improvement of the degree of precision in positioning the cable block: for the first dipole production, Tevatron, the order of magnitude of geometric random components is compatible with a random movement of the blocks of ~ 65 μm whilst for the more recent productions (LHC and RHIC) e the lowest values is recorded (52 - 54 μm). In order to better estimate the field errors the four classes of harmonics are separately considered and four displacements are calculated. For RHIC and LHC dipole productions random movements of the blocks of ~50 μm r.m.s. are needed for the odd normal multipoles, ~30 μm for the even skew, and 5 to 20 μm for the even normal and for the odd skew. Such parameters allow estimating the random geometric errors with an average error of ~20%.

In the last chapter a method based on magnetic measurements at room temperature to locate electrical shorts in the coil of the main LHC dipole has been presented. The approach is reliable since the field anomalies generated by the short are, in general, very large compared to the natural spread in field quality induced by tolerances and assembly procedures. We have shown that using an electromagnetic code, one can forecast the effect of shorts between adjacent cables on field quality, and that the comparison to experimental data gives a location of the short. The method is very sensitive, also allowing to detecting if the short is perfect or only partial. Along the LHC main dipole production, 18 coils presenting electrical shorts have been analyzed and rescued using this procedure.